

R-07-51

**Modelling the long-time stability
of the engineered barriers of SFR
with respect to climate changes**

Peter Cronstrand, Vattenfall Power Consultant

February 2007

Svensk Kärnbränslehantering AB

Swedish Nuclear Fuel
and Waste Management Co
Box 5864

SE-102 40 Stockholm Sweden

Tel 08-459 84 00

+46 8 459 84 00

Fax 08-661 57 19

+46 8 661 57 19



ISSN 1402-3091

SKB Rapport R-07-51

Modelling the long-time stability of the engineered barriers of SFR with respect to climate changes

Peter Cronstrand, Vattenfall Power Consultant

February 2007

Keywords: dokID 1082620, Degradation, EBS, Concrete, Bentonite, SFR 1 SAR-08.

This report concerns a study which was conducted for SKB. The conclusions and viewpoints presented in the report are those of the author and do not necessarily coincide with those of the client.

A pdf version of this document can be downloaded from www.skb.se.

Preface

This document describes the degradation of the engineered barriers in SFR 1 in a long-term perspective. This document constitutes one of the references describing chemical degradation of concrete and bentonite used in the safety analysis SFR 1 SAR-08.

Peter Cronstrand, Vattenfall Power Consultant AB has compiled the report.

This document has been reviewed and all comments have been documented in accordance with SKIFS 2004:1.

Stockholm, November 2007

Anna Gordon

Project leader, SFR 1 SAR-08.

Summary

Extensive modelling has been performed on various degradation processes that are related to climate changes and are believed to critically affect the long-term safety of the Silo and BMA at SFR. The model employs a variation of temperature and composition of infiltrating water, a dynamic update of the transport conditions parameterized through the porosity, fracture mechanics and addresses the expected freeze-thaw effects through a successive increase of the diffusivity. In order to evaluate the sensitivity of the model each effect is evaluated as a deviation from a base case before being incorporated in a complete model. Irrespective of the inclusion or exclusion of temperature and/or salinity variation and a dynamically updated diffusivity the calculations are in mutual agreement concerning the depth of the degradation, which for the Silo and BMA reaches half way through the concrete wall at year 100,000.

A more substantial acceleration of the aging processes can be achieved by the inclusion of fractures or freeze-thaw effects, for which the results beyond year 50,000 are highly uncertain, but indicates that further degradation will be rapid. Although the present fracture model is incomplete, it demonstrates that rapid changes in transport conditions associated with emerging fractures can pose a serious threat to the repository.

Contents

1	Introduction	9
1.1	Purpose	9
1.2	Background	9
1.3	The impact of climate changes	9
1.4	Conceptual model of concrete degradation	10
2	Method of approach	11
2.1	Thermodynamic modelling	11
2.2	Fracture and damage mechanics	11
2.2.1	Introduction to fracture mechanics in concrete	11
2.2.2	Expansion mechanisms	12
2.2.3	Linear region	13
2.2.4	Pre-peak region	13
2.2.5	Post peak region	13
2.3	Freeze-thaw effects	14
2.4	Failure criterion	15
2.5	Transport conditions	15
2.5.1	General remarks	15
2.5.2	Porosity	16
2.5.3	Diffusivity	16
2.6	Simulations	18
2.7	Software	18
3	Input data	19
3.1	Models of BMA and the Silo	19
3.2	Thermodynamic database	19
3.3	Water and temperature variation	20
3.4	Concrete/cement	21
3.4.1	Chemical composition	21
3.5	Mechanical/Fracture parameters	23
3.6	Transport parameters	23
4	Results	25
4.1	Silo	25
4.1.1	A. Base case scenario	25
4.1.2	B. Varying temperature	25
4.1.3	C. Varying salinity	25
4.1.4	D. Dynamic diffusivity	26
4.1.5	E. Dynamic model	26
4.1.6	F. Fracture model	27
4.1.7	G. Freeze and thaw effects	27
4.1.8	Comparison between scenarios regarding porosity and pH	27
4.2	BMA	28
4.2.1	General remarks	28
4.2.2	A. Base case scenario	28
4.2.3	B. Varying temperature	29
4.2.4	C. Variable salinity	29
4.2.5	D. Dynamic diffusivity	29
4.2.6	E. Dynamic model	29
4.2.7	F. Fracture model	29
4.2.8	G. Freeze and thaw effects	30
4.2.9	Comparison between scenarios regarding porosity and pH	30

5	Comments and conclusions	31
5.1	General remarks	31
5.2	Silo	31
5.3	BMA	32
5.4	Uncertainties	32
5.4.1	Uncertainties of various input data	32
5.4.2	Uncertainty due to the thermodynamic database	33
5.4.3	Uncertainty due to the transport model	33
5.4.4	Overall uncertainty	35
6	References	37
	Appendix A	41
	Appendix B	43

1 Introduction

1.1 Purpose

The purpose of this report is to assess the overall degradation of the engineered barriers constituting SFR in a long-term perspective, with special emphasis on the effects arising from climate changes, in particular permafrost. The model employs variation of temperature and composition of infiltrating water, a dynamic update of the transport conditions parameterized through the porosity, fracture mechanics and addresses the expected freeze-thaw effects through a successive increase of the diffusivity. In order to evaluate the sensitivity of the model each effect is evaluated as a deviation from a base case before it is incorporated in a complete model.

1.2 Background

The evolution of the structural integrity of the engineered barriers of a nuclear repository greatly influences the expected retention of radionuclides, both by ensuring low diffusivity, but also by maintaining a high pH, which promotes the sorption of various radionuclides. Any thorough long-term scenario for SFR therefore must include future climate changes, with permafrost and glaciations cycles as the dominating events with major implications for the barriers. The effects are either direct, as a reduction in the rates of chemical reactions, scaling the diffusivity through the viscosity, but foremost physical through various freeze-thaw effects, or indirect through the impact on the composition of the infiltrating water. The overall degrading process can be described as successive trials of the material to equilibrate with infiltrating water. The leaching of mainly Ca and OH in combination with the intrusion of chlorides, sulphates and carbonates will force the materials to re-equilibrate through various dissolution and precipitation processes. Since the mineral phases will occupy different volumes and exhibit different re-crystallization patterns, the initial transport conditions given by the initial pore structure will evolve with time. Moreover, as the repository largely is based on cementitious materials in combination with bentonite clay, a non-trivial effect is introduced through the interaction between the barriers.

Although the general features of each influence can be derived from conceptual estimates, the combination of these effects, as well as the requirement for quantification of various parameters related to the physical state of the repository, calls for numerical modelling. Thus, a modelling approach need not only to address the ultimate combination of the above-mentioned effects, but also evaluate the contribution from each effect in order to assess the sensitivity of the model to given input data.

1.3 The impact of climate changes

Except for the merely physical effect of freezing, all major effects of climate changes on a nuclear repository can be derived from hydrochemistry changes. Permafrost, glaciations and shoreline movements will all affect the composition of the water infiltrating the repository, which in turn will affect the rate and character of the degrading process. Permafrost could also increase the salinity through salt exclusion, i.e the freezing of available water will create a moving front of high saline water as the freezing front advances through the repository. However, due to the low salinity of water prevailing at periods when permafrost reaches depths critical for the repository, this effect is considered insignificant (see for instance /Vidstrand et al. 2006/).

Temperature effects will also have a direct, but presumably small, influence through regulating the viscosity and the rates of various detrimental chemical reactions.

Nevertheless, all chemical effects are probably subordinate to the direct physical impact of the freeze-thaw cycles. Since the cement is expected to be completely saturated in each freezing cycle, the freezing process can be assumed to cause maximum damage in each cycle /Emborg et al. 2007/.

1.4 Conceptual model of concrete degradation

Although the hydration of cement does not occur instantaneously, the time is short compared to its life and the final material is not in equilibrium, which may be subjected to further reorganisation and re-crystallisation. The main constituents of cement are the crystalline portlandite and the amorphous to crypto-crystalline calcium-silica-hydrate (CSH-gel). Concrete will also contain in addition to cement a substantial amount of ballast, such as sand, gravel or crushed rock. All cementitious materials will also include excess minerals such as ettringite, hydrotalcite and Friedel salt /Brown and Lacroix 1989, Damidot et al. 1992, 1994, Damidot and Glasser 1993, 1995, Lagerblad and Trägårdh 1994, Clodic and Meike 1997/. Although these minerals control the setting of the cement and also affect the long-term porosity changes, they are not considered to contribute to the binding capacity of the cement.

Cement contains both capillary pores and gel pores, of which capillary pores constitute the major path for the ion migration. Diffusion through the gel pores is possible, but at least 400 times slower /Bentz et al. 1995/. From theoretical considerations it has been estimated that cement pastes with w/c below 0.4 would not contain any capillary pores. In reality inhomogeneities and unhydrated clinker grains will contribute pore structure and enable ion transport.

Because the dissolution of CSH-gel is accompanied by structural as well as chemical changes in Ca/Si-ratio, the dissolution mechanism is non-trivial and several concurrent models have been proposed /Jennings 1986, 2000, Gartner and Jennings 1987, Richardsson 1999, Famy et al. 2003, Chen et al. 2004/. One method, /Berner 1988, Revertegat et al. 1997/ represents the incongruent dissolution, the structural decrease and successive decrease in Ca/Si ratio by a discrete set of mineral phases with their own independent solubility products, often denoted $CSH_{1.8}$, $CSH_{1.1}$ and $CSH_{0.8}$. The upper limiting composition of the solid solution series is $CSH_{1.8}$ and above a Ca/Si-ratio of 1.8 portlandite precipitates as a separate phase

A refinement of the variable log K approach is to describe the CSH gel as a two end member solid solution. Although more intuitively appealing and based on a more elaborate thermodynamic theory, the model shares the weaknesses of the variable log K approach, the dependence of carefully selected empirical parameters. Whilst the variable log K approach requires only log K values, the solid solution approach also require Guggenheim parameters in order to scale the Gibbs free energy between the end members in the Guggenheim thermodynamic mixing model. Clearly the same degree of conservatism required in a performance assessment can be achieved within both paradigms. With Guggenheim parameters suggested by /Kersten 1996/ preliminary results was found to be less conservative than results obtained with the variable log K approach and /ZZ-Hatches 2006/ database. Thus, it is expected that the results and the derived conclusions would not be significantly affected by a more rigorous technique, but merely show almost identical dissolution mechanisms only slightly shifted in time.

The degradation of concrete or cement is characterized by leaching, often in combination with intruding ions, which perturb pre-existing mineral equilibria. Since the stability is determined by thermodynamic equilibria, the degradation scheme is accompanied with distinct decreases in pH, which may serve as a fingerprint on the prevailing mineral distribution (see Table 1-1). While, alkali hydroxides initially maintain the pH at 13.5, leaching processes lowers the pH to 12.5 where mainly portlandite controls the pH. The subsequent dissolution phase is mainly characterized by the incongruent dissolution of calcium-silica-hydrate (CSH). A Ca/Si-ratio below 1 and a pH below 10.5 coincide with the collapse of ettringite.

Table 1-1. Controlling mineral phases at given pH.

pH	Controlling phase
13.5	Alkali hydroxides
12.5	Portlandite
12.5–10.5	CSH

2 Method of approach

2.1 Thermodynamic modelling

The computational approach is based on ion transport through diffusion in conjunction with thermodynamic equilibrium calculations and employs the local equilibrium assumption (LEA), i.e. chemical reaction will be much faster than the transport. The main implication from the LEA assumption is that the transport steps can be decoupled from the equilibrium calculations.

The main purpose behind thermodynamical modelling is to minimize the global change in, Gibbs Free energy, which in case of the present model comprises contributions from solid phase and aqueous species, i.e.

$$\Delta G_{solid} = \sum_i n_i \Delta G_{f,i}^0 \quad (2-1)$$

and

$$\Delta G_{aqueous} = \sum_i n_i \Delta G_{f,i}^0 + RT \sum_i \ln m_i + RT \sum_i \ln \gamma_i \quad (2-2)$$

Whereas the activity coefficient, γ , for the solid phases in general is assumed to be 1, there are numerous equations proposed for aqueous species. The standard relation in PHREEQC is the Davies equation, which in accordance with the majority of proposals includes the ionic strength (μ), the valence of the ion (z) and a temperature dependent constant, A .

$$\log \gamma_i = -Az_i^2 \left(\frac{\sqrt{\mu}}{1 + \sqrt{\mu}} - 0.3\mu \right) \quad (2-3)$$

Other relationships, especially designed for the environment in cement have been developed, but are currently not implemented in PHREEQC /Samson et al. 1999, 2001/.

The dissolution of the ballast, in the model represented by quartz, albite, k-feldspar and biotite, is modelled through a simplified kinetic relation

$$\frac{dm}{dt} = c \left(\frac{m}{m_0} \right)^{2/3} \quad (2-4)$$

with the rate constant, c , chosen to $10^{-13.7}$ in accordance with rate constant suggested for quartz /Rimstidt and Barnes 1980/. The modelling of the dissolution kinetics is clearly incomplete by neglecting pH, and distance to equilibrium, but still reflects the assumed slow interaction with additional cement constituents. Moreover, a more elaborate kinetic description could potentially introduce numerical instabilities because of the stepwise degradation of CSH, which would impose further requirements on step length etc.

2.2 Fracture and damage mechanics

2.2.1 Introduction to fracture mechanics in concrete

Although the causes of the deformation mainly are of chemical origin (e.g. formation of ettringite), the model for fracture and damage mechanics is based on mechanical strain-stress/crack opening model from /CEB-FIP model code 1993/. Freeze and thaw effects are not included, but are addressed through a successive increase of the diffusivity for each permafrost cycle (see Section 2.3).

The exact mechanism of deformation is not entirely understood, but experimental observations indicate that the stress-deformation steps can be divided in several stages. The two critical events during the strain-stress evolution are the transition from linear elastic response to non-linear response and the crossing of the peak of maximum stress corresponding to the material property ultimate stress, f_t . The typical stress-strain curve will therefore be composed of three sections with different curvature and underlying mechanisms.

1. A linear elastic response characterized by a constant deformation modulus, E_0 .
2. A pre-peak region where micro-cracks are initiated and then propagated through the specimen causing strain localization. The modulus is assumed to decrease according to a linear or non-linear relation.
3. A post-peak region characterized by a stress-decrease and crack-width opening which leads to a failure of the specimen.

Throughout the stress-strain-curve, the actual damage is parameterized by the damage parameter, ω , which here is considered as a scalar between 0 and 1, where 0 corresponds to an undamaged and 1 to a failed specimen. Although the damage parameter can be motivated from a micro-mechanical approach and related to a crack density /Li and Shah 1994/, it is here primarily considered as a phenomenological parameter and mainly employed to evaluate the final diffusivity, d as

$$d = d_c + \omega(d_0 - d_c) \quad (2-5)$$

where d_c denotes the capillary diffusivity and d_0 the diffusivity in free water. For an undamaged specimen ($\omega = 0$) $d = d_c$, whereas for a completely damaged specimen ($\omega = 1$) $d = d_0$.

Unlike some damage mechanics models, the damage parameter is not considered as the driving force of the evolution, but mainly serves as measure of the observed degradation. Key parameters are the tensile strength, f_t , and the fracture energy, G_F . The stress-strain evolution is based on /CEB-FIP model code 1993/.

2.2.2 Expansion mechanisms

The primary cause behind the cracking is assumed to be an internal pressure evaluated as a simple volumetric strain through

$$\varepsilon_v = \sum_p \left(\frac{\Delta V}{V} \right)_p \quad (2-6)$$

Because precipitation can occur either in existing capillary pores or in the emerging micro-cracks, it necessary to establish a relation between the porosity and the fraction of the precipitating minerals that causes volume expansion and increased strain. One approach suggested by /Tixier 2000/ is to postulate a cut-off value by subtracting a fraction of the initial porosity as

$$\tilde{\varepsilon}_v = \varepsilon_v - f\varphi \quad (2-7)$$

where f here is the fraction of the minerals that populates the pores. Clearly, when the porosity is 0, f loses its relevance and if f is set to 1, the threshold coincides with zero porosity. In practice, the relation above defines a threshold and a suggested value for f which applies for most types of concrete based ordinary portland cement is 0.3 according to /Tixier 2000/.

The final and effective strain is obtained by assuming isotropy as

$$\varepsilon = \frac{\varepsilon_v}{3} \quad (2-8)$$

2.2.3 Linear region

The linear elastic region is characterized by a constant deformation modulus, E_0 , and an undamaged specimen ($\omega = 0$).

$$E = E_0 \quad (2-9)$$

The region is terminated when the strain reaches the threshold strain, ε_{th} . To account for the effects of hydrate dissolution in this region, the following formula, suggested by /Kamali et al. 2003/ relates the increase of capillary porosity to the decrease in deformation modulus

$$\frac{E}{E_0} = \left(\frac{1 - \varphi}{1 - \varphi_0} \right)^{3.16} \quad (2-10)$$

2.2.4 Pre-peak region

In the pre-peak region, $0.9f_t < \sigma \leq f_t$, the stress is evaluated as

$$\sigma = f_t - \frac{0.1f_t}{\varepsilon_p - 0.9f_t/E_0} (\varepsilon_p - \varepsilon) \quad (2-11)$$

The damage parameter is assumed to follow the micromechanical scalar damage model for tensile response of concrete suggested by /Karihaloo and Fu 1989/

$$\omega = \omega_0 - C_1 \left(1 - \frac{\varepsilon_{th}}{\varepsilon}\right)^{C_2} \quad (2-12)$$

where

$$\varepsilon_{th} = \frac{0.9f_t}{E_0} \quad (2-13)$$

The constants, C_1 and C_2 , are 0.16 and 2.3 for randomly distributed penny-shaped cracks, 0.24, and 2.60 for spherical micro-voids. Other relations are plausible; the essential feature is a gradual increase, but fairly slow since no opening of the cracks is occurring, the emerging cracks remain closed. The region is terminated when the stress reaches the ultimate strength, f_t .

2.2.5 Post peak region

The post-peak region is characterized by crack-opening and several models have been suggested to capture the process, linear relation, exponential decay, power laws, all with the aim of describing a decay from f_t to a minimum stress, usually zero. CEB-FIP suggests a two-step model, where the initial rapid decrease in stress from f_t to $0.15f_t$ from zero to crack width w_l . The subsequent opening to zero stress and the ultimate width w_c is slower. In terms of equations this scenario corresponds to a bilinear stress-crack opening relation as

$$\sigma = f_t \left(1 - 0.85 \frac{w}{w_l}\right) \text{ for } 0.15f_t \leq \sigma \leq f_t \quad (2-14)$$

and

$$\sigma = \frac{0.15f_t}{w_c - w_l} (w_c - w) \text{ for } 0 \leq \sigma < 0.15f_t \quad (2-15)$$

where the critical widths w_l and w_c are defined as

$$w_l = 2 \frac{G_F}{f_t} - 0.15w_c \quad (2-16)$$

where

$$w_c = \alpha_F \frac{G_F}{f_t} \quad (2-17)$$

and α_F is determined from the maximum aggregate size, d_{max} , according to Table 2-1.

Table 2-1. Maximum aggregate size, d_{max} , related to the coefficient α_F to estimate w_c .

d_{max} (mm)	8	16	32
α_F	8	7	5

The damage parameter is chosen to inversely mimic the stress decrease, i.e.

$$\omega = \omega_p + \frac{0.85w}{w_l} \quad (2-18)$$

during phase I and

$$\omega = \frac{0.15}{w_c - w_l}(w - w_l) + 0.85 - \omega_p \quad (2-19)$$

during phase II. The most pronounced growth of the damage parameter and the diffusivity clearly occurs during crack-opening phase.

2.3 Freeze-thaw effects

There are several concurrent theories about the physical-chemical mechanisms causing fractures in concrete when freezing (hydraulic pressure, osmotic pressure, crystallization pressure). Although most theories strongly reject the trivial explanations as the volume expansion of 9%, the effects can be scaled to this expansion. Since the major objective of the repository is not to support load in a mechanical sense, but the ability to contain and reduce the discharge of radionuclides, it is sufficient to parameterize the freezing damage in terms of stepwise increases in the diffusivities in order to capture the acceleration of the aging kinetics (see Table 2-2). The values of the diffusivities are correlated to the temperature variation described by Figure 3-1, but this should merely be considered as tentative approach to address a gradual change of the integrity. A perhaps more reasonable – but not particularly illuminating approach from a modelling point of view – would clearly be to assume a complete rupture at first freezing cycle which immediately destroys the sorption barrier.

In a conservative freeze-thaw scenario the first major freezing cycle occurring at year 50,000 (see Table 3-1) is assumed to destroy the pore-structure of the concrete. Thus, the succeeding freezing cycles are therefore within the same scenario considered to act upon a strongly degraded material and even moderate temperatures below 0°C are addressed as critical for the cement-based barriers.

Table 2-2. Diffusivities of the concrete as scaled by the successive freezing periods.

Period (year)	Diffusivity (m ² /s)
< 45,000	1.0E-11
45,000–49,000	5.0E-11
49,000–57,000	1.0E-10
57,000–80,000	5.0E-10
80,000–100,000	1.0E-9

2.4 Failure criterion

It is essential to distinguish between mechanical and thermodynamic failure. Mechanical failure occurs when the damage parameter, ω , reaches 1, and the crack-width is stretched to w_c (in general some tenths of a millimetre). The material is considered to permanently have lost its ability to support any load. However, the material may still be intact from a thermodynamic point of view, in the sense that all cement-specific constituents, i.e. CH and CSH, still appear unaffected by the ongoing ion intrusion. However, because of the substantially increased diffusivity, the degrading mechanisms clearly will be accelerated. In contrast to the well-defined mechanical failure criterion, there are no unique and simple thresholds for thermodynamical failure. In general the material is assumed to retain the binding capacity at least as long as portlandite controls the pH. Even though the mechanical strength is strongly reduced because of the depletion of portlandite, the silica structure can undergo a substantial loss of Ca and it is believed that the material will maintain structural integrity, although weakened, while the CSH-gel is not entirely degraded, i.e. a Ca/Si ratio above 1. Because the distribution of minerals controls the pH, a fingerprint of thermodynamic failure, thus is also a pH below 10.5.

2.5 Transport conditions

2.5.1 General remarks

Introducing dynamic porosity/diffusivity in a more elaborate framework, as in the case of multi-component diffusion (MCD) module supplemented in PHREEQC-2.13 is not completely trivial, since it concerns not only the transport properties as encoded by appropriate porosity –diffusivity relations, but also regulates the water content in each cell. In a purely dynamic model with no cut off values all transport and dissolution processes affecting the silo wall would cease within 10,000 to 20,000 years due to the complete clogging of certain cells. The predictions thus obtained would be favourable for the long-term stability, but to some extent also trivial and perhaps not entirely realistic. Analogous to the cut off value employed in porosity-diffusivity for cement to reflect transport through gel pores, it is necessary to ascribe a minimum porosity to maintain minimum content water in the cells. Otherwise the mineral phases would be left dry and neither transport, nor dissolution would occur, although the sole diffusivity would allow transport. A minimum transport condition can therefore be achieved technically through either simply setting a minimum porosity and evaluating a minimum diffusivity from given relations or let the porosity vary freely (between 0 and 1), but use local minimum porosity when evaluating the water content in each cell. The latter method is employed in the modelling of the transport since it to some extent reflects the remaining water bound as gel water in a similar manner as the minimum diffusivity at zero porosity reflects the gel pores.

Unlike previous version of the code, PHREEQC-2.13 has the ability to handle solutes at different diffusion speeds through the multi-component diffusion (MCD) module which includes electro-chemical migration and gradients of the activity coefficients through the following description of the flux, J_i , of specie i :

$$J_i = -d_i \left(\frac{\partial \ln(\gamma_i)}{\partial \ln(c_i)} + 1 \right) \frac{\partial c_i}{\partial x} + d_i z_i c_i \frac{\sum_{j=1}^n d_j z_j \left(\frac{\partial \ln(\gamma_j)}{\partial \ln(c_j)} + 1 \right) \frac{\partial c_j}{\partial x}}{\sum_{j=1}^n d_j z_j^2 c_j} \quad (2-20)$$

where d_i is the diffusivity, γ_i the activity coefficient, c_i the concentration and z_i the valence specie i . In particular the MCD feature would be valuable for the bentonite barrier where the clay is likely to present quite different transport conditions for cations and anions and possibly also promote upgradient diffusion processes. Unfortunately, this feature is not utilized in analysed model because of scarcity of data and the fact that a multi-barrier system would require two sets of diffusivities for each species, which although feasible falls outside the scope of present study.

2.5.2 Porosity

A straightforward approach to address the evolution of the porosity, φ , is to parameterize the porosity in terms of volume changes.

$$\varphi = \frac{V_{void}}{V_{tot}} = \frac{V_{void}}{V_{mineral} + V_{void}} \quad (2-21)$$

Since the aggregate is considered to consist of dense and impermeable material its influence on the porosity is neglected.

For each time-step the volume of all relevant mineral phases is determined and based on the initial total volume the void space is re-calculated. The total mineral volume is allowed to expand beyond the initially evaluated total size of the cell, because this expansion can be interpreted as a measure of the swelling and the tendency to induce fractures. However, the porosity obviously is never allowed to reach below zero and is instead ascribed a lowest nominal value of 0.8 times the initial porosity when evaluating the minimum water content in the cell and thus avoid complete clogging. The chosen value reflects the presumed fraction of capillary water compared to the total water volume in cement /Taylor 1990/.

The variations in porosity due to arising micro-cracks are considered as negligible.

2.5.3 Diffusivity

All relations between the porosity and the capillary diffusivity, d_c , for concrete emphasize the need for incorporating the connectivity between the pores. A relation suggested by /Bentz and Garboczi 1992/ focus on the relation between the hydration percolation thresholds φ_{th} (chosen to 0.16) and the porosity φ as

$$\frac{d_c}{d_0} = 0.001 + 0.07\varphi^2 + H(\varphi - \varphi_{th})1.8(\varphi - \varphi_{th})^2 \quad (2-22)$$

where d_0 is the diffusivity in free water. It is noteworthy that the expression admits remaining non-zero diffusivity even though the porosity reaches zero. A cut-off value, 0.001, reflects the diffusion through the gel pores of the CSH-phase. The relation has been modified by /van Eijk and Brouwers 1998/, which distinguishes between the leaching and the hydration percolation thresholds, however, Equation 2-22 is considered sufficiently adequate to capture the essential features of a porosity-diffusivity variation. Moreover, compared to van Eijks relation it is more numerically robust to the considerable porosity changes the specimen will experience.

The total diffusivity, as mentioned in 2.3.1, will unavoidably embrace emerging fractures, which will be evaluated from the capillary diffusivity through Equation 2-5.

As bentonite is less thoroughly examined and there may be parameters other than porosity that influence the diffusivity, such as the degree of compaction and chemical composition, there are greater uncertainties in the proposed relations between the porosity and the diffusivity. /Suzuki et al. 2004/ suggest a modified version of Archies law

$$\frac{d_c}{d_0} = \beta \varphi^m \quad (2-23)$$

where $\beta = 0.29$ and $m = 2.1$ in the direction parallel to compaction. It should be emphasized that this relation is essentially empirical and the behaviour at extreme porosities ($\varphi = 1$) deviates from what is expected in theory. However, within the moderate changes in porosity the bentonite will undergo the relation is considered to be valid. Similar to concrete a cut-off value of 0.001 is employed in order to avoid complete clogging. The porosity-diffusivity relations for concrete and bentonite are shown in Figure 2-1.

A difficulty introduced by dynamic porosity relates to the gradients of porosity throughout the systems of cells. Since most proposed relations assumes a quadratic dependence, the corresponding gradients of diffusivities will be even steeper, which potentially could result in numerical instabilities, which indirectly impose restrictions on the porosity-diffusivity relations.

The choice of cut-off value for the diffusivity is deliberately chosen quite large in order to avoid complete clogging. Lowering the cut-off value even further would – especially in a multicomponent diffusion transport model – even more explicitly construct a low-porosity barrier at the outer part of the silo-wall leaving the inner quasi-stationary cell almost unaffected. Thus, apart from reflecting transport through gel-pores of the CSH-phase, the selected value for minimum diffusivity also constitutes a conservative choice with respect to the long-term stability.

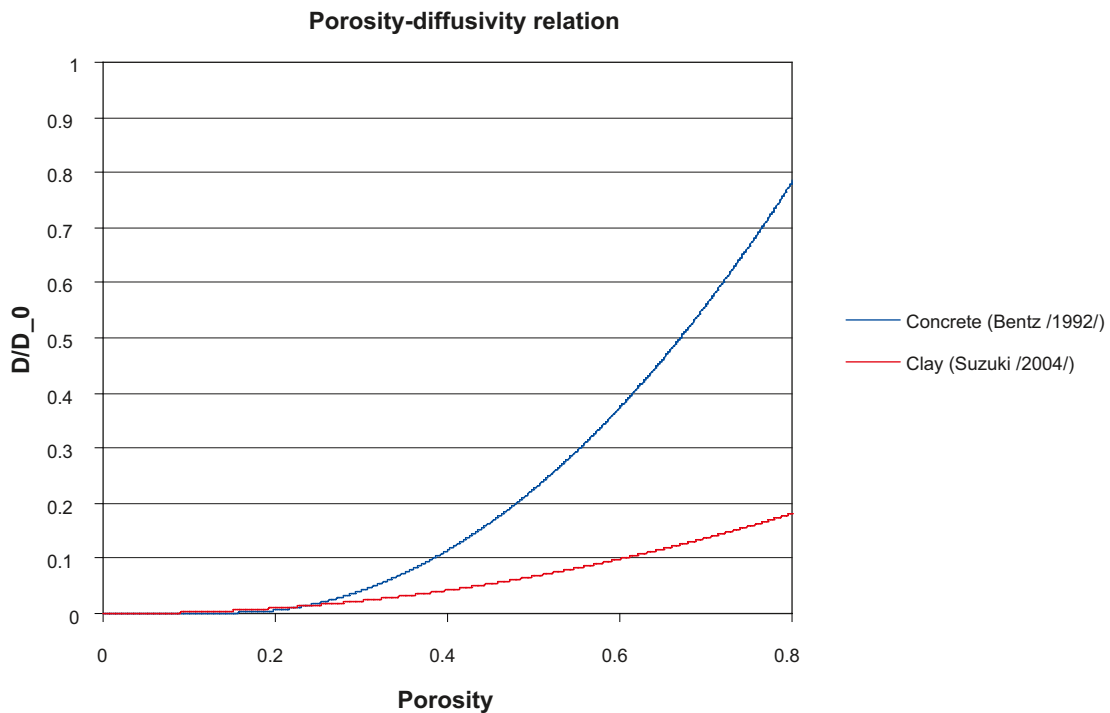


Figure 2-1. Porosity-diffusivity relations for concrete /Bentz 1992/ and bentonite clay /Suzuki 2004/.

2.6 Simulations

For each model there are a variety of parameters that can be altered:

- Temperature, either fixed or varying according to climate scenarios.
- The type of water. Either salt or fresh throughout the analysed period of time or a gradual transformation from salt to fresh.
- The coupling between porosity and diffusivity, either fixed or dynamic as described in Section 2.5.
- Inclusion of fracture mechanics for the cement-based sections of the engineered barriers as described in Section 2.2.
- Inclusion of freeze-thaw effects through a successive increase of the diffusivity for each freezing period as described in Section 2.3. This is referred to as scaled diffusivity in Table 2-3.

In to order evaluate the models sensitivity to each parameter all parameters are initially assessed/addressed as deviations from base case where all parameters are kept fixed (see simulation 1 in Table 2-3) before they are incorporated in a more complete model (as simulation 5-6 in Table 2-3).

2.7 Software

The main tool for modelling the degradation of cement has been PHREEQC-2.13 program /Parkhurst and Apello 1999/ extended by routines that updates temperature and composition of infiltrating water according to given input. PHREEQC is a hydrochemical transport model by D.H. Parkhurst and C.A.J. Apello, which combines 1D-transport mechanisms with thermodynamic equilibrium calculations. The computational scheme applies the local equilibrium assumption (LEA), which states that the chemical reactions are substantially faster than the ion transport. Hence, the transport and the chemical reaction can be treated separately. Thus, a simplified scheme can be sketched through following steps; diffusion transport, thermodynamic equilibrium calculations, volume changes, porosity and diffusivity evaluations.

The multi component diffusion module introduced in version 2.13 represent a major revision from a transport modelling point of view, since it embraces a more elaborate transport equation and foremost enables a dynamical update of the diffusivity. In addition to the standard relation between porosity and diffusivity, Archies law, the program has been supplemented by cement and bentonite specific relations described in Section 2.5.3.

Table 2-3. The computational scheme employed for BMA and the Silo.

Simulation	Temperature	Water chemistry	Diffusivity	Fracture mechanics	Freeze-thaw effects
A	Constant	Salt	Fixed	No	No
B	Varying	Salt	Fixed	No	No
C	Constant	Varying	Fixed	No	No
D	Constant	Salt	Dynamic	No	No
E	Varying	Varying	Dynamic	No	No
F	Varying	Varying	Dynamic	Yes	No
G	Constant	Salt	Scaled	No	Yes

3 Input data

3.1 Models of BMA and the Silo

The models for BMA and the Silo (see Table 3-1 and 3-2) are constructed from a 1D system of adjacent cells in contact with a cell containing the infiltrating water. Whereas the outer boundary condition, as encoded by cell 0, is considered as fixed or varying according to the variation described in Section 2.3, the inner boundary condition is considered as closed and the last cell is only affected by its neighbour to the left. It is emphasized that since the chemical composition of the outer boundary cell representing the ambient water is independent of its neighbours, the conditions conceptually corresponds to an advective flow around the repository, which repeatedly replaces the content of the boundary cell.

3.2 Thermodynamic database

All calculations were performed with the thermodynamic database /ZZ-HATCHES-17 2006/ published by NEA. The cement specific data were validated against those suggested by /Atkins et al. 1992, 1993, Damidot and Glasser 1995, Revertegat et al. 1997/ as cited in /Altmaier et al. 2004/. All solubility products were also in close agreement with those suggested in the thorough review by /Clodic et al. 1997/.

Other mineral specific data, such as molar volumes, were extracted from those employed by CEMHYD3D program /Bentz 2000/ and are explicitly shown in Appendix A. The molar volumes have been validated against CRC handbook by /Weast and Astle 1982/ as well as the report by /Gaucher et al. 2005/.

Table 3-1. The system of cells constituting the model of BMA.

Cell no	Length (m)	Material	Initial porosity
0		Ambient water	
1–4	0.1	Concrete	0.15
5	0.1	Grout	0.3
6–25	0.1	LW&ILW	0.3

Table 3-2. The system of cells constituting the model of the Silo.

Cell no	Length (m)	Material	Initial porosity
0		Ambient water	
1	0.1	Shotcrete	0.15
2–13	0.1	Bentonite	0.61
14–23	0.1	Concrete	0.15
23	0.1	Grout	0.3
25–44	0.1	ILW&LLW	0.3

3.3 Water and temperature variation

The present groundwater conditions are saline, but because of the geological uplift of the area occurring in approximately 5,000–10,000 years, it is necessary to assume a gradual transformation from salt to fresh water. According to SKB climate report TR-06-23 /SKB 2006/ the salinity is expected to decrease down to fresh water composition at approximately year 10,000 and thereafter remain at a low salinity until causes a minor increase (see Figure 3-1). The compositions of the waters are shown in Table 3-3 and reveals that the shift is characterized by a decrease of all species except carbonates.

The considerable discrepancies in anion content will generate quite different mineral dynamics, but since the initial infiltrating water will constitute a front moving inwards, the differences between permanently salt water and a varying water are less dramatic than between a fixed salt and a fixed fresh water.

Table 3-3. The expected water conditions in SFR /Höglund 2001/.

Element specie	Initial saline water (mg/kgw)	Fresh groundwater (mg/kgw)	Saline water under submerged conditions (mg/kgw)
Ca ²⁺	430	35	290
Na ⁺	2,500	100	1,700
Cl ⁻	5,000	45	3,400
CO ₃ ²⁻	100	300	70
Mg ²⁺	270	9	180
SO ₄ ²⁻	500	50	340
K ⁺	20	4	10
Si as SiO ₂ (aq)	5.66	5.9	5.66

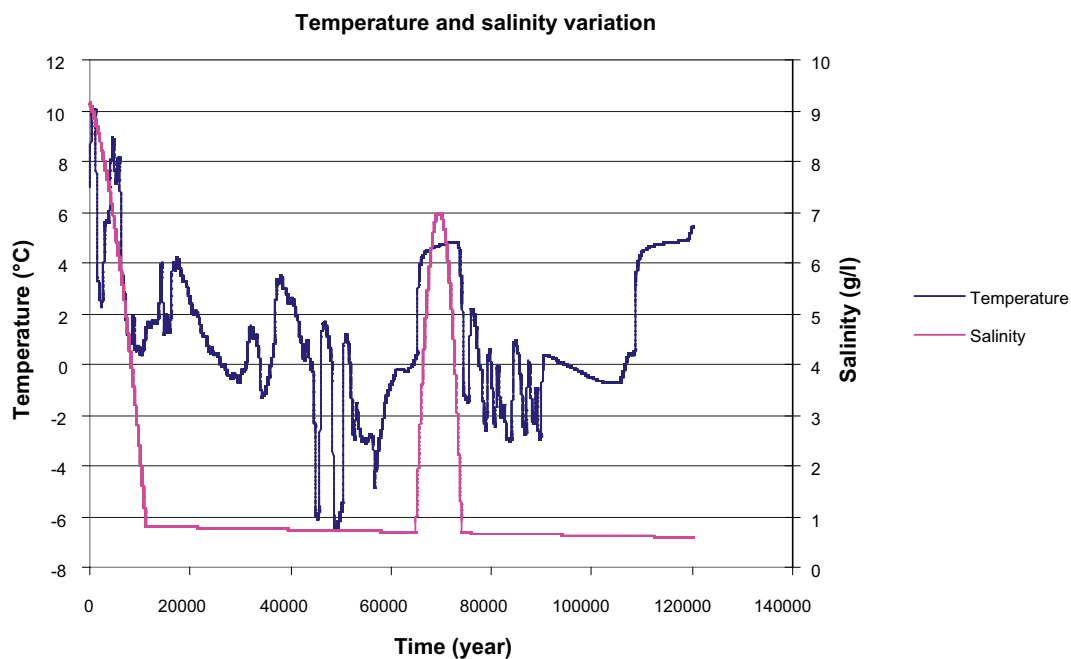


Figure 3-1. Temperature and salinity variation at SFR (from /SKB 2006/).

Although the effects of a non-fixed temperature are considered to be subordinate to the effects of, for instance, the water chemistry or the mechanical damage caused by freezing, a time-dependent temperature is included as a separate parameter of variation (see Figure 3-1).

The first major freezing cycle occurs at year 50,000. In a conservative freeze-thaw scenario the first major freezing cycle occurring at year 50,000 is assumed to destroy the pore-structure of the concrete and the succeeding freezing cycles are therefore within the same scenario considered to act upon a strongly degraded material.

3.4 Concrete/cement

3.4.1 Chemical composition

The presumed compositions of shotcrete, silo-wall (concrete), grout, cement-encapsulated waste (ILW&LLW) and bentonite are shown in Table 3-4 to 3-8 (from /Gaucher et al. 2005/).

Table 3-4. Composition of shotcrete.

Mineral phases	mol	volume %
Quartz	16.605	41.33
Albite	1.771	19.30
K-feldspar	1.437	16.98
CSH _{1,8}	0.932	13.85
Portlandite	0.898	3.22
Ettringite	0.021	1.65
Biotite	0.091	1.39
Hydrogarnet	0.056	0.91
Hydrotalcite	0.007	0.23
Magnetite	0.044	0.21
Friedels salt	0.001	0.03

Table 3-5. Composition of silo-wall (concrete) (w/c 0.47).

Mineral phases	mol	volume %
Quartz	15.096	40.62
K-feldspar	1.307	16.69
CSH _{1,8}	0.847	13.61
Albite	1.067	12.56
Portlandite	0.811	3.14
Ettringite	0.022	1.85
Biotite	0.083	1.36
Hydrogarnet	0.050	0.87
Hydrotalcite	0.008	0.27
Magnetite	0.040	0.21

Table 3-6. Composition of grout (w/c 1.125).

Mineral phases	mol	volume %
Quartz	13.813	44.43
K-feldspar	1.196	18.26
CSH _{1.8}	0.775	14.89
Albite	0.976	13.74
Portlandite	0.750	3.48
Ettringite	0.022	2.19
Biotite	0.076	1.49
Hydrogarnet	0.046	0.98
Hydrotalcite	0.007	0.29
Magnetite	0.036	0.23

Table 3-7. Composition of cement-encapsulated waste (ILW&LLW) (w/c 0.37).

Mineral phases	mol	volume %
CSH _{1.8}	3.522	68.70
Portlandite	3.409	16.05
Ettringite	0.079	8.14
Hydrogarnet	0.219	4.66
Hydrotalcite	0.031	1.35
Magnetite	0.169	1.07

Table 3-8. Composition of bentonite barrier.

Mineral phases	mol	volume %
Montmorillonite-Na	1.498	90.00
Quartz	1.295	7.63
Calcite	0.109	1.04
Phillipsite-NaK	0.006	0.99
Illite	0.005	0.19
Saponite-Ca	0.003	0.12
Magnetite	0.002	0.02

3.5 Mechanical/Fracture parameters

The relevant input parameters from the CEB-FIP-90 model code are summarised in Table 3-9. It is emphasized that the fracture mechanics approach is exclusively applied to the cement-based part of the engineered barriers.

Table 3-9. Various input parameters related to fracture mechanics.

Parameter	Value
E_0	20 GPa
ε_{th}	0.00015
f_t	5.3 Mpa
G_F	156 Nm ⁻¹
w_1	0.024 mm
w_c	0.24 mm
C_1	0.16
C_2	1.2
α_F	0.2
F	0.3

3.6 Transport parameters

The relevant transport parameters are summarised in Table 3-10.

Table 3-10. Various transport parameters.

Parameter	Value
d_o	1.0·10 ⁻⁹ m ² /s
d_c (in scenarios with fixed diffusivity)	1.0·10 ⁻¹¹ m ² /s
φ_{th}	0.16
β	0.29
M	2.1

4 Results

4.1 Silo

4.1.1 A. Base case scenario

Figures B-1 to B-5 display the evolution of the engineered barriers as represented by a selection of snapshots of the cross-sections of the repository at year 0, 1,000, 10,000, 50,000 and 100,000 after the final sealing.

The structural integrity of the concrete wall is in the base case scenario with fixed transport conditions predicted to maintain throughout the analysed period of time. The $\text{CSH}_{1.8}$ in the silo-wall appears to be intact at depth of 50 cm and the content of portlandite in the silo-wall is not completely depleted until year 50,000.

Concerning cement-encapsulated waste, the leaching of portlandite has reached approximately 20 cm into the cement-encapsulated waste and $\text{CSH}_{1.8}$ remains unaffected. Considering this low leach depth, the waste appears virtually unaffected even at year 100,000.

The transformation of the bentonite progresses at an even slower pace than the concrete. Whilst the main structural provider for concrete at year 10,000 has eroded 40 cm from the outer boundary, the bentonite still consist of at least 90% Na-montmorillonite. The bentonite layer will be attacked from two directions, both from the infiltrating water and the high pH water with Ca and OH leaching from the concrete. Figure B-2, which represents the degradation at year 1,000, demonstrates that initially the transformation to phillipsite occurs on both sides of the bentonite layer, however, as seen from Figures B-3 to B-5, the subsequent evolution is more moderate at the outer boundary facing the shotcrete, than the boundary in contact with the silo-wall. Obviously this coincides with the rapid dissolution of the shotcrete. Whereas the inner boundary continues to transform to phillipsite (both Na and K) and katoite and causes a porosity reduction, the outer boundary show a rather constant porosity with minor transformation to illite.

4.1.2 B. Varying temperature

The accelerating/deceleration of thermodynamic aging effects imposed by a varying temperature can be assessed through a comparison between the figures from the base case scenario (Figures B-2 to B-5) with Figures B-6 to B-9. Although, the deviations between the two sets of figures are not particularly significant, is possible to distinguish a net deceleration effect from year 50,000, in particular considering the transformation of $\text{CSH}_{1.8}$ to $\text{CSH}_{1.1}$ in the silo-wall. Another difference relates to the precipitation of minerals in the interface between bentonite and the silo-wall, however, the overall conclusion is that temperature, as expected, is a parameter of minor importance.

4.1.3 C. Varying salinity

Although it is complicated to predict the long-term variation of the ambient water, the essential features of the changes can be addressed through the salinity variation depicted in Section 3.3. The main uncertainty of the salinity variation relates to the parabola at between year 65,000 and 74,000 corresponding to submerged conditions for the repository. However, with respect to the performance assessment, the salinity increase and the perturbation of the corresponding equilibrium achieved, is considered a slightly more conservative scenario than fixed fresh water. Moreover, since the water change occurs at such a late stage, the major effect will be confined to regions of the repository already substantially degraded. The inner un-degraded regions will not be able to be exposed to the new front of high-saline water within the analysed period of time.

From a comparison between Figures B-2 to B-5 and Figures B-10 to B-13, it is clear that the type of the ambient water has a significantly higher impact on the degradation of the barriers, than the temperature variation. Already at year 10,000 (see Figure B-11) the distribution of minerals at the interface between shotcrete and the bentonite layer deviates significantly from the scenarios with fixed water composition. Whereas the scenario with varying water composition shows a substantial porosity decrease due to precipitation of phillipsite, the fixed water scenarios show a slight decrease in porosity characterized by a moderate precipitation of illite and saponite. At a later stage the degradation also includes transformation from montmorillonite-Na to montmorillonite-Ca.

The precipitation of phillipsite is even more pronounced at the interface between bentonite and the silo-wall where porosity drops to 0.10 at year 100,000. Clearly, this rapid precipitation process will have a substantial influence on various mechanical properties, such as the occurrence of fractures that could accelerate the degradation even further.

Nevertheless, throughout the analysed period of time, the degradation of the silo-wall progresses at a similar rate and yields a similar mineral distribution for cells representing the interior part of the silo-wall. This feature is partly a consequence of the fact that cement-based materials are completely dominated by portlandite and CSH with only a limited option of dissolution paths. Notwithstanding the gradual decrease of salinity, the water composition at such depths is also largely influenced by the composition of the initially infiltrating water. Thus, a major impact on the leaching depth can be traced back to the initial front of salt water that enters the barriers.

4.1.4 D. Dynamic diffusivity

On a rough scale, the major implication of a dynamic diffusivity can be associated with altered transport conditions at the two interfaces between bentonite and cement-based barriers. An increased diffusivity can be expected at the interface between shotcrete and bentonite and a decreased diffusivity at the interface between bentonite and silo-wall.

At year 1,000, (see Figure B-14) there are minor differences, perhaps most striking is the symmetrical transformation of montmorillonite-Na to montmorillonite-Ca in the dynamic diffusivity scenario. Even at year 10,000, (see Figure B-15) the differences compared to a fixed diffusivity scenario are not particularly significant and are confined to minor deviations in terms of $\text{CSH}_{1.8}/\text{CSH}_{1.1}$ transformation and the ingress of katoite in the phillipsite peak near the interface between bentonite and the silo-wall in the fixed diffusivity scenario. At year 50,000 and year 100,000, (see Figure B-16 to B-17), again the deviation relates to the interfaces between two barriers. Whilst in the fixed diffusivity scenario, the phillipsite-peak is maintained and the interface between eroded shotcrete and bentonite seems rather unaffected, the dynamic diffusivity shows the opposite behaviour. Whereas the outer boundary of bentonite barrier is dominated by strong phillipsite-peak, the inner boundary now is populated by minor fractions of illite and saponite. The once overwhelming phillipsite peak appears to be dissolved.

Concerning the silo-wall, the $\text{CSH}_{1.8}/\text{CSH}_{1.1}$ transformation has not reached the same depths as in fixed diffusivity scenarios and a small fraction of portlandite remains.

Overall, the degradation of the outer boundary is accelerated because of the early erosion of shotcrete, whereas for interior cells the degradation rate is reduced.

4.1.5 E. Dynamic model

A model incorporating temperature and salinity variations as well as dynamic diffusivity will derive features from all scenarios. Up to year 10,000, (see Figure B-19) the completely dynamic model shares the main characteristics with the scenario including salinity variation, with a fairly symmetric precipitation of phillipsite-Na. At year 50,000, (see Figure B-20) the varying water composition still exercises the strongest influence, with the decoupling of the phillipsite-Na peak in the interface between bentonite and the silo-wall and the gradual transformation of the

phillipsite peak at the interface between shotcrete and bentonite as distinct fingerprints. The effect of a dynamical diffusivity is most evident as a minor reduction of the $CSH_{1,8}/CSH_{1,1}$ transformation depth.

Overall, Figures B-18 to B-21 demonstrate a significant acceleration of the degradation of the bentonite barrier, which could have serious implications for the transport through the bentonite barrier, through, for instance, fracturing, which indirectly could affect the dissolution rate of the entire silo-wall that otherwise appear to withstands the attack of infiltrating water throughout the analysed time period.

4.1.6 F. Fracture model

Since the fracture mechanics model is based on theory developed for specimens subjected to mechanical strain, the effects are rather harsh, as seen in Figures B-22 to B-25. The model predicts a rupture through the entire silo-wall already at year 20,000, which have severe consequences for both the thermodynamic stability and the transport conditions. Already at year 10,000 the leaching of portlandite have reached levels that in other scenarios corresponds to the degraded state at year 100,000. The similar level of acceleration is manifested in the strong and decoupled peak of phillipsite. At year 100,000 the bentonite barrier is completely degraded and although the silo-wall still consists of $CSH_{1,8}$, this may be attributed to the fairly realistic re-precipitation of $CSH_{1,8}/CSH_{1,1}$ due to massive release of Ca. As the results are rather extreme, they are difficult to interpret and validate. The overall conclusion is therefore not insomuch quantification, than a qualitative observation that if fractures occur, probably after year 10,000, their influence can potentially affect all attained predictions substantially.

4.1.7 G. Freeze and thaw effects

Unlike dynamic diffusivity, the diffusivity changes caused by freeze-thaw effects are modelled as related to the entire cross section, although confined to cementitious material. Since the major freezing cycles and the corresponding diffusivity shifts first occur almost half-way through the period of time considered there are no major deviations from the fixed diffusivity scenario until snapshot taken at year 50,000 (see Figure B-28). However, starting from the first freezing cycle, the degradation is significantly accelerated. The bentonite barrier reaches the same degree of degradation as the end degradation in fixed diffusivity scenarios even before year 50,000. A substantial part of the montmorillonite-Na has been transformed to montmorillonite-Ca and montmorillonite-Mg. As expected, Figures B-26 to B-30, show that the freeze-thaw cycles has an enormous impact on the degradation rate.

The accelerated dissolution mechanisms lead to numerical convergence problems which causes the program to terminate at year 81,000. The last available snap shot of the cross section of the engineered barriers therefore relates to year 80,000. As seen in Figure B-33, the bentonite barrier has completely eroded and due to the massive release of numerous species the model clearly is beyond the limit of validity. Although the predictions for the degradation beyond year 50,000 are highly uncertain, it is evident that the mechanical effects from the freeze-thaw cycles have a severe impact on the thermodynamic state of the barriers. The dissolution process after the first freezing cycles will be rapid and uncontrolled.

4.1.8 Comparison between scenarios regarding porosity and pH

Figures B-30 to B-33 display the porosity distribution within the cross-section of the repository at year 1,000–100,000. The mutual deviations within the set of scenarios are visible from year 10,000, especially around the interface between the bentonite barrier and the silowall. Whereas all fixed diffusivity scenarios show a porosity peak adjacent to the porosity drops at distance 1.35 m from the outer border, the dynamic diffusivity are characterized by a smoother transition. Without the smoothening effect from dynamic diffusivity, fixed transport conditions generate a partially accelerated degradation mechanism in some cells due to leaching and

deceleration in some cells due to precipitation. This will create zones within the barriers with either enhanced leaching or enhanced clogging. The excess of ions leaking from a cell characterized by extensive leaching, may precipitate in the neighbouring cell and thus create entrapment where aging kinetics is further accelerated.

There are no significant porosity differences between the different scenarios for the innermost part of the repository, i.e. the cement-encapsulated waste.

In comparison with the porosity, the pH deviations within the set of scenarios are easier to interpret. Already at year 10,000, the decay of salinity of the infiltrating water causes an increase of pH in the bentonite layer, which also is reflected in the transformation of montmorillonite to phillipsite. Whereas for scenarios with fixed salinity of infiltrating water, the pH remains around 8.5 throughout the considered period of time, for varying salinity the pH is already at year 10,000 above 10 and before year 100,000 the pH reaches 11 for the entire bentonite layer. Considering the predicted state of the montmorillonite, this may indicate that the applied database underestimates the transformation of montmorillonite and/or a kinetic approach may be better suited to describe this transformation.

Starting from year 50,000, the pH curves are clustered around either scenario A, B and D or C and E, which demonstrates that the water composition of the infiltrating water is the most influential parameter. Although less explicit shown, the same conclusion can be derived from the corresponding porosity curves. It is also noteworthy, that mutual deviations within the set of porosity curves perhaps is most pronounced in the middle period, i.e. between year 10,000 and year 50,000. The set of final porosity curves at year 100,000, are in more mutual agreement.

4.2 BMA

4.2.1 General remarks

For BMA the porosity gradient and the corresponding diffusivity gradient were prone to cause convergence problems in the subsequent thermodynamic equilibrium calculations. In order to resolve the numerical instabilities, the exponent in Equation 2-22 was reduced to 1.2, to establish a more linear relation and a more moderate diffusivity gradient. Although this is a fairly brute way to achieve convergence, it is not believed to affect the qualitative behaviour of the predictions. In fact, the mutual agreements between the results obtained for the Silo with and without dynamic diffusivity, indicate the effects from a fine-tuning of the porosity-diffusivity relation is subordinate to the changes in water composition. The fracture scenario represents an exception since the difference between a solid and a fractured cell had to be reduced by a factor 10 in order to reach convergence. Thus, the effects from fractures are not sufficiently aggressively modelled and the obtained predictions far to modest.

4.2.2 A. Base case scenario

In the base case scenario, where temperature, infiltrating water and diffusivities are kept fixed, the concrete wall appears to maintain structural integrity throughout the considered period of time, 100,000 years (see Figures B-38 to B-42). Although the concrete wall already at year 10,000, is completely depleted of portlandite, the $\text{CSH}_{1.8}/\text{CSH}_{1.1}$ transformation has not reached the innermost cell of the concrete wall facing the cement-encapsulated waste. An additional relevant mechanism is the delayed formation of ettringite, which coincides, with the dissolution of portlandite and causes significant porosity changes. For the concrete wall the formation of ettringite is confined to the initial 5,000 years, whereas for the cement-encapsulated waste the process reaches the outer border facing the concrete wall at year 10,000 and progresses further into the waste. At year 100,000, the ettringite formation as well as the portlandite dissolution has reached approximately 70 cm into the waste.

For the concrete wall, the late precipitation of hydrotalcite contributes to final porosity drop down to zero.

4.2.3 B. Varying temperature

As for the Silo, temperature is a parameter with only minor direct influence on the degradation process. As seen in Figs 43–46, the evolution in the scenario with fixed diffusivity and water composition, but variable temperature follows the scenario with fixed temperature closely. At year 100,000, the mutual deviation is restricted to a slightly delayed $CSH_{1.8}/CSH_{1.1}$ transformation, otherwise all relevant mineral dissolution is almost identical.

4.2.4 C. Variable salinity

Compared with the silo, the effects of varying water composition seem to be less influential as displayed by Figures B-47 to B-50. Apparently, the bentonite is more sensitive to the composition of the ambient water. Another striking feature relates to the formation of ettringite, which unlike the scenario with fixed water composition primarily is found in the concrete wall. Whereas the ettringite formation appears to be more pronounced for the concrete wall than in the fixed water composition scenario, the process is absent in the cement-encapsulated waste.

4.2.5 D. Dynamic diffusivity

From the inspection of Figures B-51 to B-54 it appears as if introducing dynamic diffusivity has the effect of accelerating the transformation of $CSH_{1.8}$ to $CSH_{1.1}$, but decelerating the leaching of portlandite. However, as Figures B-54 depict, at year 100,000 the leaching depth for portlandite is almost the same as for the scenario with fixed diffusivity, whereas the $CSH_{1.8}/CSH_{1.1}$ transformation appear to remain stationary in the scenario with dynamic diffusivity. Clearly the porosity drop occurring after year 10,000 in the frontier cells of the concrete wall, strongly reduces further migration into the matrix. This initial front, however progresses through the concrete wall and continues to accelerate the leaching. The effect may be slightly underestimated because of the downscaling of the porosity-diffusivity relation, but the results obtained for the Silo as well as the deviation between fixed and variable diffusivity for BMA indicates that the major features should be captured even with a reduced porosity-diffusivity relation.

4.2.6 E. Dynamic model

A completely dynamic model combines the varying water and temperature with dynamic diffusivity. As neither of the effects has shown to exercise a substantial influence, the combined result is in accordance with the result obtained with completely fixed transport conditions (see Figures B-55 to B-58). The final state at year 100,000 exhibit a similar depth of portlandite depletion as the other scenarios and similar $CSH_{1.8}/CSH_{1.1}$ transformation depth as the dynamic diffusivity scenario. The suppression the otherwise distinct peak of ettringite formation is in accordance with the fixed diffusivity and varying infiltrating water.

4.2.7 F. Fracture model

It is clear from Figure B-59 to B-62, that the scaled down version of the fracture model is in to much agreement with the scenario D and E, to be able to fully address the impact of fractures. Nevertheless, from year 50,000, the traces of re-formation of $CSH_{1.1}$ indicates that the present transport conditions exceeds the limits of the model.

Unlike the previous scenarios, the fracture model predicts a collapse of the entire concrete wall before year 50,000 (see Figures B-59 to B-62). The portlandite depletion depth exceeds the length considered in the model and the $CSH_{1.8}/CSH_{1.1}$ transformation reaches 1 m into the waste. This corresponds to a situation where the waste is completely exposed to infiltrating water before year 50,000.

4.2.8 G. Freeze and thaw effects

Similar to fractures, freeze-thaw cycles have a significant influence on the degradation process. As seen in Figures B-63 to B-66, the degradation from the first freeze-thaw cycle is substantially accelerated. Already at year 50,000, the Silo wall is completely eroded, but again the reformation of $\text{CSH}_{1,1}$ clearly indicates that the model is beyond what can be regarded as realistic.

4.2.9 Comparison between scenarios regarding porosity and pH

All major deviations between the porosity curves of scenarios A–D in Figures B-67 to B-70 are related to the formation of ettringite, either in the first frontier cells of the concrete wall or in the interface between the cement-encapsulated waste and the grout. Whilst scenarios with variable water composition predict a decreasing porosity due to formation of ettringite for the first initial cells at year 10,000, the other scenarios suggest a porosity decrease. This is in contrast to the situation at year 50,000, where the same scenarios, C and E, are distinguished by not predicting a peak of late ettringite formation. In conclusion, scenarios with fixed water composition show a stronger, but delayed formation of ettringite confined to the cement-encapsulated waste.

Unlike the porosity, the pH-curves in Figures B-71 to B-74 are all in close agreement. All scenarios with fixed diffusivity almost overlap each other, whereas the scenarios based on dynamic diffusivity show a slight deviation, which indicates that although porosities may vary, the content of the essential and pH-controlling mineral phases are almost the same. Thus, in an entirely thermodynamic picture, all scenarios agree on the long-term stability, but the critical aspect relates to the potential influence of fractures.

5 Comments and conclusions

5.1 General remarks

Extensive modelling has been performed on various degradation processes assumed to critically affect the long-term safety of the Silo and BMA at SFR. It is demonstrated that the direct impact of temperature variation through regulating the rates of chemical reactions, is not significant. Of more importance are effects related to the infiltrating water. However, the implications for the actual degradation depth are not substantial. The reason for this is a combination of two effects. Since it will be the initial ambient water that will constitute the invasive front, the effects of subsequent variation of the water, i.e. decreased salinity, mainly will be confined to the outer parts of the repository. Moreover, as the degradation of the inner part of the repository largely concerns the dissolution of portlandite and CSH, which in turn is determined by the leaching of Ca and OH, the infiltrating water has only indirect effects on the depth of degradation. Among these indirect effects, clearly, porosity changes and the corresponding changes of transport conditions are the most important. From a comparison between calculations with fixed and dynamic diffusivity, it is evident that by introducing dynamic diffusivity, degradation of the outer parts of the repository is accelerated, whilst for the inner regions the degradation is decelerated. In particular the dissolution of portlandite is retarded compared to scenarios with fixed diffusivities.

It is notable, that irrespective of the inclusion or exclusion of temperature and/or salinity variation and a dynamically updated diffusivity the calculations are in mutual agreement concerning the depth of the degradation.

A more substantial acceleration of the aging processes is achieved by the inclusion of fractures or freeze-thaw effects. However, the freeze and fracture scenarios should merely be considered as a tentative approach with the aim to illustrate that fractures and freezing effects could be dramatic, not that they actually will be. Substantial amount of experimental work are required in order to parameterize models including fractures.

5.2 Silo

Most calculations support the view that the silo wall will only be degraded half way through if employing the failure criterion described in Section 2.4. The major differences between results from the scenarios are confined to the outer part of the repository, in particular the interface between the bentonite barrier and either the shotcrete or the silowall. Since the core of the bentonite layer is predicted to remain intact, the presumed impact of zeolitisation and subsequent embrittlement can be considered as local effects with uncertain influence on the overall degradation depth. Certainly, the zeolitisation process would be further accelerated if the transformation from montmorillonite were accompanied by fractures, however this process would occur at such late stage of degradation, that the leaching depth within the concrete would probably not be substantially increased. A non-degraded bentonite will clearly not be subjected to fractures because of its inherent plasticity.

An overall conclusion is that the results obtained within the set of scenarios are not particularly sensitive to the variation of input parameters or the inclusion of dynamic diffusivity. In all scenarios, the structural integrity of at least half of the silowall is maintained throughout the 100,000 years, although the porosity of the entire silowall has reached zero.

The potential events that theoretically could exercise the strongest influence on the long-term stability are related to fractures and/or freeze-thaw cycles. Although somewhat crude and

adapted to a mechanical rather than a chemically induced strain, the fracture model employed illustrates that fractures can pose a serious threat to the long-term stability of any repository. The present formulation may be immature and clearly in need of further empirical input, however it still demonstrates that rapid changes in transport conditions, irrespective of origin, critically accelerate the degrading processes. Further research should therefore focus on investigating the nature of porosity changes and their impact on the mechanical properties, such as their ability to induce fractures and their function in ultimately determining the transport conditions.

5.3 BMA

As for the silo, the predictions are relatively stable to the presumed variation of input parameters. Neither variation of temperature, and/or salinity, nor the dynamic diffusivity alters the main conclusions derived from the base case scenario, i.e. the concrete wall is only partially degraded below the failure criterion in Section 2.4.

As for the Silo, emerging fractures and freeze-thaw cycles appear to be the events, which seriously can alter the attained predictions by substantially revising the transport conditions. However, it is again emphasized that the present model merely points out the some of the possible consequences of fractures, rather than actually numerically addressing a full-scale scenario including fractures.

5.4 Uncertainties

5.4.1 Uncertainties of various input data

Although there are alternative descriptions of the cement-based barriers (shotcrete, the silo-wall, the grout and the cement-encapsulated waste) and the distribution between the major mineral phases can be varied, the essential degrading mechanisms, i.e. dissolution of portlandite and CSH as caused by the leaching of Ca, can be captured by the selected phases. Thus, within reasonable variations of the cement recipe, the key features of the degradation are not expected to vary substantially. The same conclusion applies for geometric dimensions of the repository.

Because concrete is dominated by aggregates, it is often assumed that concrete will show an increased tortuosity compared to pure cement. However, presence of aggregates will construct an interfacial zone between the aggregate and the paste with a higher porosity than bulk paste, which may counter balance the effects the net effect on the transport conditions. Although the interfacial transition zone (ITZ) will be thicker for concrete with high w/c, the compensation appears to justify an identical conceptual treatment of cement and concrete.

As the hydration process is often incomplete, remaining cement clinker grains may retard the dissolution rate, but this effect is likely to be of minor importance considering the extremely long-term perspective.

Notwithstanding the uncertainties related to the barriers, the input data with the probably greatest influence on the final result is the infiltrating water. Unlike the uncertainties related to the cement, the uncertainties related to the infiltrating water are implicitly addressed through a comparison between the two scenarios based on a fixed diffusivity and with or without variation of the water chemistry. Since it is the initial batch of saline water that will progress inward, the depth of the leaching process largely will be determined by the initial front of water, which is rather well characterized compared to the long-term evolution. It is evident from performed calculations that the major degrading scheme and depth is retained in both scenarios which indicates that the influence of uncertainties associated with water composition mainly affects the character of the degradation, rather than the actual leaching depth.

5.4.2 Uncertainty due to the thermodynamic database

The present understanding of concrete is not by any means complete and the approach does not account for unresolved conceptual uncertainties. Thermodynamic databases are clearly compiled from data originating from numerous experiments, each of them subjected to different experimental strategies and subsequent interpretation. For instance calcium ferri hydrates are neglected and various meta-stable phases are in general not addressed.

As described in Section 1.4, there are alternative methodologies to depict the gradual transformation of CSH, however preliminary calculations have shown that the same qualitative behaviour along with the same degree of conservatism can be achieved within both types of approaches. Another uncertainty is posed by the predictions of re-formation of various CSH phases at extreme conditions. This is probably not realistic, but does only affect cells suffering from strongly exaggerated transport conditions, as the occurrence of fractures, where the cell already is strongly degraded.

Although an extensive kinetic description of the relevant cement-specific mineral phases would improve the scientific foundation, this does not necessarily imply that the present approach and estimates obtained are less conservative. Hence, a rigorous comparison between the outcomes of different databases would be valuable, especially in conjunction with a comparison with an entirely kinetic approach. However, it is beyond the scope of this report to critically assess the merits of different databases.

The thermodynamic description of bentonite is in general considered likewise incomplete, in particular, since clay dissolution is believed to follow an Ostwald step sequence. Clearly, dissolution kinetics represents a more sophisticated approach, but could potentially introduce numerical instabilities. In spite of the conceptual advantages of a kinetic approach, a well-tuned database should be able to mimic the essential dissolution features, or at least be able to present a conservative estimate.

A particular issue considering the clay relates to zeolitisation, which could lead to embrittlement and fracturing of the bentonite barrier, although such effects could be incorporated easily into the model by assessing fractures, or simply by modifying diffusivities, whenever the content in the clay cells reach a certain threshold distribution. However, lack of experimental data makes further attempts in this direction questionable. Overall, considering the incomplete state of knowledge for the long-term behaviour of montmorillonite, there may be several sources for underestimation of the detrimental processes of the clay. Moreover, considering the height of the Silo and the compressive force exercised by gravity it appears unlikely that fractures should occur in a non-rigid structure as the bentonite barrier, even though suffering from considerable mineral transformations. Substantial porosity changes in combination with a pressure gradient should create a void on top of the clay cylinder rather than complete ruptures through the wall.

Another, although probably less influential, issue relates to the fact that the database is compiled at 25°C, and scaled to other temperatures through given enthalpies. Nevertheless, the insignificant differences in the results obtained by the scenarios with fixed diffusivity, with and without temperature dependence, reflect the widely expected weak temperature dependence.

The kinetic description of the dissolution of the ballast is clearly incomplete by excluding pH and distance to equilibrium and can be improved by accurate experimental data specially adapted to the high pH cement environment. However, more advanced kinetics in combination with the stepwise dissolution of CSH can again potentially introduce numerical instabilities with further requirements for step length etc.

5.4.3 Uncertainty due to the transport model

The multi-components module introduced in version 2.13 of PHREEQC represents a substantial improvement compared with previous versions. Although the model multi-component transport module allows non-uniform diffusivities, the present study has assumed a single diffusivity in

free water valid for all species. Although the transport model would be improved by the use of accurate diffusivities, their effect is assumed to be insignificant, because the mutual differences between diffusivities in free water for the major ions are not much larger than their individual uncertainty. It is more likely that the parameterization of the diffusivity in terms of porosity is a greater source of uncertainty, especially since the model relies on a single diffusivity-porosity relation irrespective of the type of ion. Even though this may be correct from a geometric point of view, it neglects various inter-ion effects, such as ion exchange etc. that may suggest that there should be different types of diffusivity-porosity relations for anions than for cations. However, any attempts to incorporate such relations would be questionable, without relevant data.

It is also doubtful whether the proposed porosity-diffusivity relations for concrete still apply for specimens subjected to late stage re-crystallisation. The model assumes implicitly that the calculated gross volume changes will occur on top of pre-existing pore-structure. It is likely that the initial precipitation will occur in prevailing pore structure; however the dissolution of CSH along with precipitation of various other mineral phases might create a new pore structure. Although the porosity-diffusivity relation for BMA had to be scaled down from quadratic to semi-linear relation, the moderate differences between a fixed and a dynamic diffusivity for the Silo indicate that the actual relation between porosity and diffusivity are of minor importance as long as they reflect the fundamental fact that a decrease in porosity should correspond to a decrease in diffusivity.

The ion transport through clay is even less understood than the transport through cement-based materials, in particular since clay in general often exhibits ion-exchange capacity. Therefore the uncertainty associated with the proposed porosity-diffusivity relation is probably less influential than uncertainty introduced by the transport model per se. A more sophisticated approach incorporating diffuse double layer (DDL) could resolve such issues, but will be even more dependent on validated input data.

Non-fixed porosities and diffusivities will unavoidably introduce a dependence on step-length, which in principle calls for some self-consistent approach. However, preliminary calculations show only a weak dependence on the actual step-length, which clearly also is in agreement with the comparably small deviations between fixed and non-fixed diffusivity.

The model does not distinguish between horizontal versus vertical direction of mass transport, mainly because for migration of ions in the engineered barriers gravity clearly is subordinate to diffusive processes. The direction of transport becomes important only for advection.

The fracture mechanics model should be considered as a preliminary work in progress in order to explore the general implications on thermodynamic stability caused by fracturing, rather than providing accurate predictions of the fractures per se. Since it is based on the tensile response due to externally applied strain, not internal swelling pressure, the fracture mechanisms can be expected to deviate substantially. In sharp contrast to the ordinary fracture mechanics, where the specimen is chemically intact, the swelling pressure is mediated through the gradual transformation of relevant mineral phases and precipitation in capillary pores, i.e. the elongation is accompanied, or even caused by, various chemical transformations. To some extent, the major uncertainty might therefore relate to the evaluation of the strain itself, rather than the actual response to the strain. A more complete model would therefore necessarily take into account the individual behaviour of each of the precipitating mineral phases and their effect on the tensile response.

5.4.4 Overall uncertainty

Although several sources of uncertainty have been identified and evaluated (see Table 5-1), the mutual agreement of the obtained predictions clearly manifests an internal stability within the approach. The only sources of uncertainty that appear to have a significant impact on the final performance assessment of the repository are those related to fracturing, either caused externally by freeze-thaw processes or through a swelling pressure inferred from precipitation of certain mineral phases in pre-existing micro-cracks. Irrespective of their origin, fractures clearly affect the structural integrity per se, but foremost also create more generous transport conditions, which further accelerate the overall aging process. Thus, it is essential to further investigate the role of fractures in order to improve the accuracy and applicability of the attained predictions.

Table 5-1. A summary of critical input parameters, the method applied to address their implications, their presumed uncertainty and their presumed influence.

Critical parameter	Means of addressing	Uncertainty	Influence
Dissolution/solubility of components	Thermodynamic database	Small	Large
Initial concentration of mineral phases	Input data	Small	Small
Kinetics for dissolution of ballast	Simplified relation for reaction rates	Large	Small
Initial porosity and ion diffusivity	Input data	Small	Small
Porosity-diffusivity relation	Separate relations for clay and concrete	Large	Small
Temperature	Re-constructing temperature from given enthalpies	Small	Small
Water composition	Input data (fixed and time dependent compositions)	Large	Small
Internal erosive forces and physical properties of the leached alteration product	Fracture mechanics	Large	?
Freeze-thaw effects	Successive diffusivity decreases	Large	?

6 References

- Altmaier M, Brendler V, Bosbach D, Kienzler B, Marquardt C, Neck V, Richter A, 2004.** Geochemische Prozesse bei der Ausbreitung von Schadstoffen aus einem Endlager für radioaktive Abfälle, Final report, FZK-INE 002/04, Forschungszentrum Karlsruhe, Germany.
- Atkins M, Bennett D G, Dawes A C, Glasser F P, Kindness A, Read D, 1992.** A thermodynamic model for blended cements, *Cement and Concrete Research*, 22, 497–501.
- Atkins M, Glasser F P, Moroni L P, Jack J J, 1993.** Thermodynamic modelling of blended cements at elevated temperature (50–90°C), Report No DoE/HMIP 94.011, DoE, UK.
- Bentz D P, Garboczi E J, 1992.** Modeling the Leaching of Calcium Hydroxide from Cement Paste: Effects on Pore Space Percolation and Diffusivity, *Materials and Structures* 25, 523–533.
- Bentz D P, Quenard D A, Baroghel-Bouny V, Garboczi E J, Jennings H M, 1995.** Modelling drying shrinkage of cement paste and mortar, Part 1. Structural models from nanometres to millimetres, *Materials and structures*, 28, 450–458.
- Bentz D P, CEMHYD3D, 2000.** A Three-Dimensional Cement Hydration and Microstructure Development Modelling Package. Version 2.0 NISTIR 6485, U.S. Department of Commerce.
- Berner U R, 1988.** Modelling the incongruent dissolution of hydrated cement minerals, *Radiochim. Acta.*, 44/45, 387–393.
- Brown P W, Lacroix P, 1989.** The kinetics of ettringite formation, *Cement and Concrete Research* 19 (6), 879–884.
- CEB-FIP 90 model code, 1993.** Thomas Telford London, ISBN 0-7277-1696-4.
- Chen J J, Thomas J J, Taylor H F W, Jennings H M, 2004.** Solubility and structure of Calcium Silicate Hydrate, *Cement and Concrete Research* 34, 1499–1519.
- Clodic L, Meike A, 1997.** Thermodynamics of Calcium Silicate Hydrates, Lawrence Livermore National Laboratory, UCRL-ID-132088.
- Damidot D, Atkins M, Kindness A, Glasser F P, 1992.** Sulphate attack on concrete: limits of the AFt stability domain, *Cement and Concrete Research* (22), 6, 229–234.
- Damidot D, Glasser F P, 1993.** Thermodynamic investigation of the CaO- Al_2O_3 -CaSO₄-H₂O system at 25°C and the influence of Na₂O. *Cement and Concrete Research* (23), 6, 221–238.
- Damidot D, Stronach S, Kindness A, Atkins M, Glasser F P, 1994.** Thermodynamic investigation of the CaO- Al_2O_3 -CaCO₃-H₂O system at 25°C and the influence of Na₂O. *Cement and Concrete Research* (24), 563–572.
- Damidot D, Glasser F P, 1995.** Thermodynamic investigation of the CaO- Al_2O_3 -CaSO₄-CaCO₃-H₂O, *Advances in Cement Research* (27), 129–134.
- Emborg W, Jonasson J E, Knutsson S, 2007.** Långtidsstabilitet till följd av frysning och tining av betong och bentonit vid förvaring av låg- och medelaktivt kärnavfall i SFR 1, Svensk Kärnbränslehantering AB, (to be published).
- Famy C, Brough A R, Taylor H F W, 2003.** The CSH-gel of Portland cement mortars: Part I. The interpretation of energy dispersive X-ray microanalyses from scanning electron microscope, with some observations on CSH, AFm and AFt phase compositions, *Cement and Concrete research*, 33, 1389–1398.

- Fukuhara M, Goto S, Asaga K, Daimon M, Kondo R, 1981.** Mechanisms and kinetics of C4AF hydration with gypsum Cem. & Conc. Res Vol 11, 407–414.
- Gartner E M, Jennings H M, 1987.** Thermodynamics of calcium Silicate Hydrates and their solutions, Journal of American Ceramic Society, 70, 743–749.
- Gaucher E, Tournassat C, Nowak C, 2005.** Modelling the geochemical evolution of the multi-barrier system of the Silo of the SFR repository. SKB R-05-80, Svensk Kärnbränslehantering AB.
- Höglund L O, 2001.** Project SAFE, Modelling of long-term concrete degradation processes in the Swedish SFR repository. SKB R-01-08, Svensk Kärnbränslehantering AB.
- Jennings H M, 1986.** Aqueous solubility relationships for two types of Calcium Silicate Hydrate, Journal of American Ceramical Society, 69, 614–618.
- Jennings H M, 2000.** A model for the microstructure of calcium silicate hydrate in cement paste, Cement and Concrete. Research, 30, 101–116.
- Kamali S, Moranville M, Garboczi E, Prené S, Gérard B, 2003.** Hydrate dissolution influence on the Young's modulus of cement pastes, submitted for publication in "International Conference on Fracture Mechanics of Concrete and Concrete Structures".
- Karihaloo B L, Fu D, 1989.** A damage-based constitutive law for plain concrete in tension, Eur. J. of Mech., Vol 8, (5) 373–384.
- Kersten M, 1996.** Aqueous solubility diagrams for cementitious waste stabilization systems. 1. The CSH solid-solution system, Environ. Sci. Technol. 20, 2286–2293.
- Lagerblad B, Trägårdh J, 1994.** Conceptual model for concrete long time degradation in a deep nuclear waste repository. SKB TR-95-21, Svensk Kärnbränslehantering AB.
- Li Z, Shah S P, 1994.** Localization of microcracking in concrete under uniaxial tension, A CI Mater. J. 372–381.
- Parkhurst D H, Apello C A J, 1999.** User's guide to PHREEQC (Version 2)--a computer program for speciation, batch-reaction, one-dimensional transport, and inverse geochemical calculations: U.S. Geological Survey Water-Resources Investigations Report 99-4259, 312.
- Revertegat E, Adenot F, Richet C, Wu L, Glasser F P, Damidot D, Stronach S A, 1997.** Theoretical and experimental study of degradation mechanisms of cement in repository environment, Report EUR 17942 EN.
- Richardson I G, 1999.** The nature of CSH in hardened cements, Cement and Concrete Research, 29, 1131–1147.
- Rimstidt J D, Barnes H L, 1980.** The kinetics of silica-water reactions, Geochim.Cosmochim. Acta, 44, 1683–1699.
- Samson E, Lemaire G, Marchand J, Beaudoin J J, 1999.** Modelling chemical activity effects in strong ionic solutions, Comput. Mater, Sci. 15 (3) 285–294.
- Samson E, Marchand J, Maltais Y, 2001.** Modelling Diffusion Mechanisms in Saturated Cement-Based Materials-An Overview. In: Ion and mass transport in cement-based materials, 97–112, Materials Science of Concrete, Special volume. The American Ceramic Society, United States of America.
- SKB, 2006.** Climate and climate-related issues for the safety assessment SR-Can. TR-06-23, Svensk Kärnbränslehantering AB.

Suzuki S, Sato H, Ishidera T, Fujii N, 2004. Study on anisotropy of effective diffusion coefficient and activation energy for deuterated water in compacted sodium bentonite, *J. Contam. Hydrol* Vol 68, 23–37.

Taylor H F W, 1990. *Cement chemistry*. Academic Press, London.

Tixier R, 2000. Microstructural development and sulphate attack modelling in blended cement-based materials, PhD dissertation, Arizona State University, Tempe, Ariz.

van Eijk R J, Brouwers H J H, 1998. Study of the relation between hydrated Portland cement and leaching resistance, *Cement and Concrete Research*, Vol. 28, No 6, 815–828.






























Vidstrand P, Svensson U, Follin S, 2006. Simulation of hydrodynamic effects of salt rejection due to permafrost. Hydrogeological numerical model of density-driven mixing, at a regional scale, due to a high salinity pulse. SKB R-06-101, Svensk Kärnbränslehantering AB.





Weast R C, Astle M J, 1982. *CRC handbook of chemistry and physics*, ISBN-0-8493-0462-8.

ZZ-HATCHES-17, 2006. NEA-1210/18.

Appendix A

Table A-1. A selection of minerals initially present or likely to precipitate in cement and/or clay, their $\log k$ value, molar volume and colour code employed in figures in Appendix B.

Mineral	Formula	$\log k$	Molar volume (cm ³)	Ref. $\log k$	Ref. vol.	Colour code
Brucite	Mg(OH) ₂	16.85	24.63	a	b	
Calcite	CaCO ₃	-8.47	36.93	a	b	
CSH _{1,8}	C _{1,8} S _{3,8} H	32.4	108.0	a	c	
CSH _{1,1}	C _{1,1} S _{3,1} H	16.66	101.8	a	c	
CSH _{0,8}	C _{0,8} S _{2,8} H	11.03	101.8	a	c*	
Ettringite	Ca ₆ Al ₂ (SO ₄) ₃ (OH) ₁₂ ·26H ₂ O	57.0	735.0	a	c	
Friedelsalt	Ca ₄ Al ₂ Cl ₂ O ₁₆ H ₂ O	70.72	296.66	a	c	
Hydrogarnet	Ca ₃ Al ₂ O ₆ ·6H ₂ O	80.8	150.0	a	c	
Hydrotalcite	Mg ₄ Al ₂ O ₁₇ H ₂ O	75.34	301.51	a	d	
Hydroxyapatite	Ca ₅ (PO ₄) ₃ OH	-3.07	159.2	a	e	
Monocarboaluminate	Ca ₄ Al ₂ (CO ₃)O ₁₇ H ₂₂	68.93	191.68	a	c	
Monosulphate	Ca ₄ Al ₂ (SO ₄)O ₁₈ H ₂₄	70.25	313.0	a	c	
Portlandite	Ca(OH) ₂	22.81	33.1	a	c	
Clinoptil-K	KAlSi ₅ O ₁₂ ·4H ₂ O	-7.42	633.1	a	e	
Illite	K _{0,6} Mg _{0,25} Al _{1,8} Al _{0,5} Si _{3,5} O ₁₁ ·H ₂ O	9.8	138.94	a	e	
Katoite	Ca ₃ Al ₂ SiO ₁₂ H ₈	68.89	149.52	a	e	
Magnetite	Fe ₃ O ₄	10.13	44.52	a	e	
Montmorillonite-Ca	Ca _{0,165} Mg _{0,33} Al _{1,67} Si ₄ O ₁₀ (OH) ₂	3.06	220.0	a	e*	
Montmorillonite-K	K _{0,33} Mg _{0,33} Al _{1,67} Si ₄ O ₁₀ (OH) ₂	2.72	220.0	a	e*	
Montmorillonite-Mg	Mg _{0,495} Al _{1,67} Si ₄ O ₁₀ (OH) ₂	2.98	220.0	a	e*	
Montmorillonite-Na	Na _{0,33} Mg _{0,33} Al _{1,67} Si ₄ O ₁₀ (OH) ₂	3.06	220.0	a	e	
Mordenite-Na	NaAlSi ₅ O ₁₂ ·3H ₂ O	-4.53	209.9	a	e	
Phillipsite-K	K ₂ Al ₂ Si ₅ O ₁₄ ·5H ₂ O	3.4	609.0	a	e	
Phillipsite-Na	Na ₂ Al ₂ Si ₅ O ₁₄ ·5H ₂ O	10.92	609.0	a	e	
Saponite-Ca	Ca _{0,165} Mg ₃ Al _{0,33} Si _{3,67} O ₁₀ (OH) ₂	26.82	135.68	a	e	
Saponite-H	H _{0,33} Mg ₃ Al _{0,33} Si _{3,67} O ₁₀ (OH) ₂	25.85	135.68	a	e*	
Saponite-K	K _{0,33} Mg ₃ Al _{0,33} Si _{3,67} O ₁₀ (OH) ₂	26.55	135.68	a	e*	
Saponite-Mg	Mg _{3,165} Al _{0,33} Si _{3,67} O ₁₀ (OH) ₂	26.8	135.68	a	e*	
Saponite-Na	Na _{0,33} Mg ₃ Al _{0,33} Si _{3,67} O ₁₀ (OH) ₂	26.88	136.69	a	e	

Mineral	Formula	log k	Molar volume (cm ³)	Ref. log k	Ref. vol.	Colour code
Albite	NaAlSi ₃ O ₈	4.42	100.25	a	e	
Biotite	KMg ₃ AlSi ₃ O ₁₀ (OH) ₂	4.42	150.0	a	e	
K-feldspar	KAlSi ₃ O ₈	0.08	108.87	a	e	
Quartz	SiO ₂	-4.0	22.93	a	e	

From a) /ZZ-HATCHES-17 2006/, b) CRC handbook of Chemistry and physics, c) molar volumes employed by CEMHYD3D /Bentz 2000/ based on /Fukuhara et al. 1981/, d) based on density 2.06 g/cm³ given by <http://www.mineralienatlas.de/>, e) /Gaucher et al. 2005/.

*assumed to have the same molar volume as the mineral phase without asterisk in the same family, i.e. CSH_{0.8} is assumed to have the same molar volume as CSH_{1.1}, Montmorillonite-Ca, K, Mg as Montmorillonite-Na, Saponite-H,K,Mg as Saponite-Ca.

Appendix B

Appendix B contains the results of calculations on the Silo and BMA for each of the seven type of scenarios (see Table B-1) visualized in terms of cross-sections at year 1,000, 10,000, 50,000 and 100,000.

Table B-1. A summary of performed calculations on BMA and the Silo.

Scenario	Selection of parameters
A	Fixed diffusivity, fixed temperature and water composition.
B	Fixed diffusivity, variable temperature and fixed composition.
C	Fixed diffusivity, fixed temperature and variable water composition.
D	Dynamic diffusivity, fixed temperature and water composition.
E	Dynamic diffusivity, variable temperature and water composition.
F	Dynamic diffusivity, variable temperature and water composition and fracture mechanics as described in Section 2.2.
G	Scaled diffusivity according to predicted freeze-thaw cycles, variable temperature and water composition as described in Section 2.3.

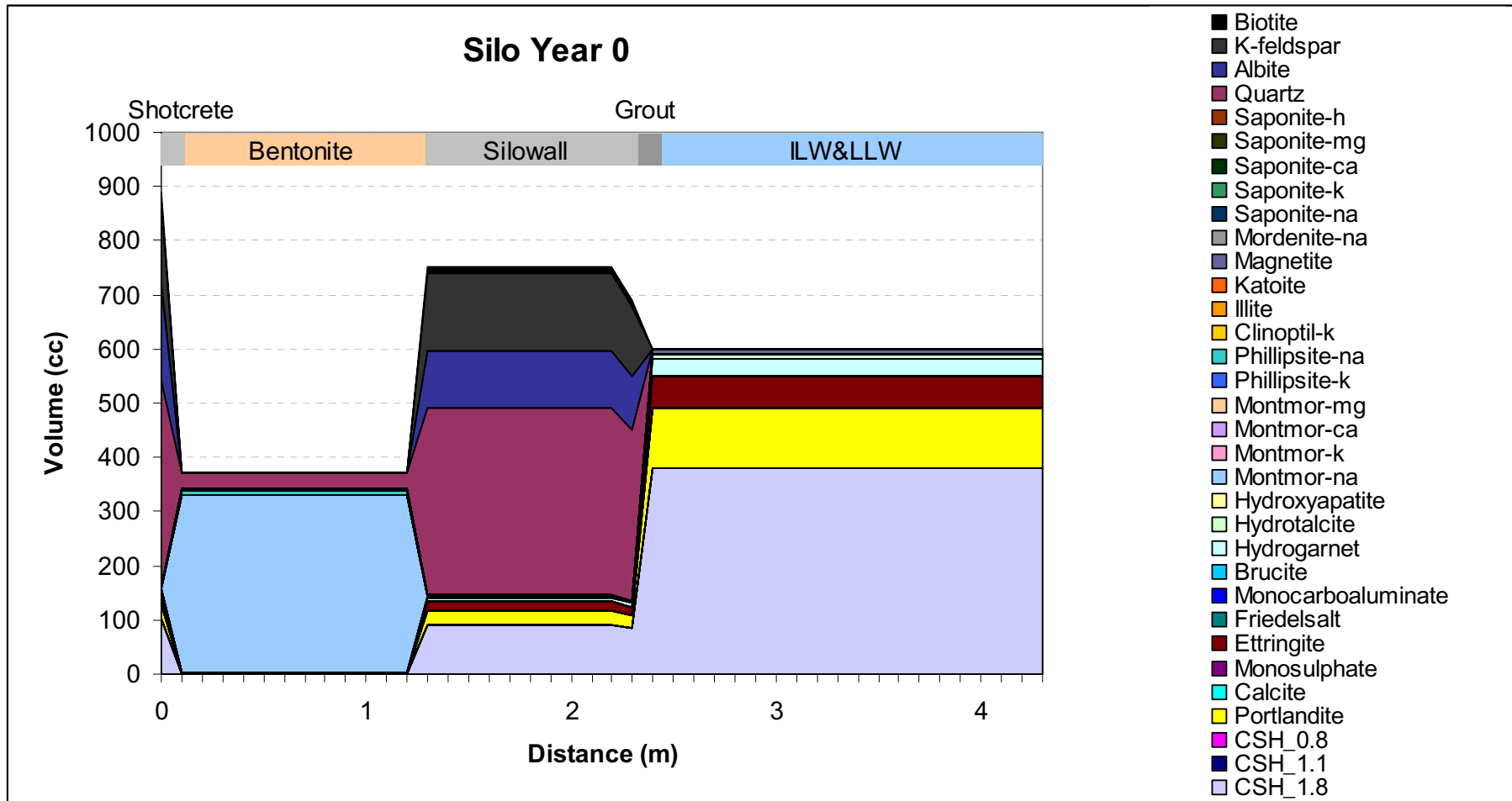


Figure B-1. Initial mineral distribution in the Silo.

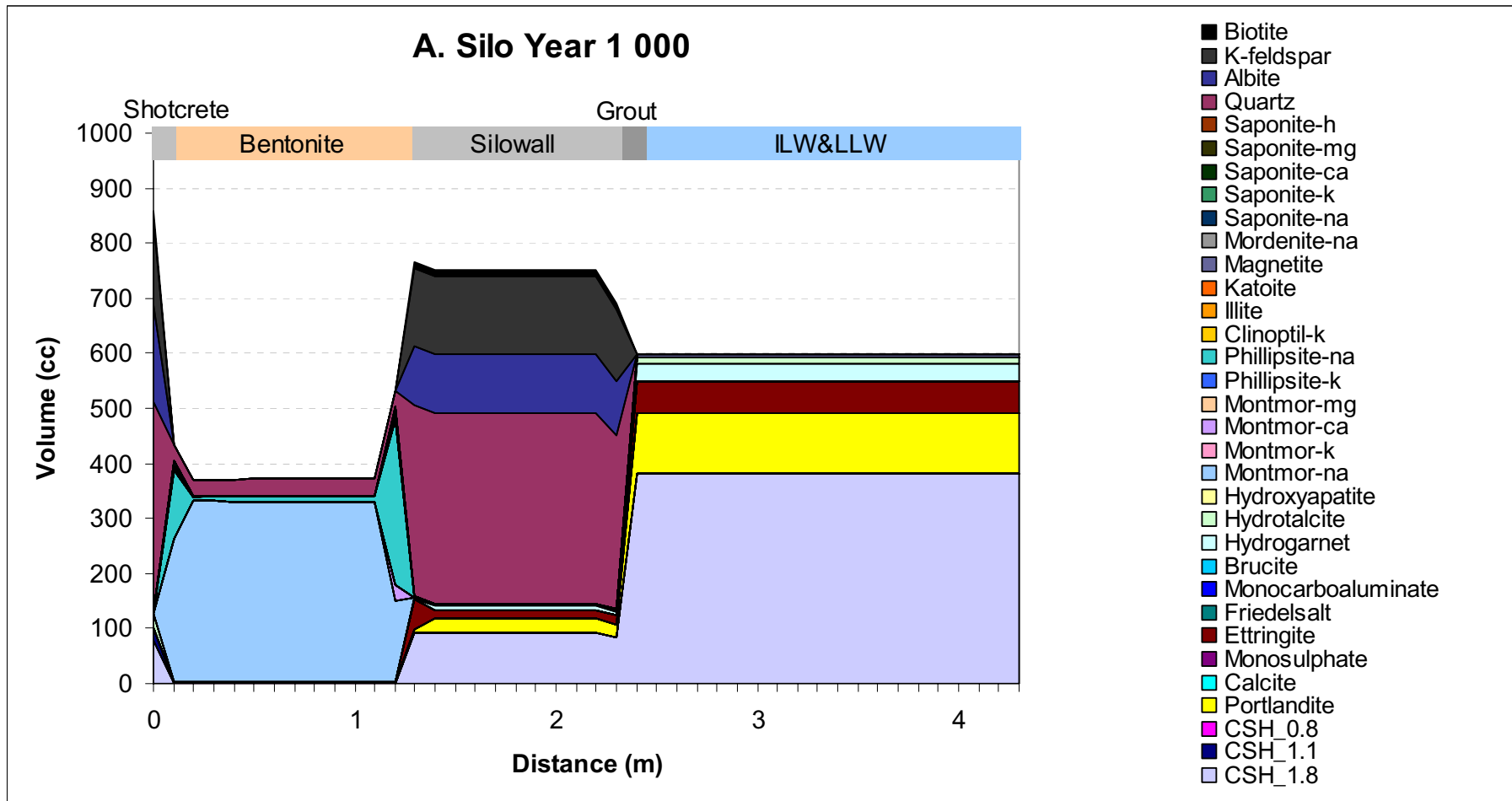


Figure B-2. Mineral distribution in the Silo at year 1,000 (fixed diffusivity, temperature and water composition).

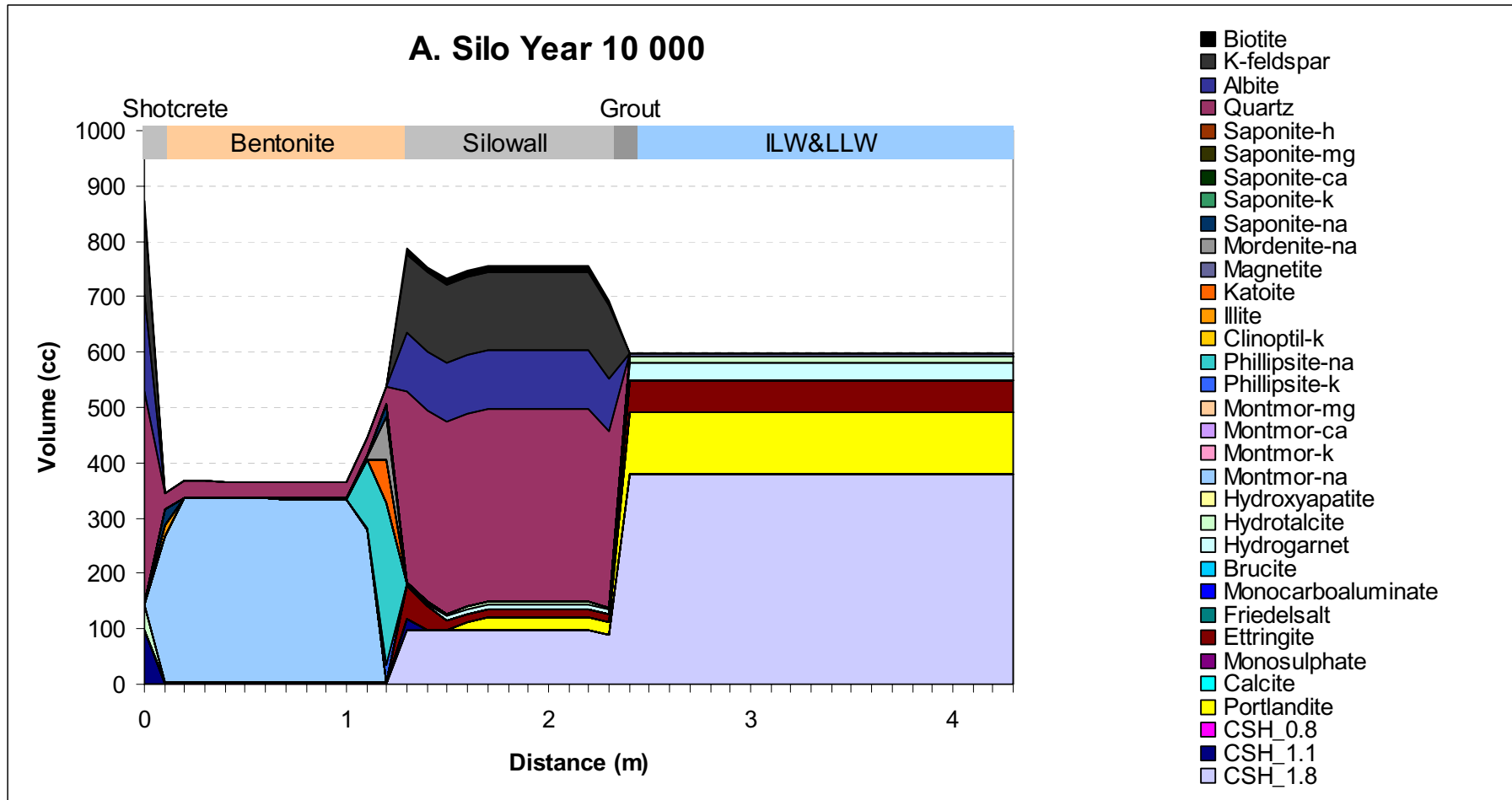


Figure B-3. Mineral distribution in the Silo at year 10,000 (fixed diffusivity, temperature and water composition).

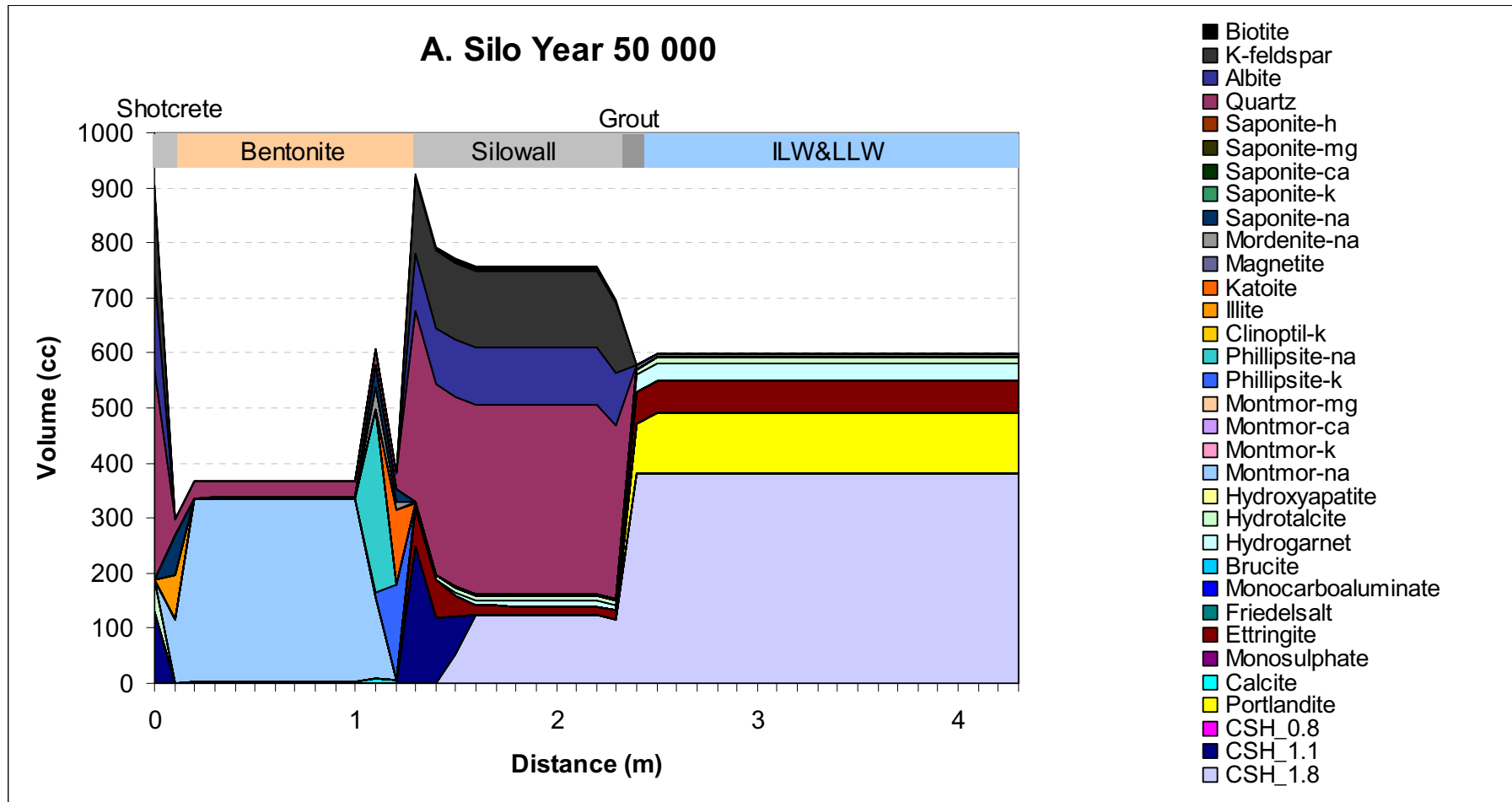


Figure B-4. Mineral distribution in the Silo at year 50,000 (fixed diffusivity, temperature and water composition).

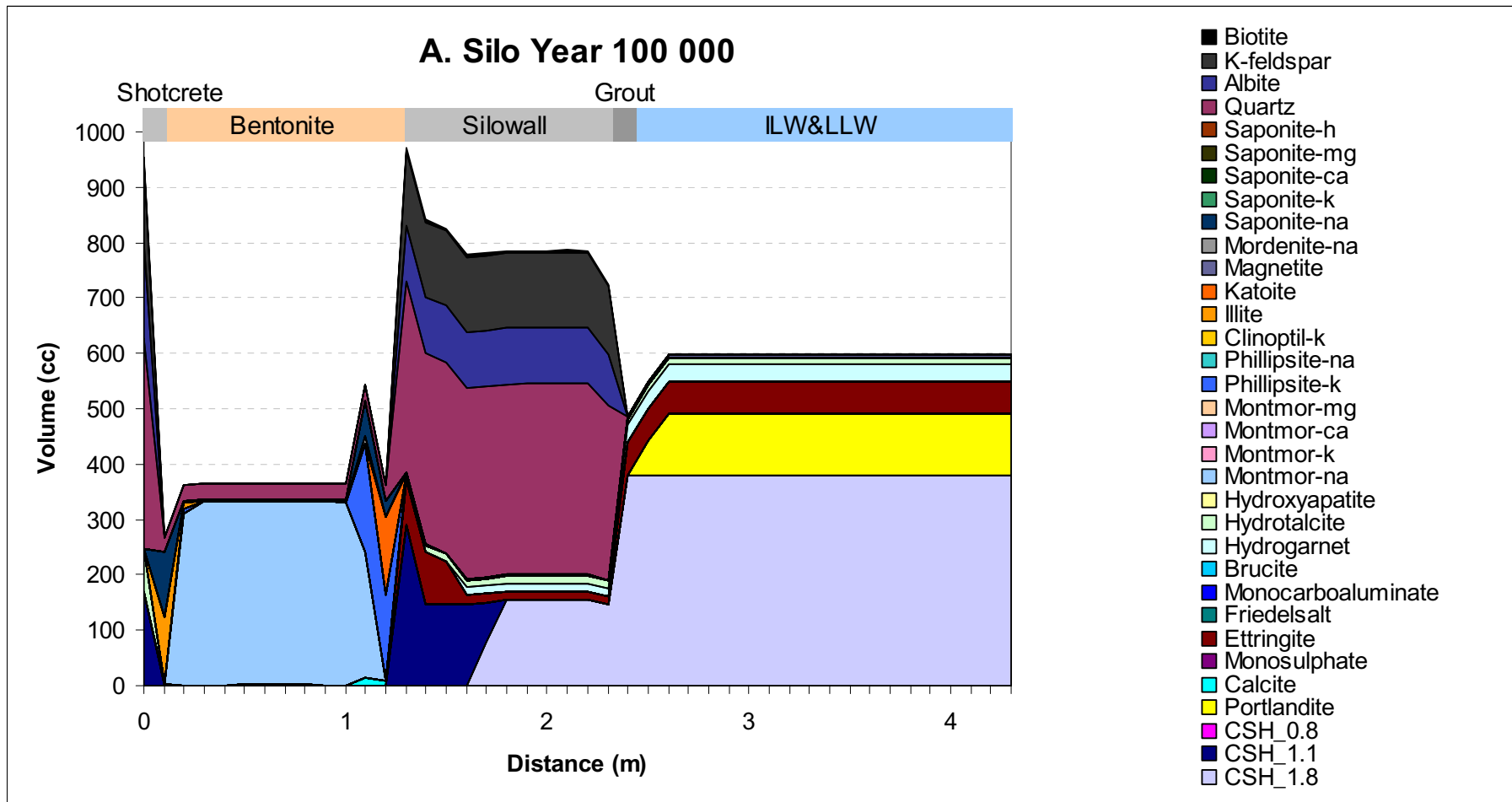


Figure B-5. Mineral distribution in the Silo at year 100,000 (fixed diffusivity, temperature and water composition).

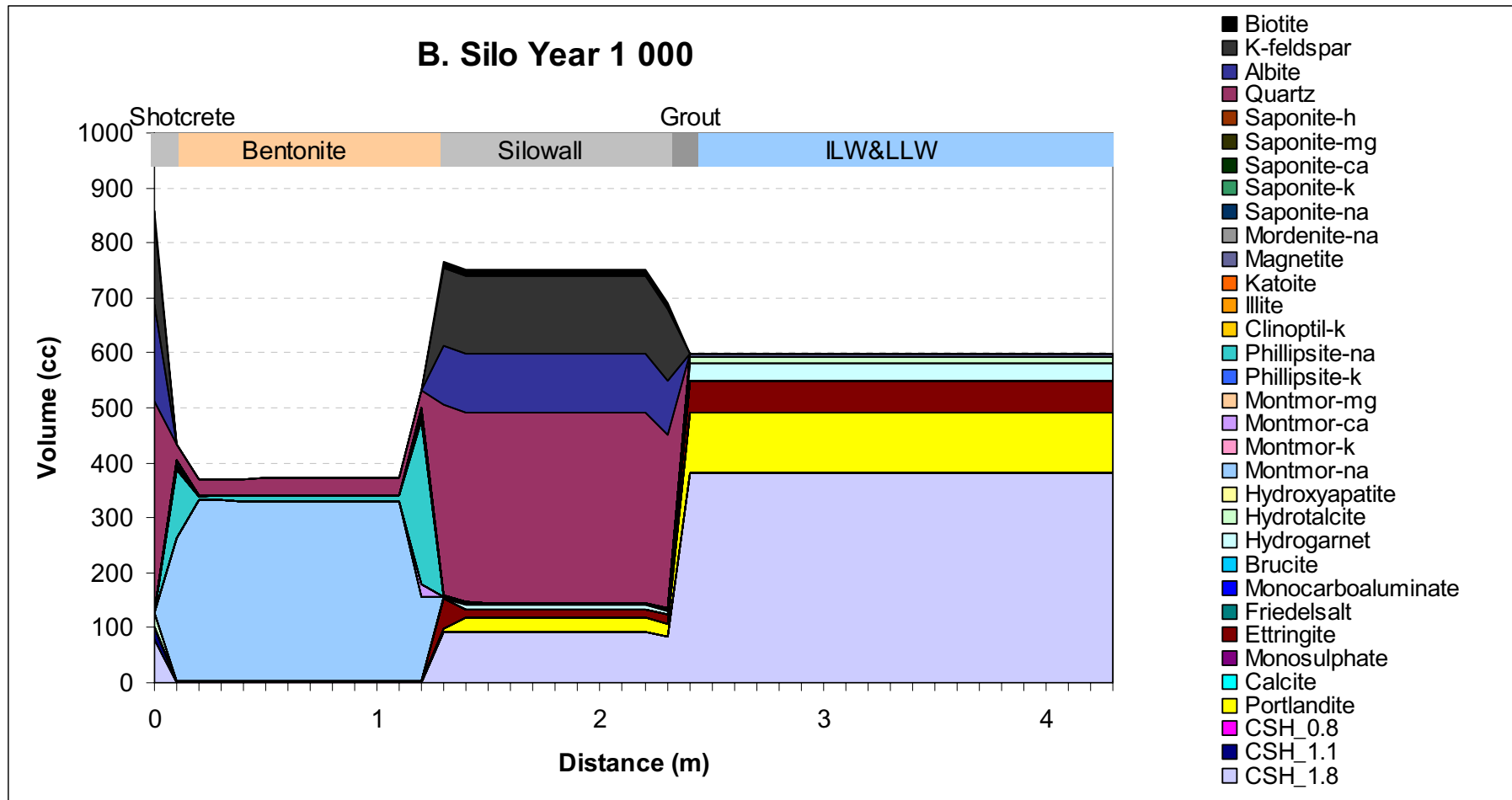


Figure B-6. Mineral distribution in the Silo at year 1,000 (fixed diffusivity and water composition, variable temperature).

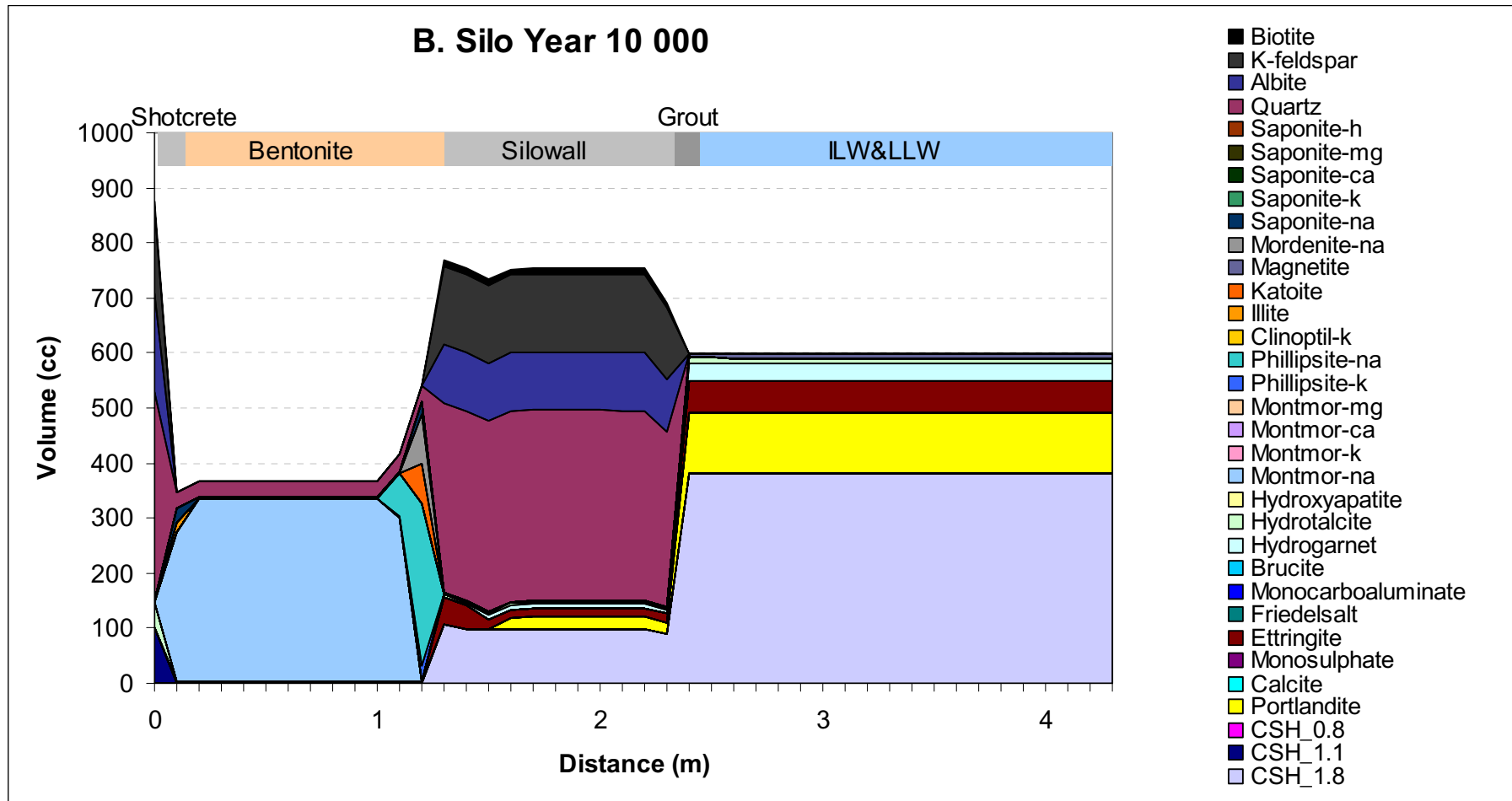


Figure B-7. Mineral distribution in the Silo at year 10,000 (fixed diffusivity and water composition, variable temperature).

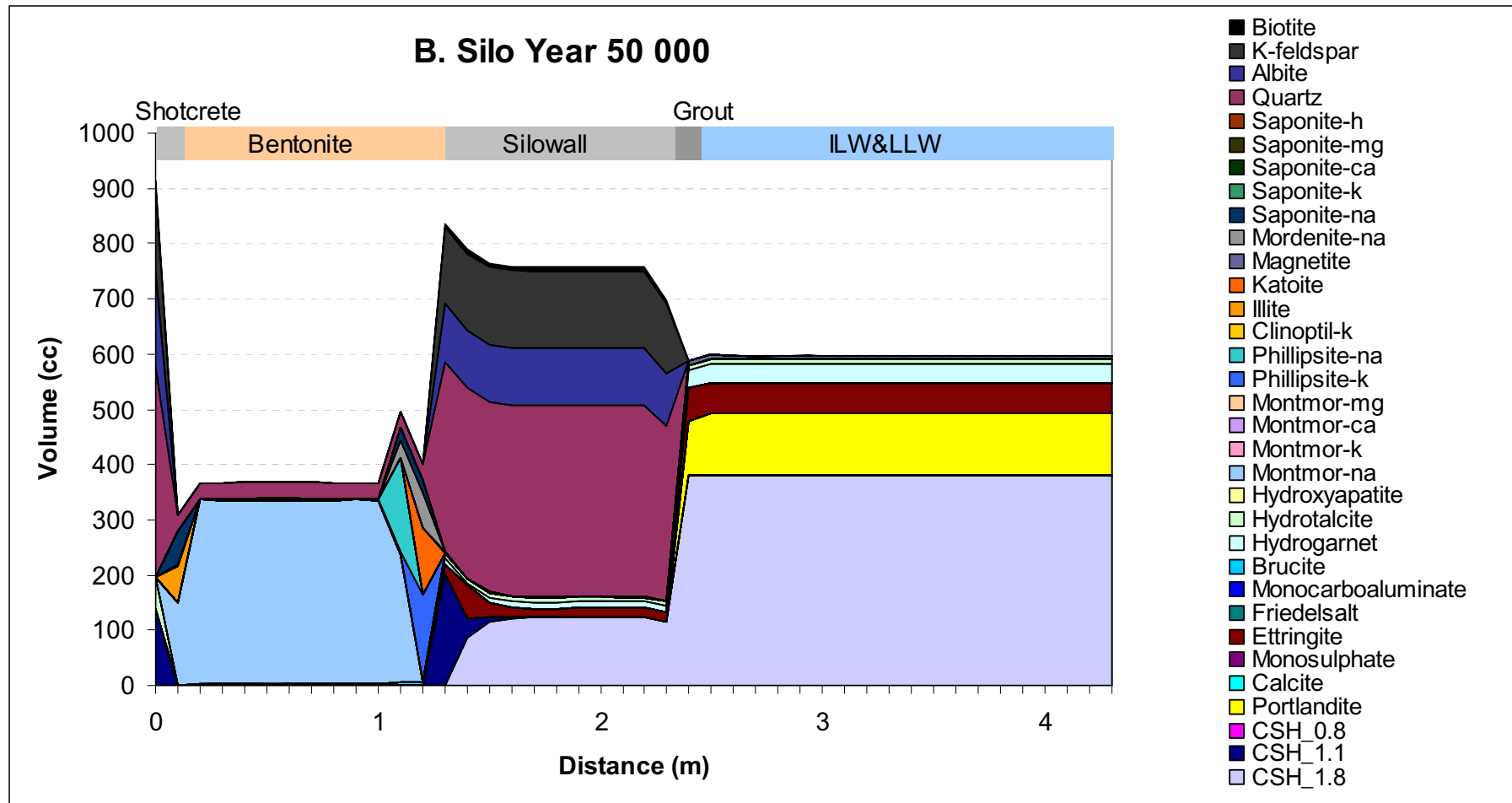


Figure B-8. Mineral distribution in the Silo at year 50,000 (fixed diffusivity and water composition, variable temperature).

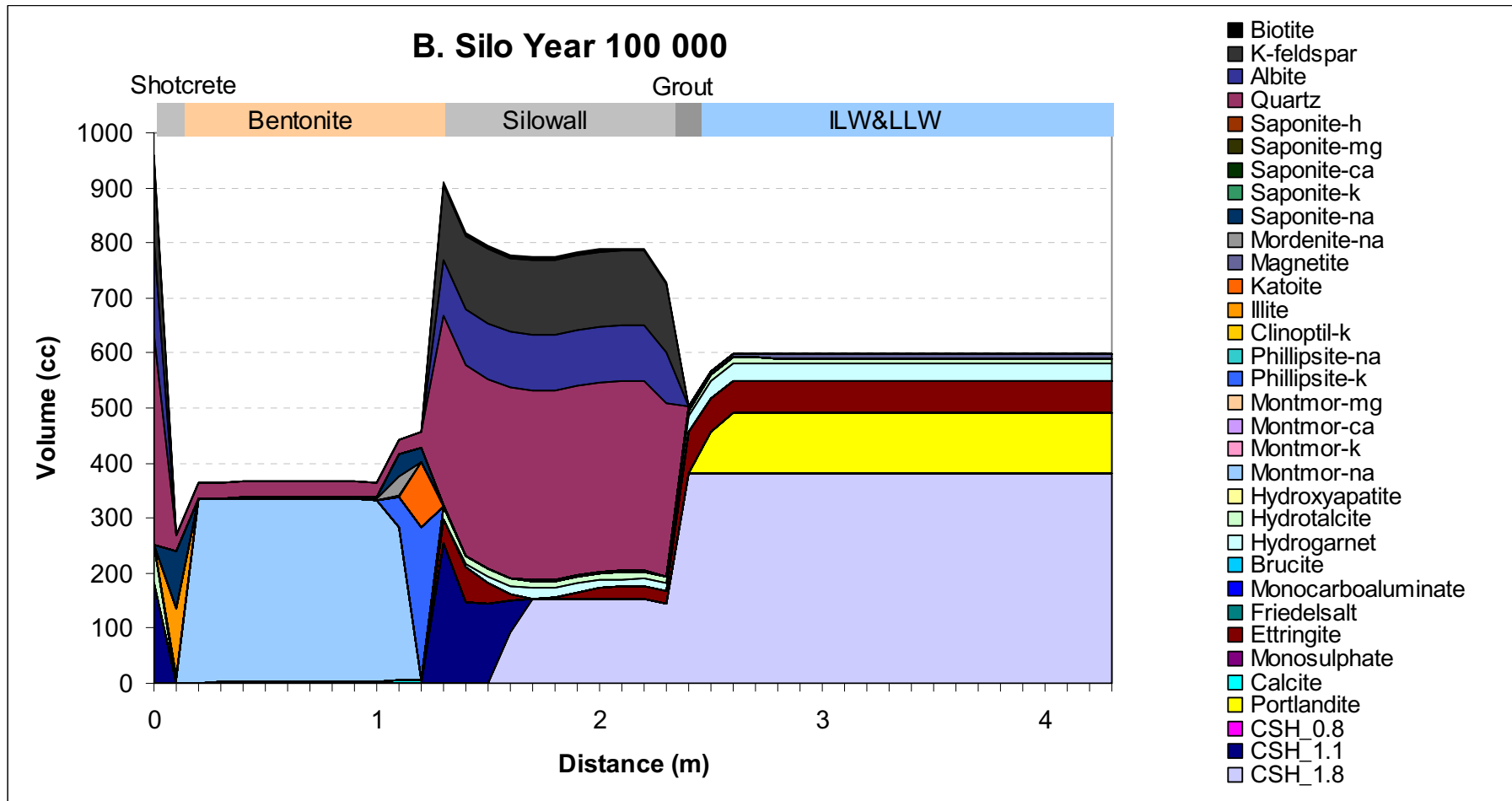


Figure B-9. Mineral distribution in the Silo at year 100,000 (fixed diffusivity and water composition, variable temperature).

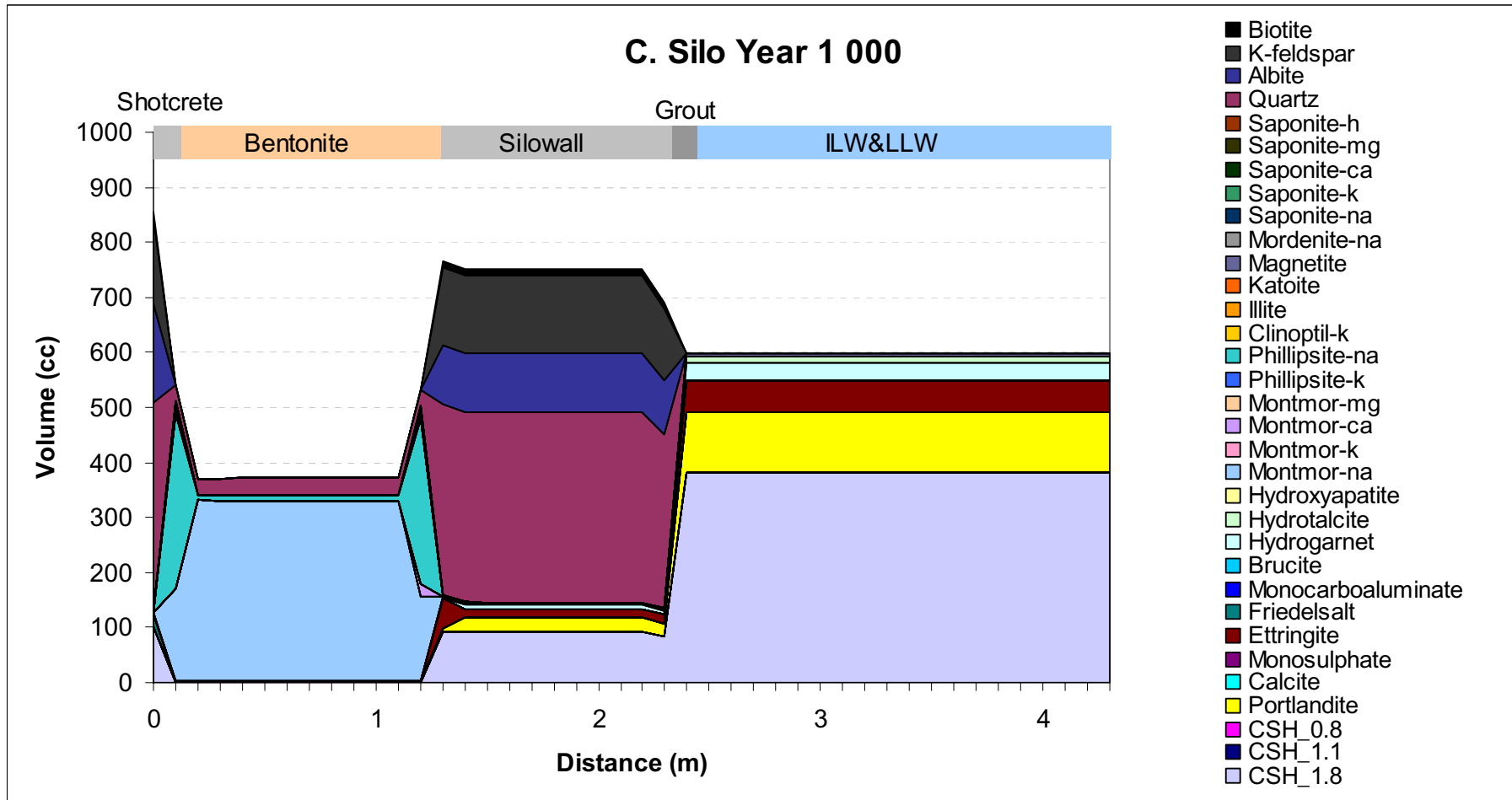


Figure B-10. Mineral distribution in the Silo at year 1,000 (fixed diffusivity and temperature, variable water composition).

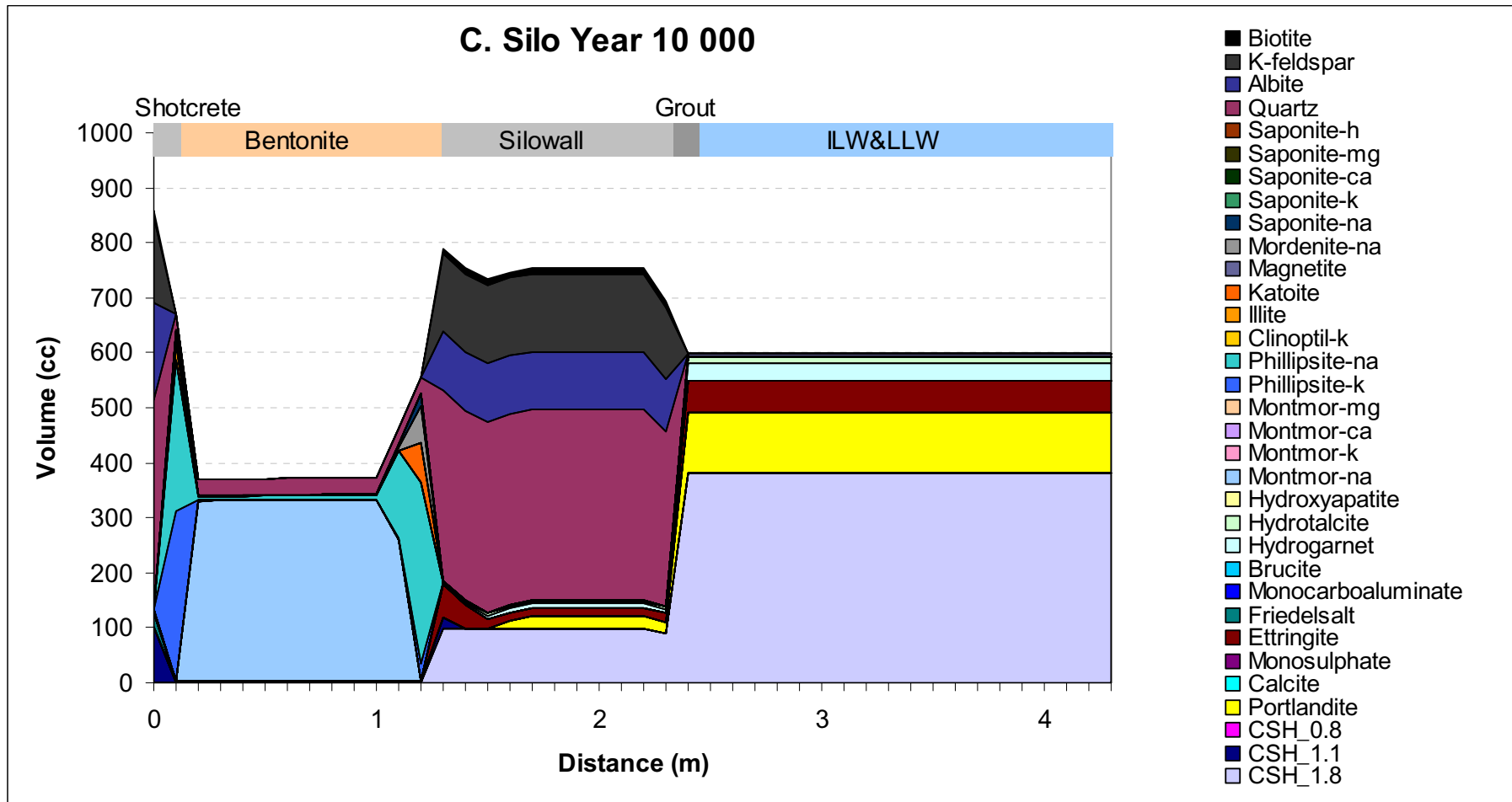


Figure B-11. Mineral distribution in the Silo at year 10,000 (fixed diffusivity and temperature, variable water composition).

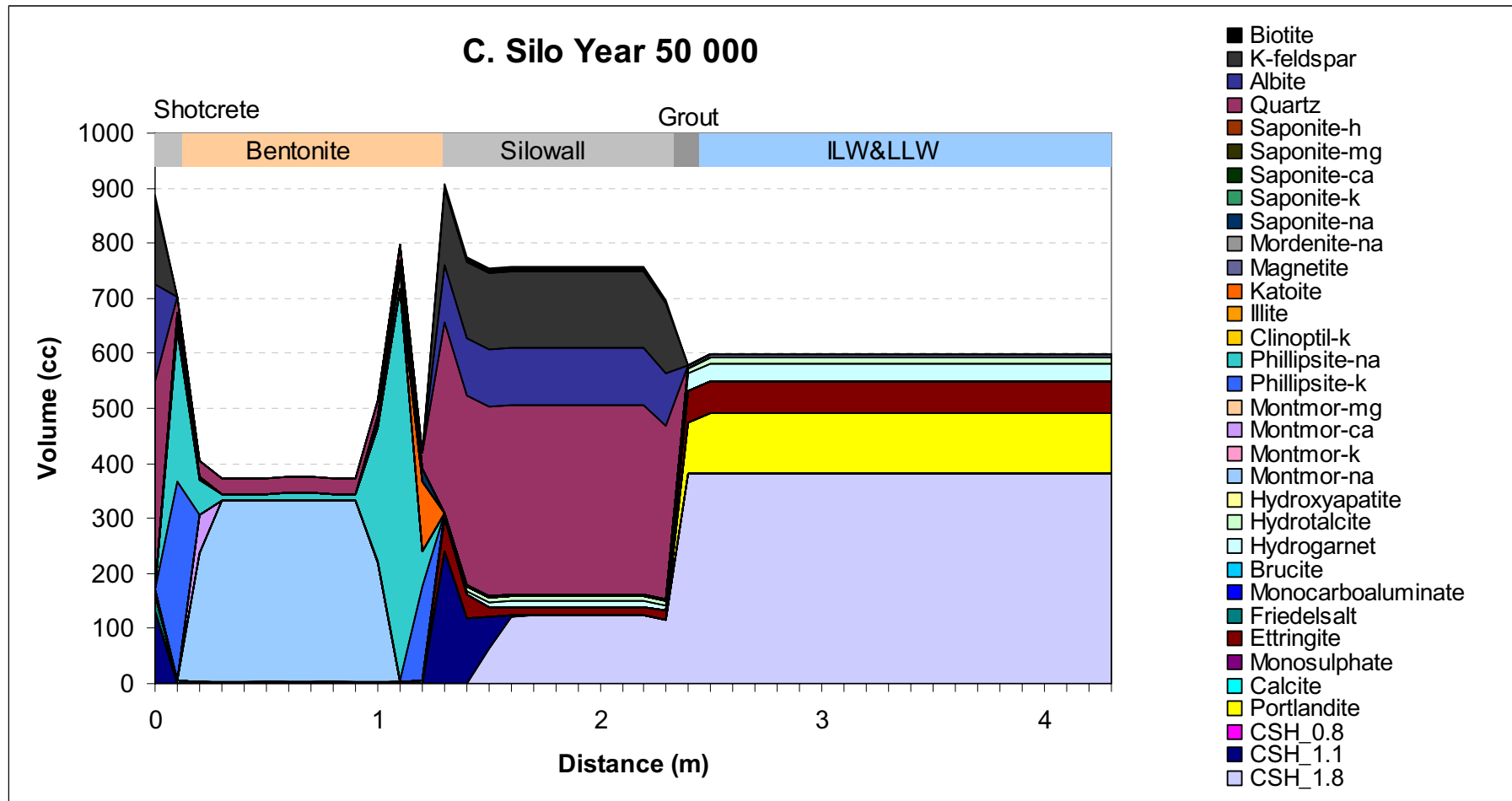


Figure B-12. Mineral distribution in the Silo at year 50,000 (fixed diffusivity and temperature, variable water composition).

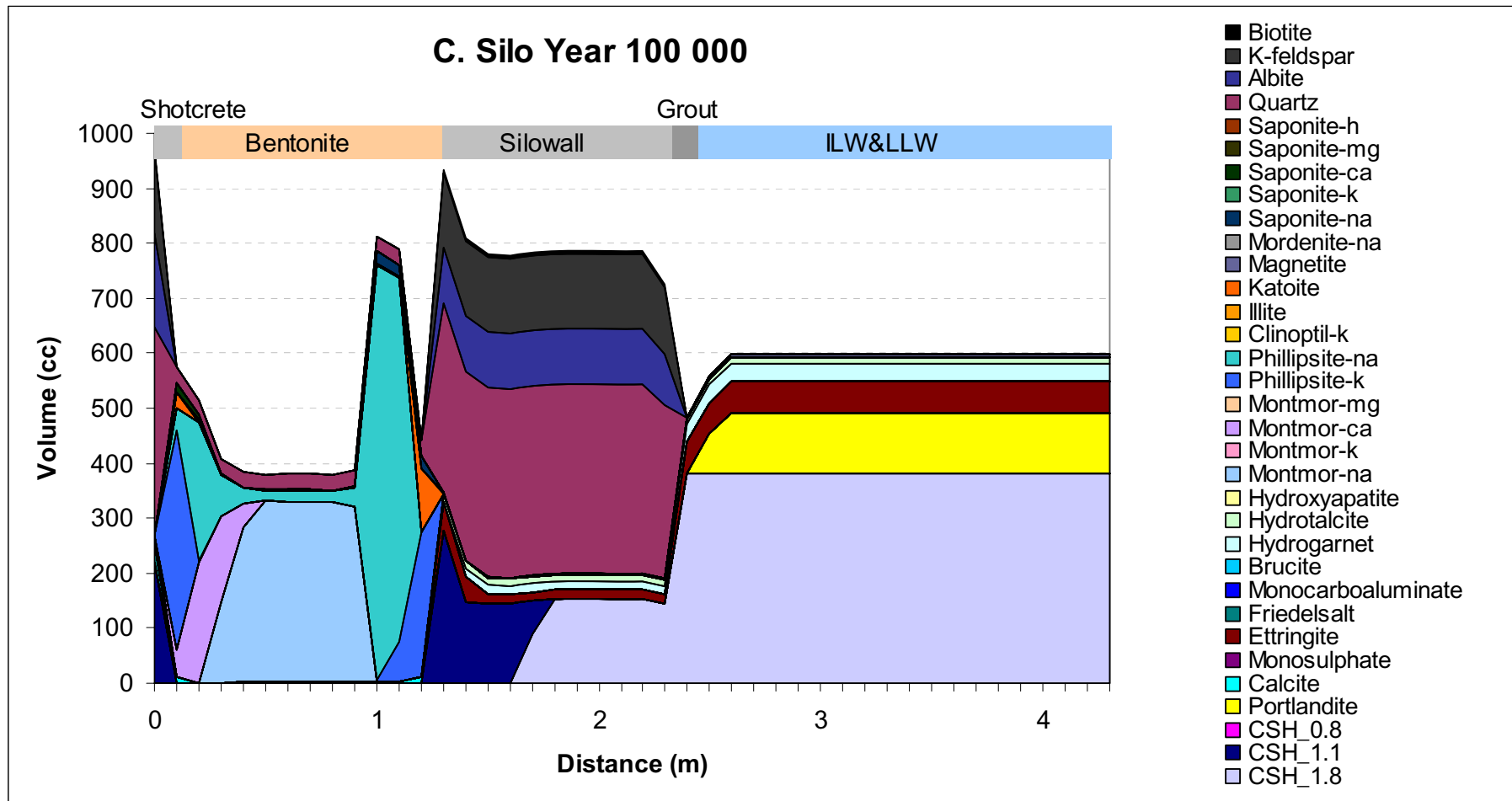


Figure B-13. Mineral distribution in the Silo at year 100,000 (fixed diffusivity and temperature, variable water composition).

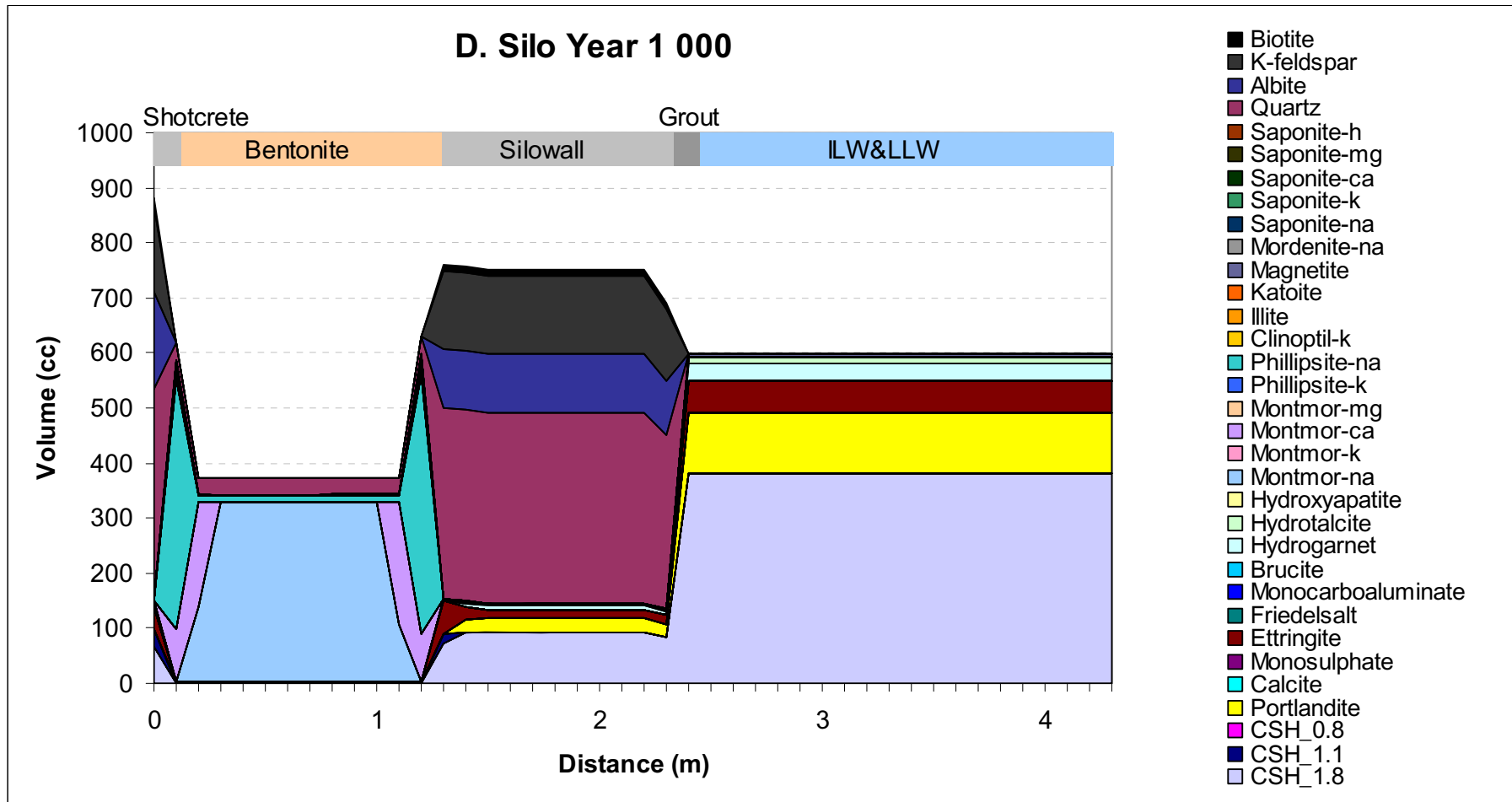


Figure B-14. Mineral distribution in the Silo at year 1,000 (dynamic diffusivity, fixed temperature and water composition).

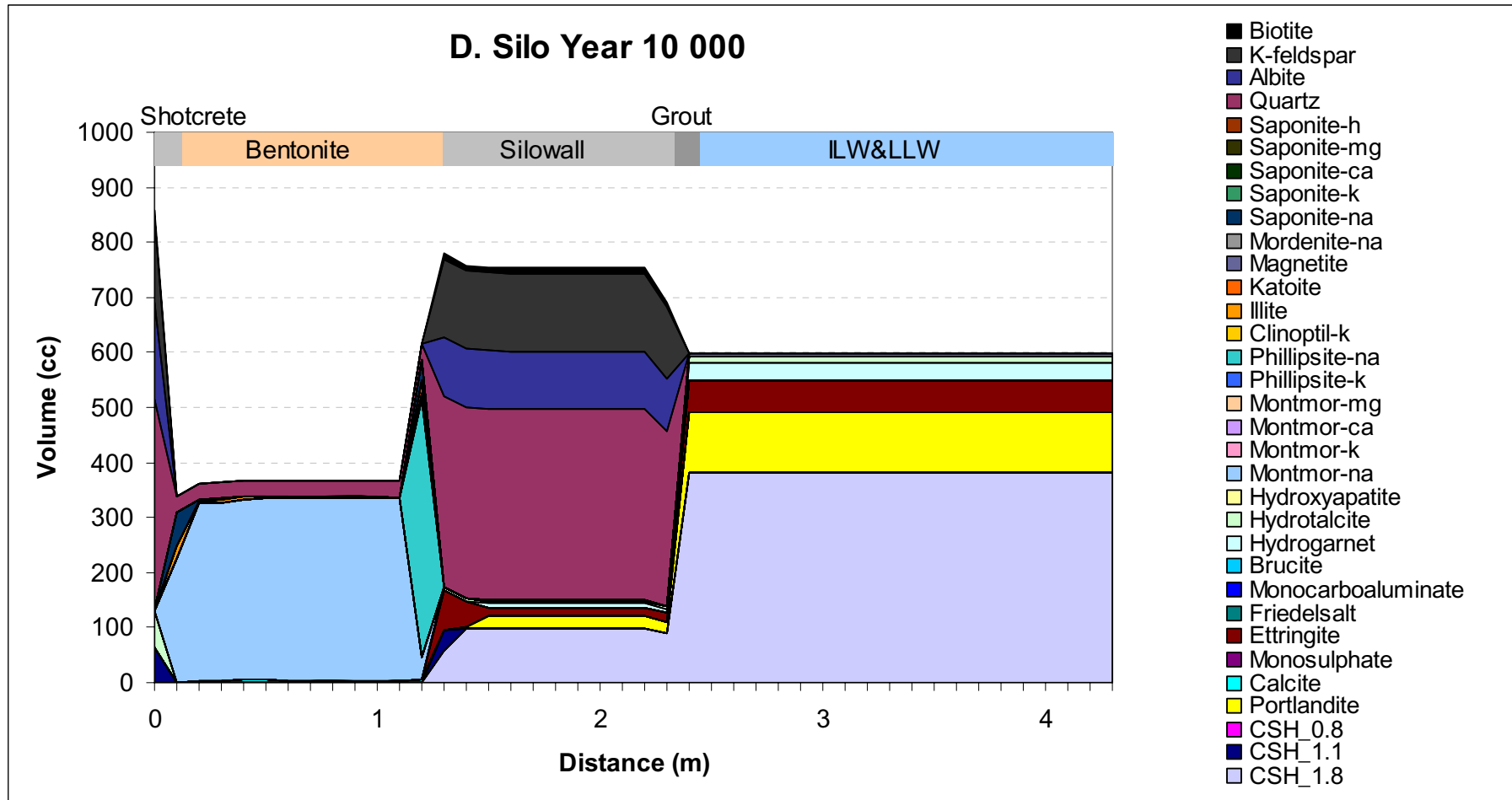


Figure B-15. Mineral distribution in the Silo at year 10,000 (dynamic diffusivity, fixed temperature and water composition).

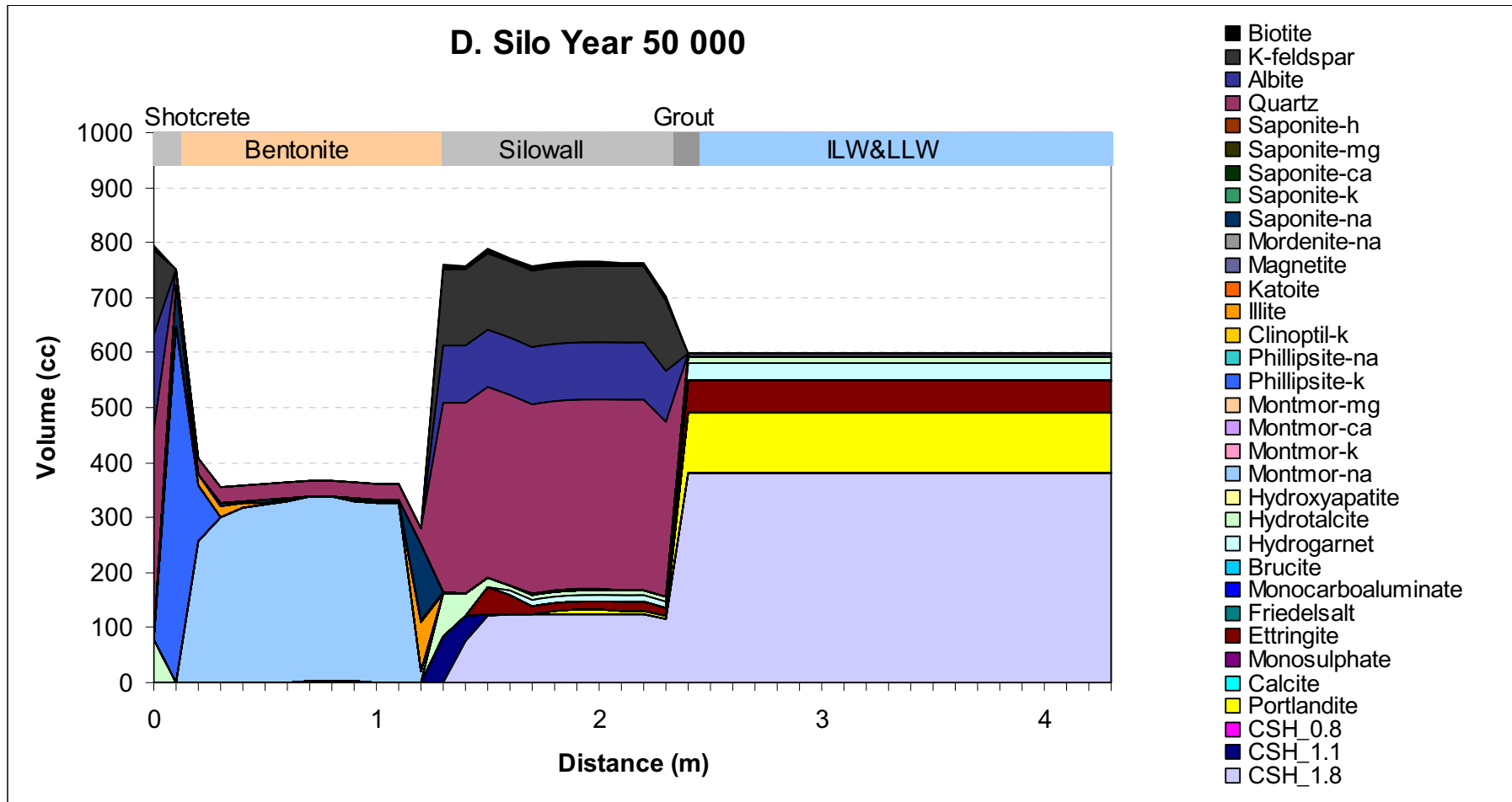


Figure B-16. Mineral distribution in the Silo at year 50,000 (dynamic diffusivity, fixed temperature and water composition).

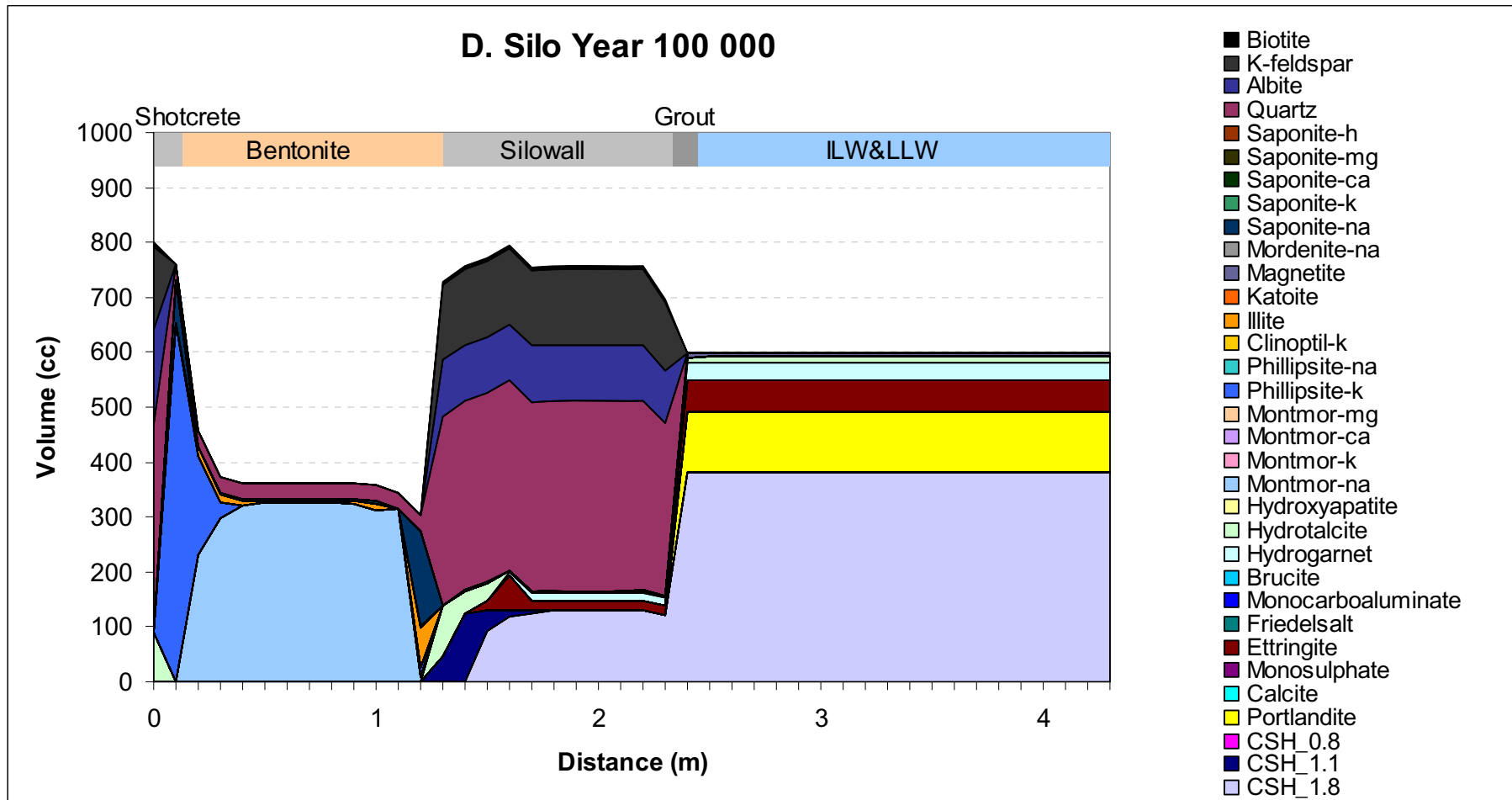


Figure B-17. Mineral distribution in the Silo at year 100,000 (dynamic diffusivity, fixed temperature and water composition).

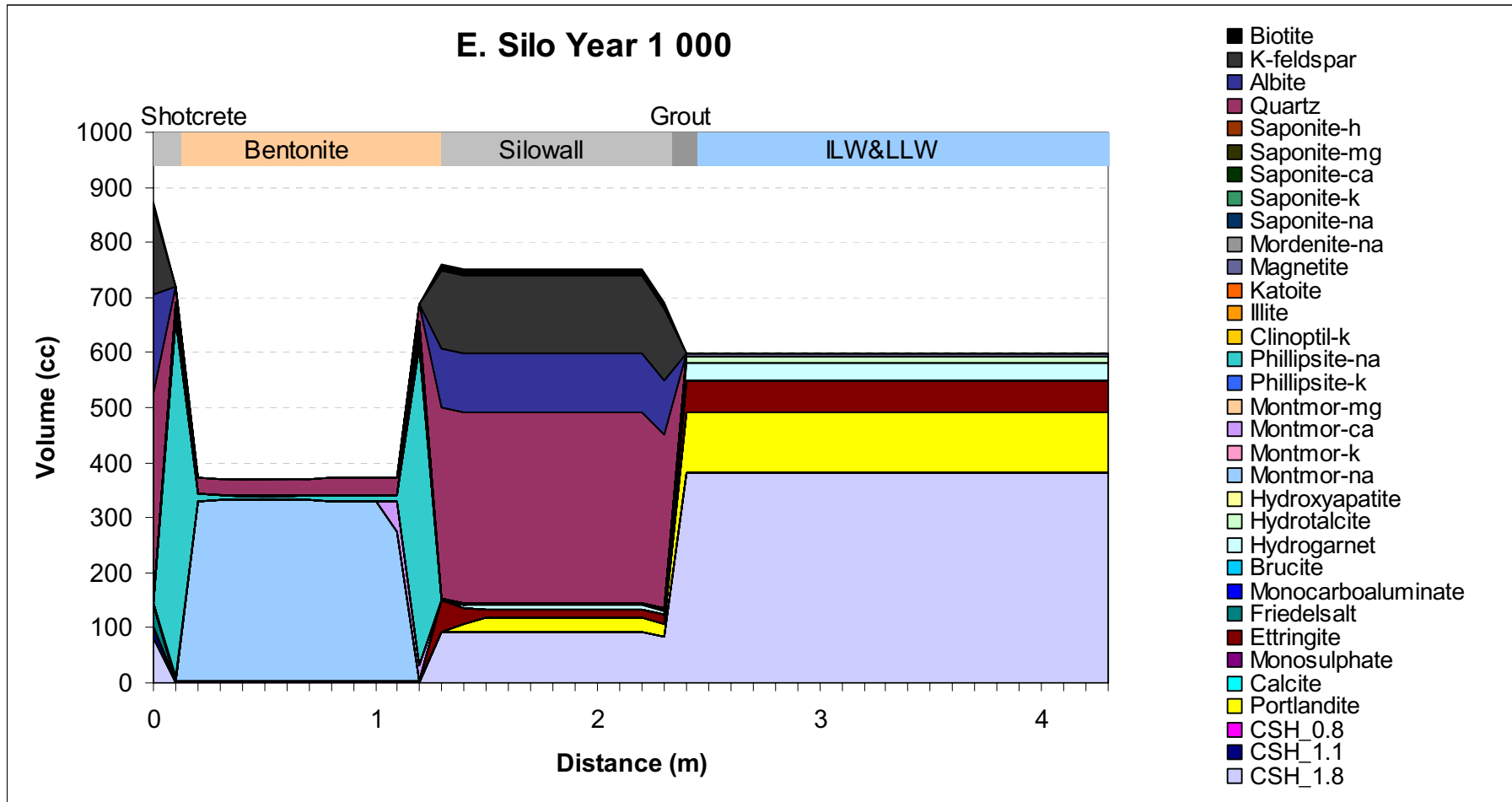


Figure B-18. Mineral distribution in the Silo at year 1,000 (dynamic diffusivity, variable temperature and water composition).

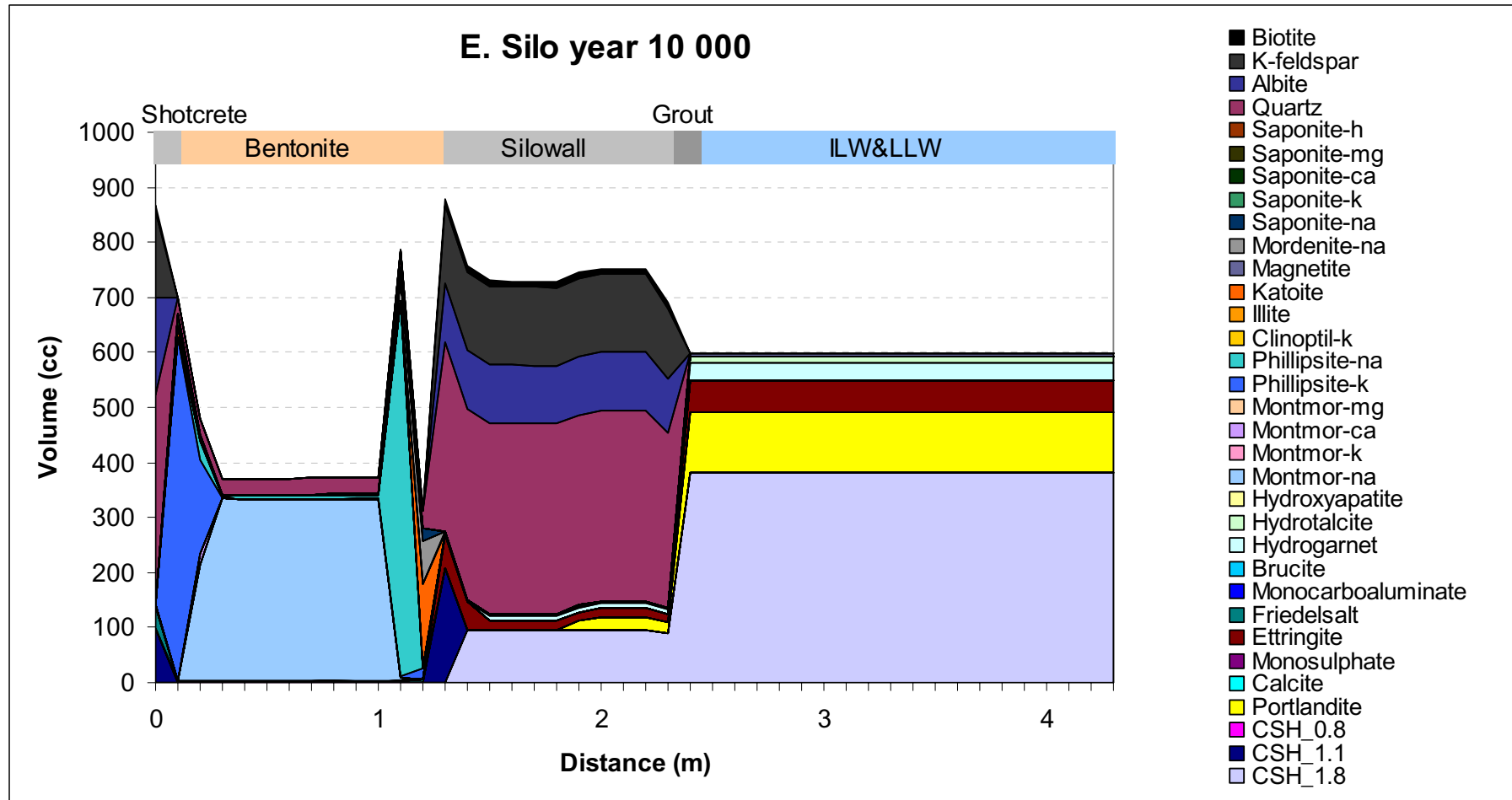


Figure B-19. Mineral distribution in the Silo at year 10,000 (dynamic diffusivity, variable temperature and water composition).

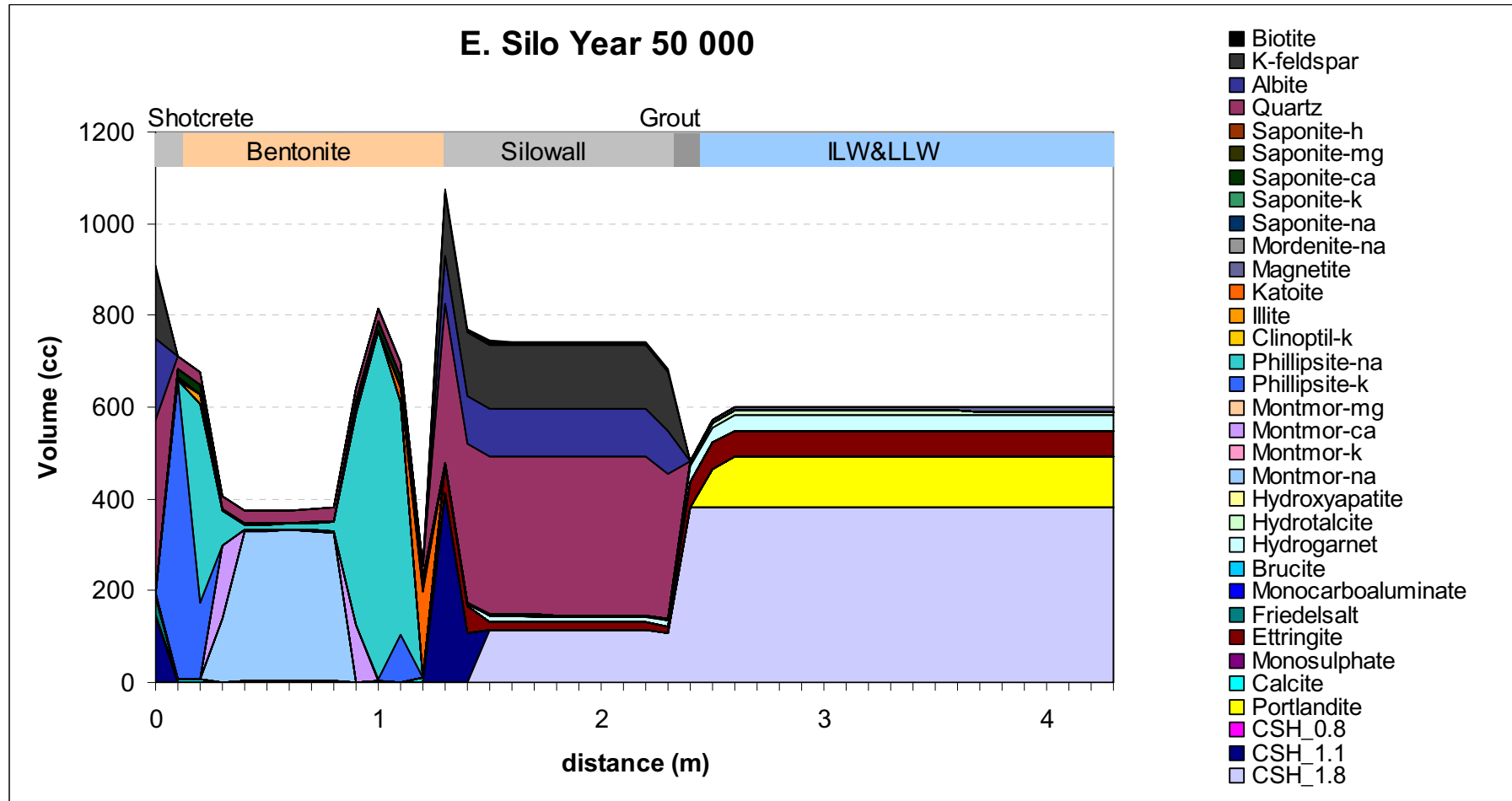


Figure B-20. Mineral distribution in the Silo at year 50,000 (dynamic diffusivity, variable temperature and water composition).

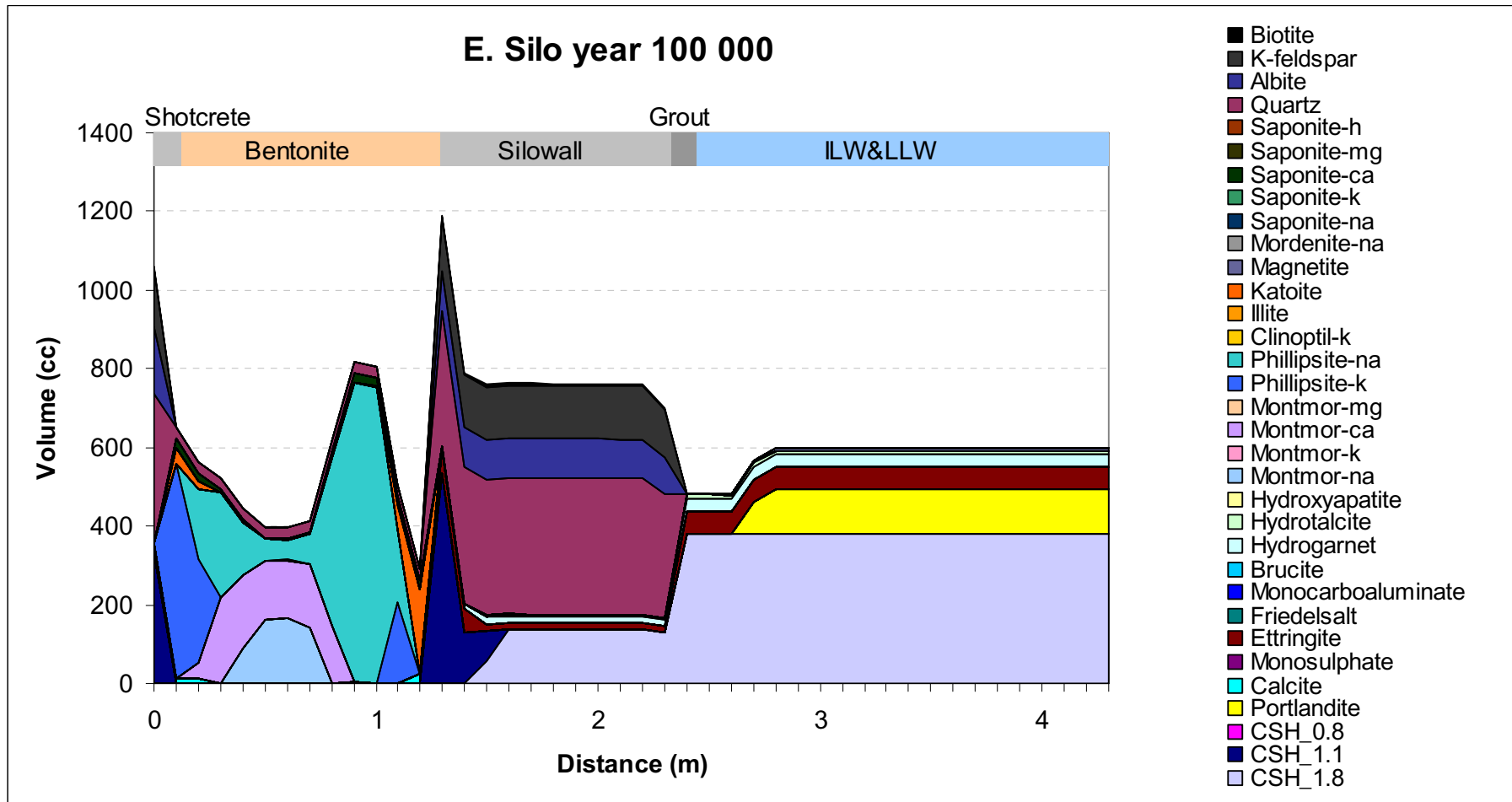


Figure B-21. Mineral distribution in the Silo at year 100,000 (dynamic diffusivity, variable temperature and water composition).

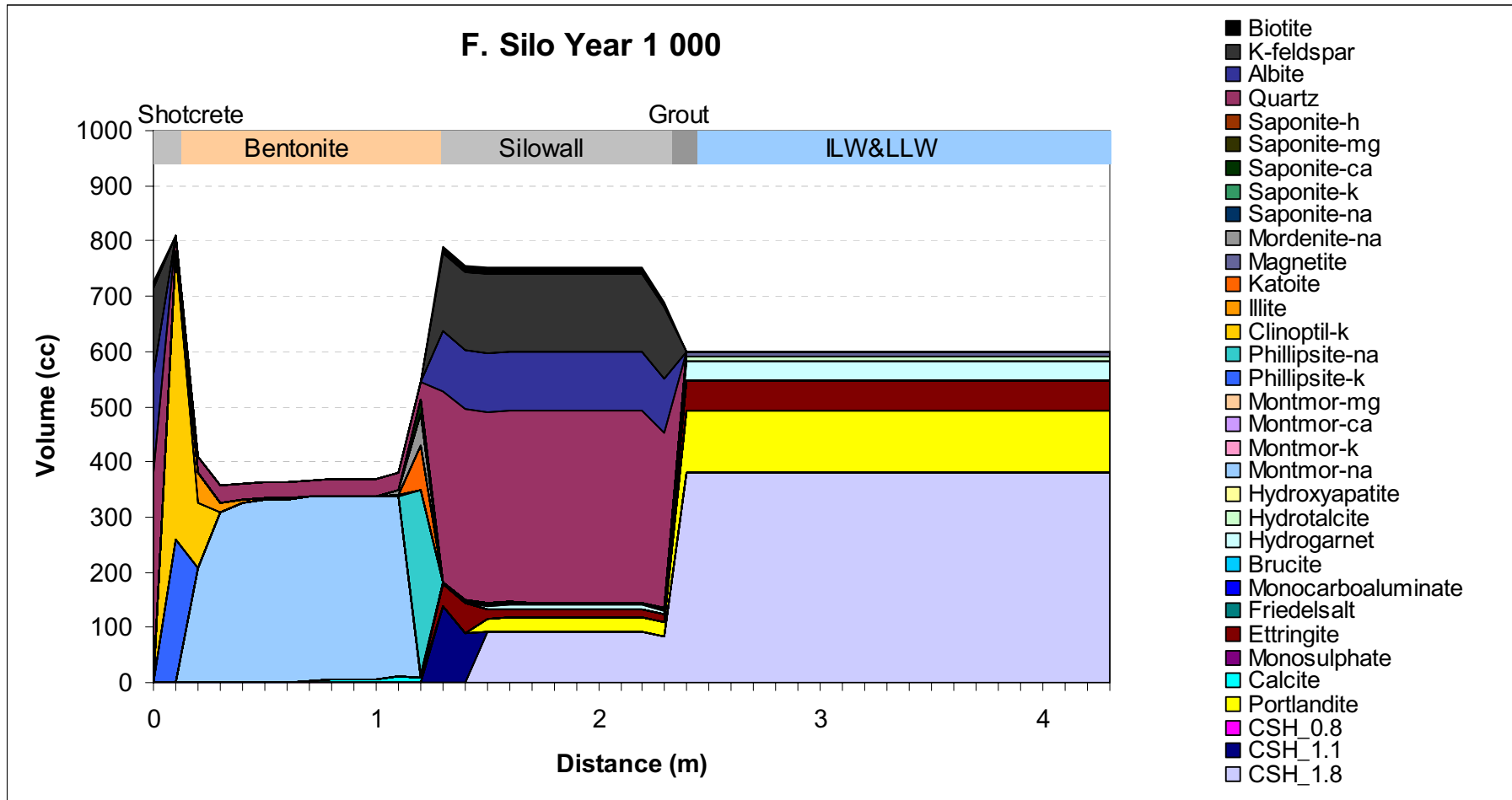


Figure B-22. Mineral distribution in the Silo at year 1,000 (fracture model).

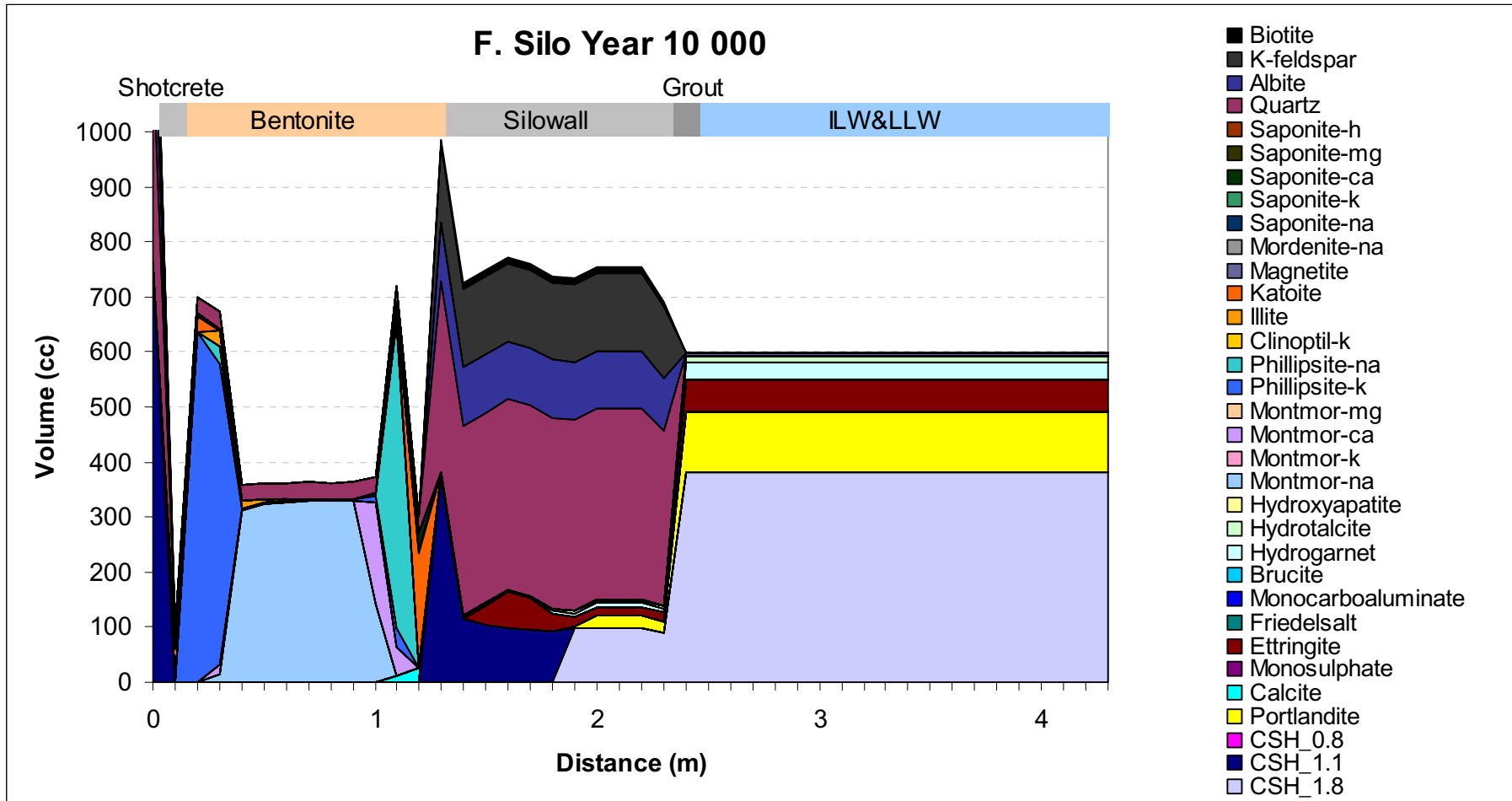


Figure B-23. Mineral distribution in the Silo at year 10,000 (fracture model).

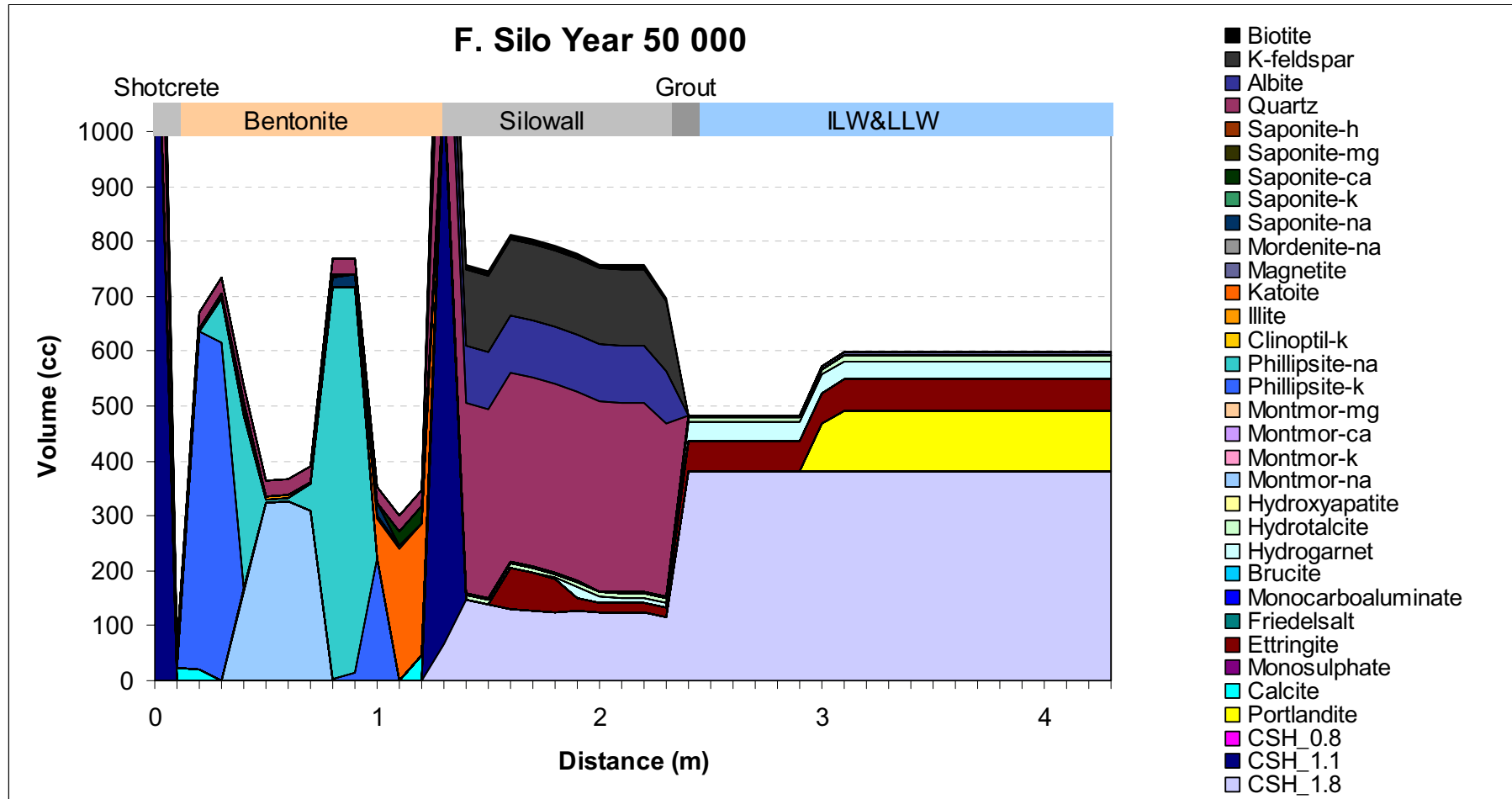


Figure B-24. Mineral distribution in the Silo at year 50,000 (fracture model).

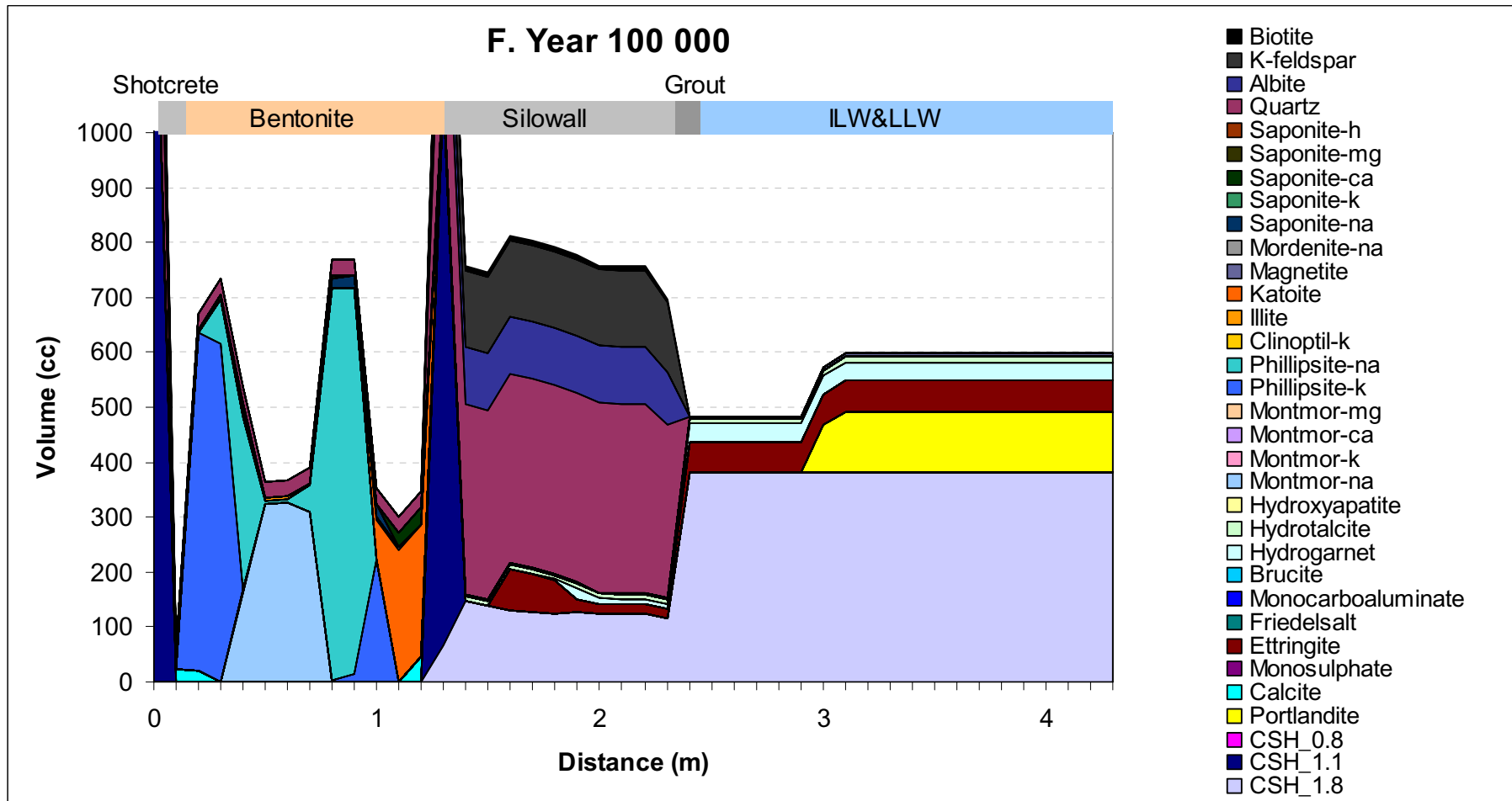


Figure B-25. Mineral distribution in the Silo at year 100,000 (fracture model).

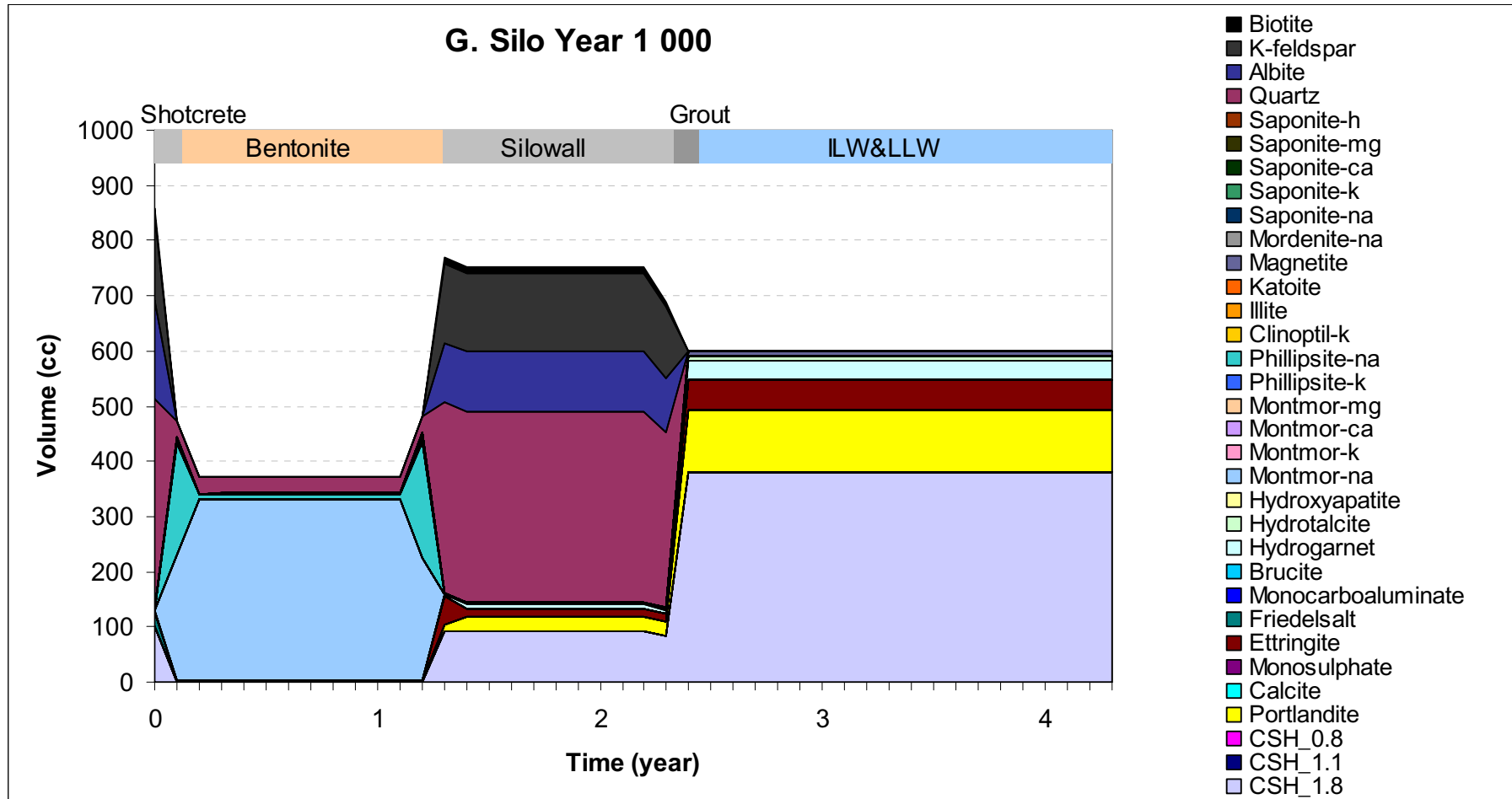
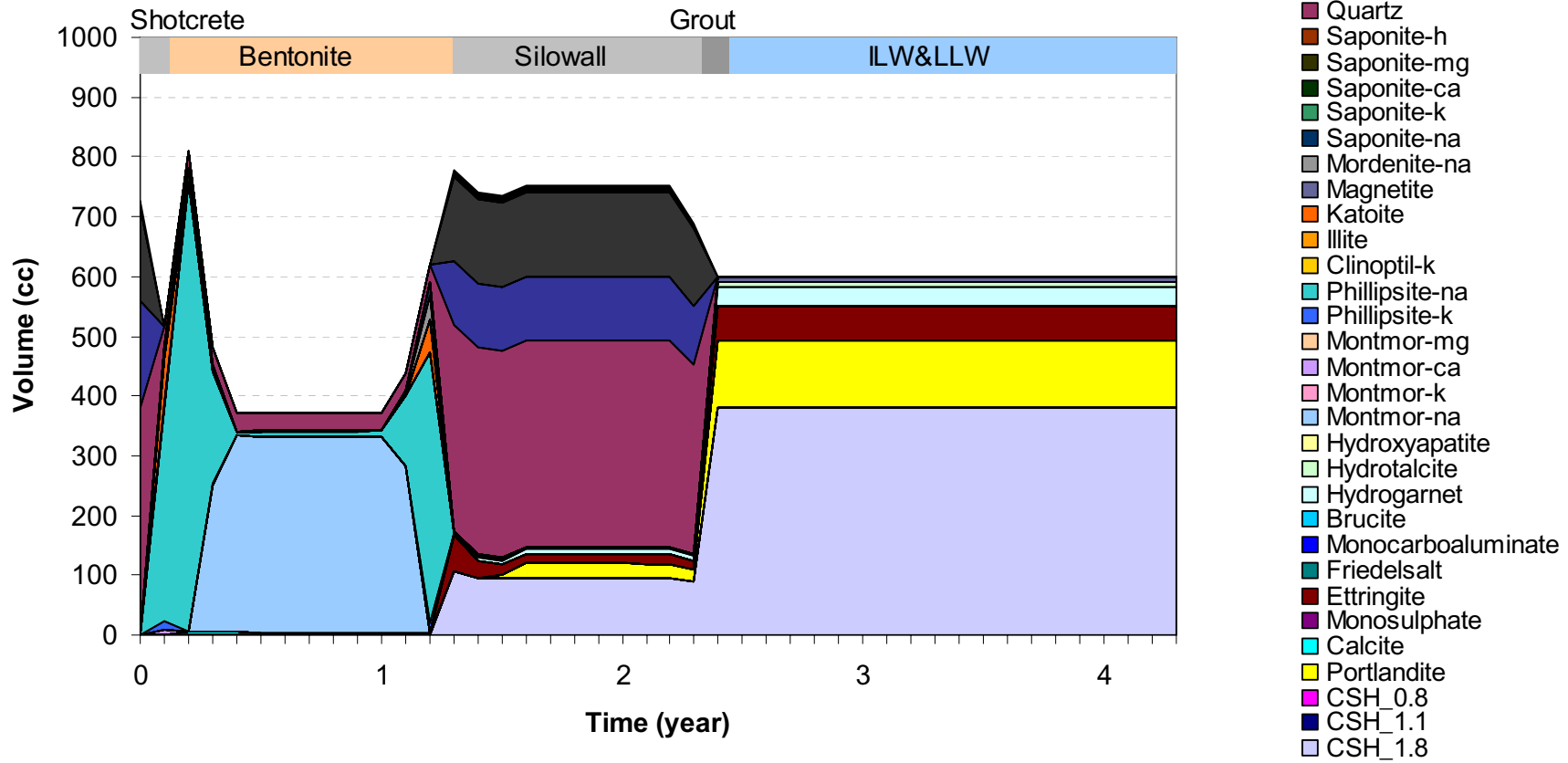


Figure B-26. Mineral distribution in the Silo at year 1,000 (freeze-thaw model).

G. Silo Year 10 000



70

Figure B-27. Mineral distribution in the Silo at year 10,000 (freeze-thaw model).

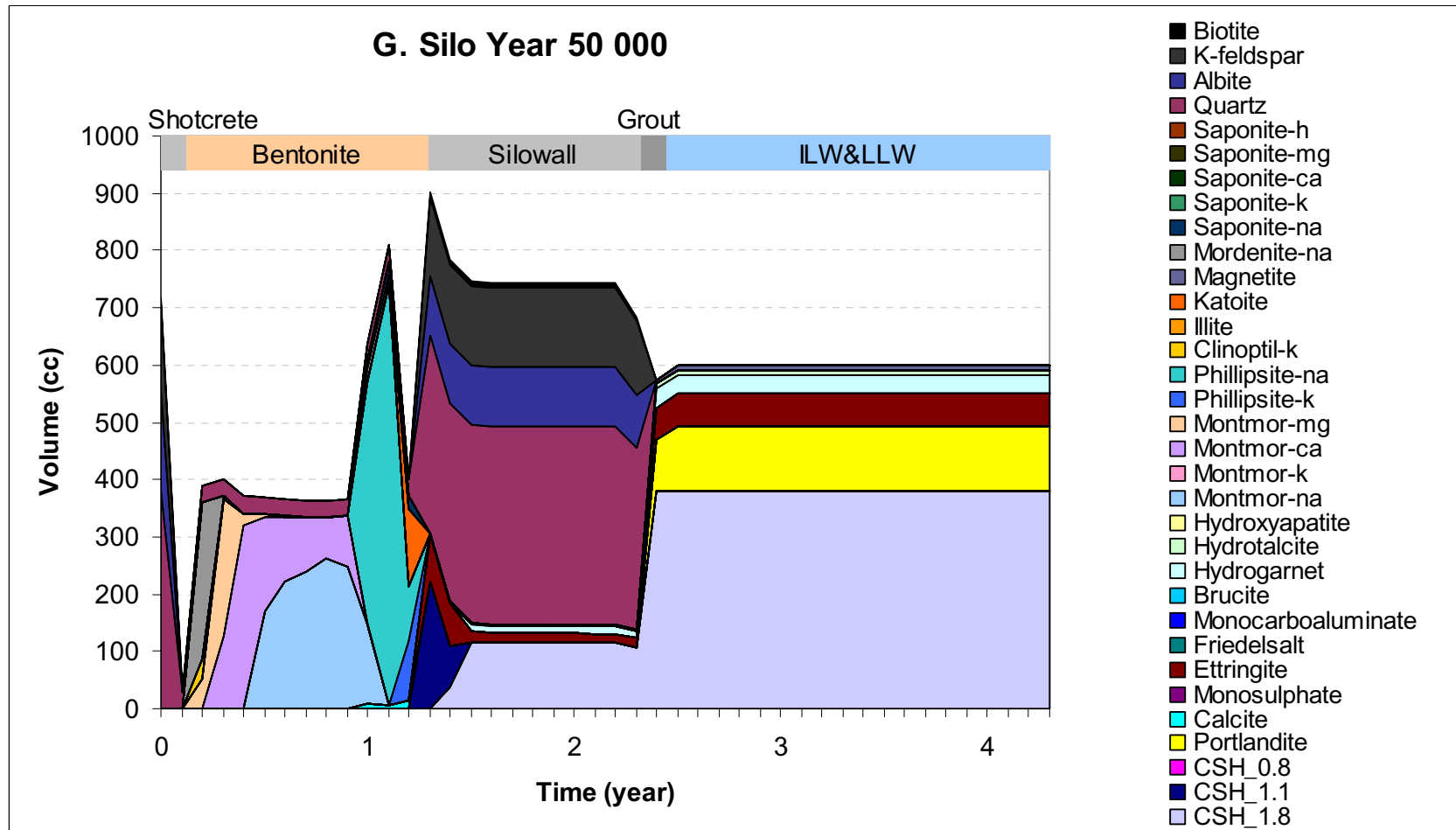
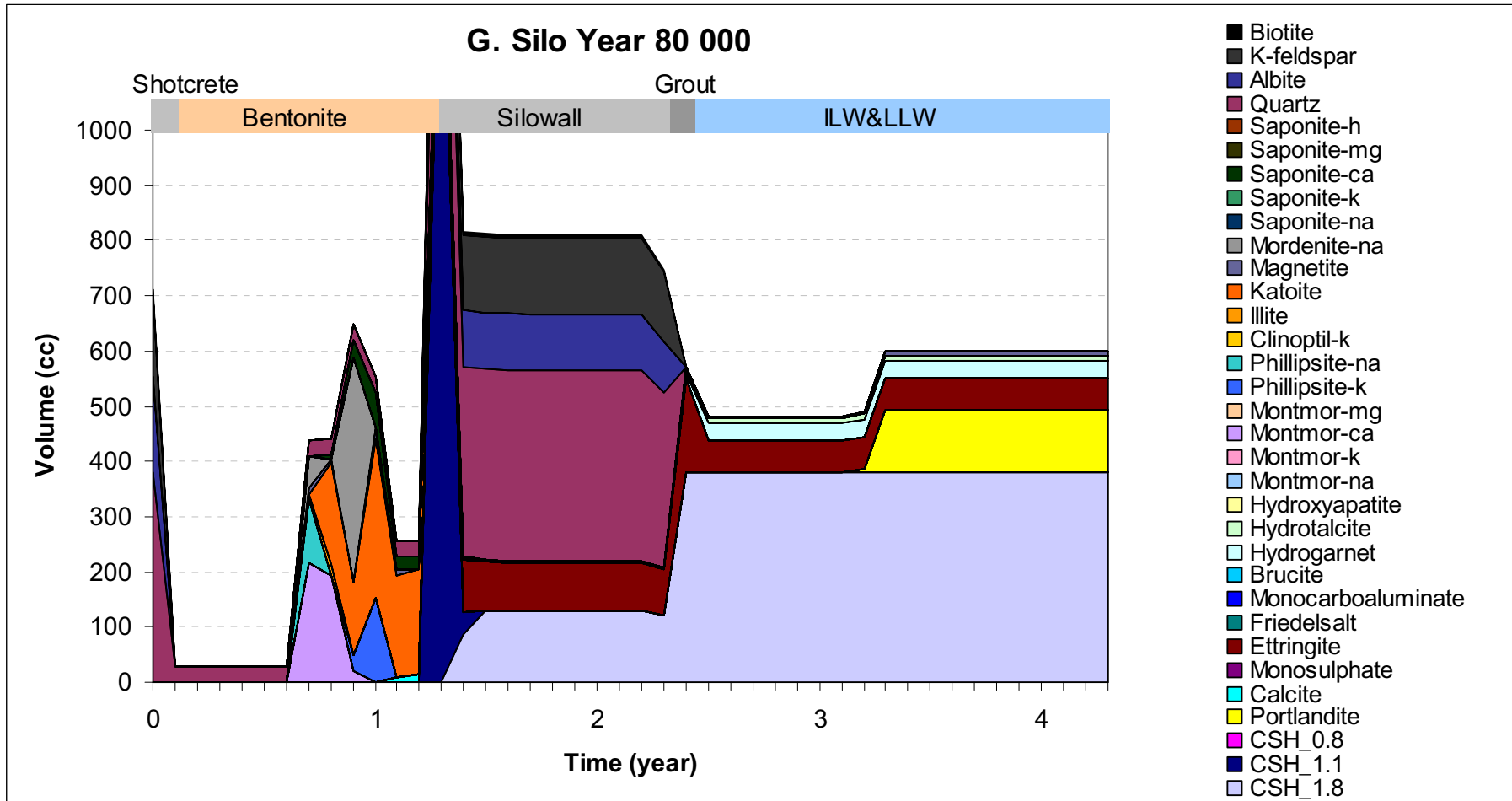


Figure B-28. Mineral distribution in the Silo at year 50,000 (freeze-thaw model).

G. Silo Year 80 000



72

Figure B-29. Mineral distribution in the Silo at year 80,000 (freeze-thaw model).

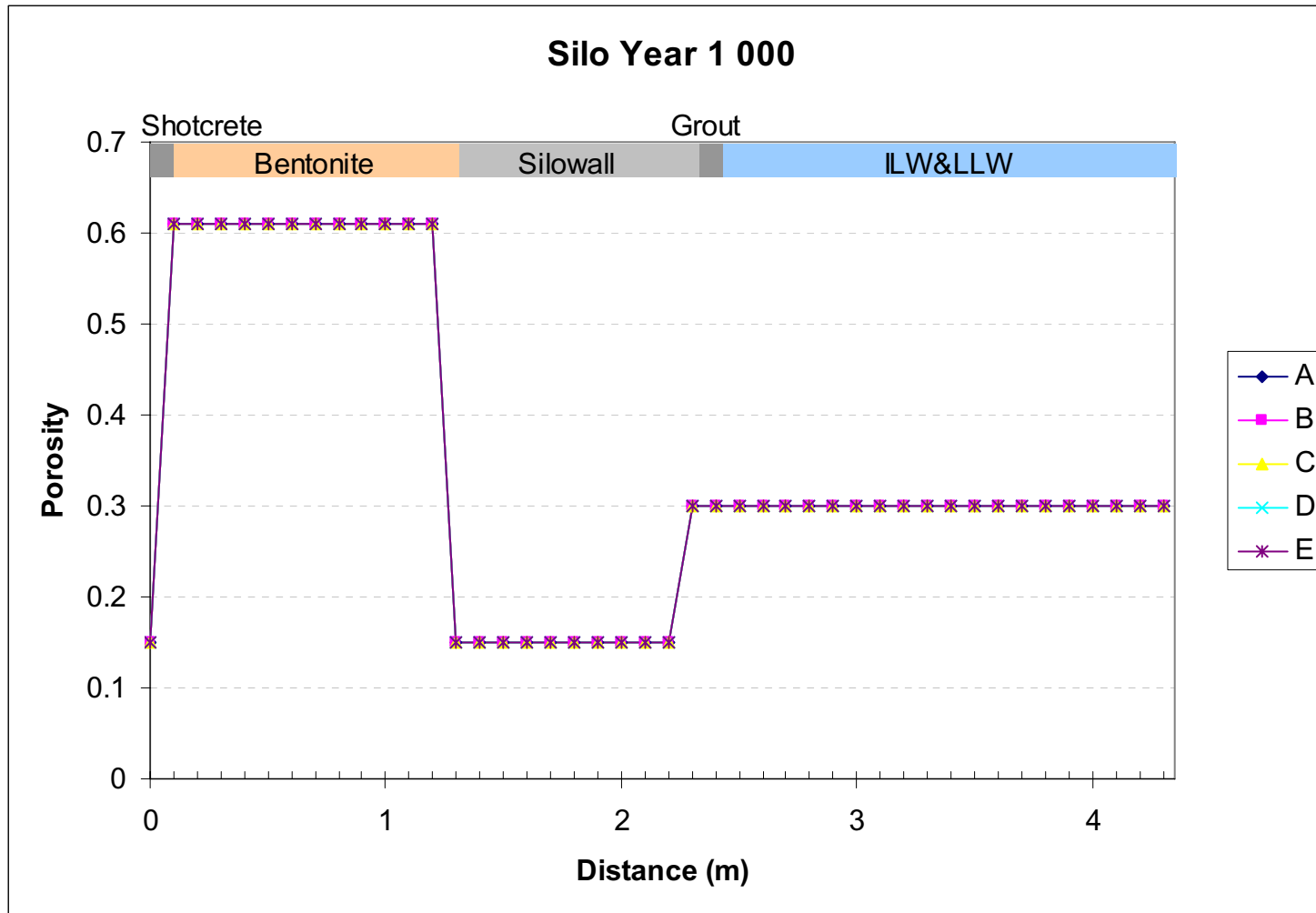


Figure B-30. Porosity distribution in the Silo at year 1,000.



Figure B-31. Porosity distribution in the Silo at year 10,000.

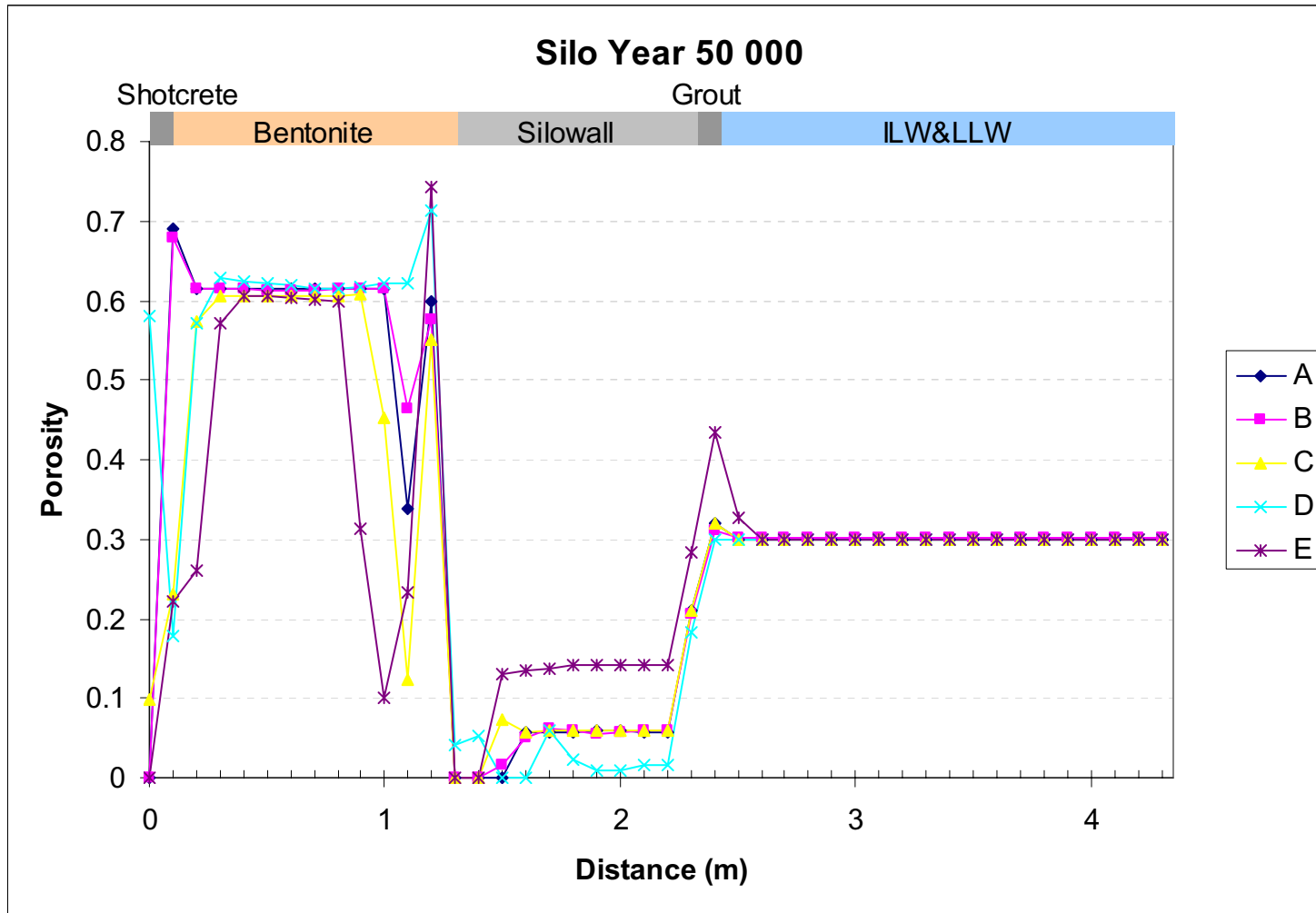


Figure B-32. Porosity distribution in the Silo at year 50,000.

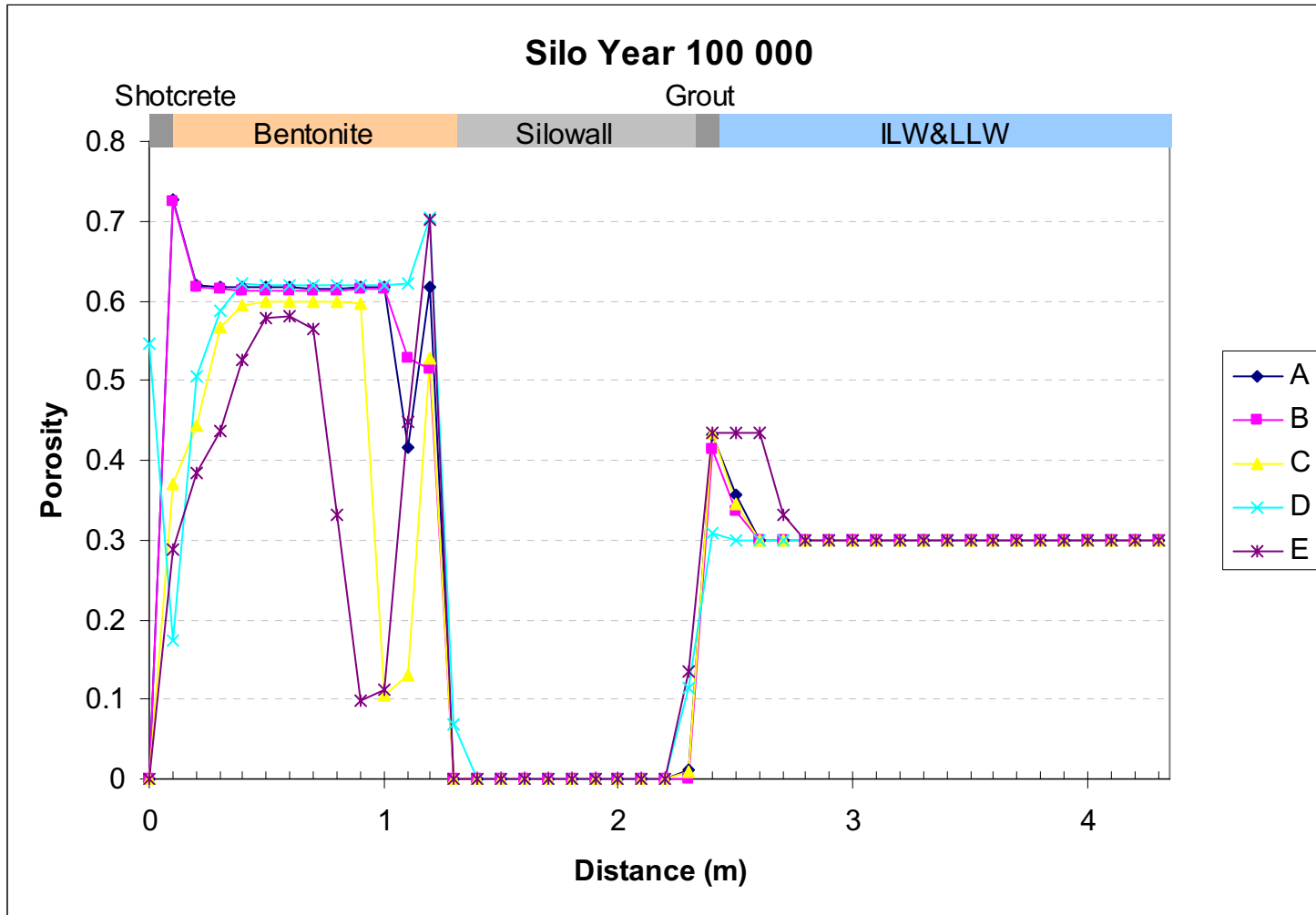


Figure B-33. Porosity distribution in the Silo at year 100,000.

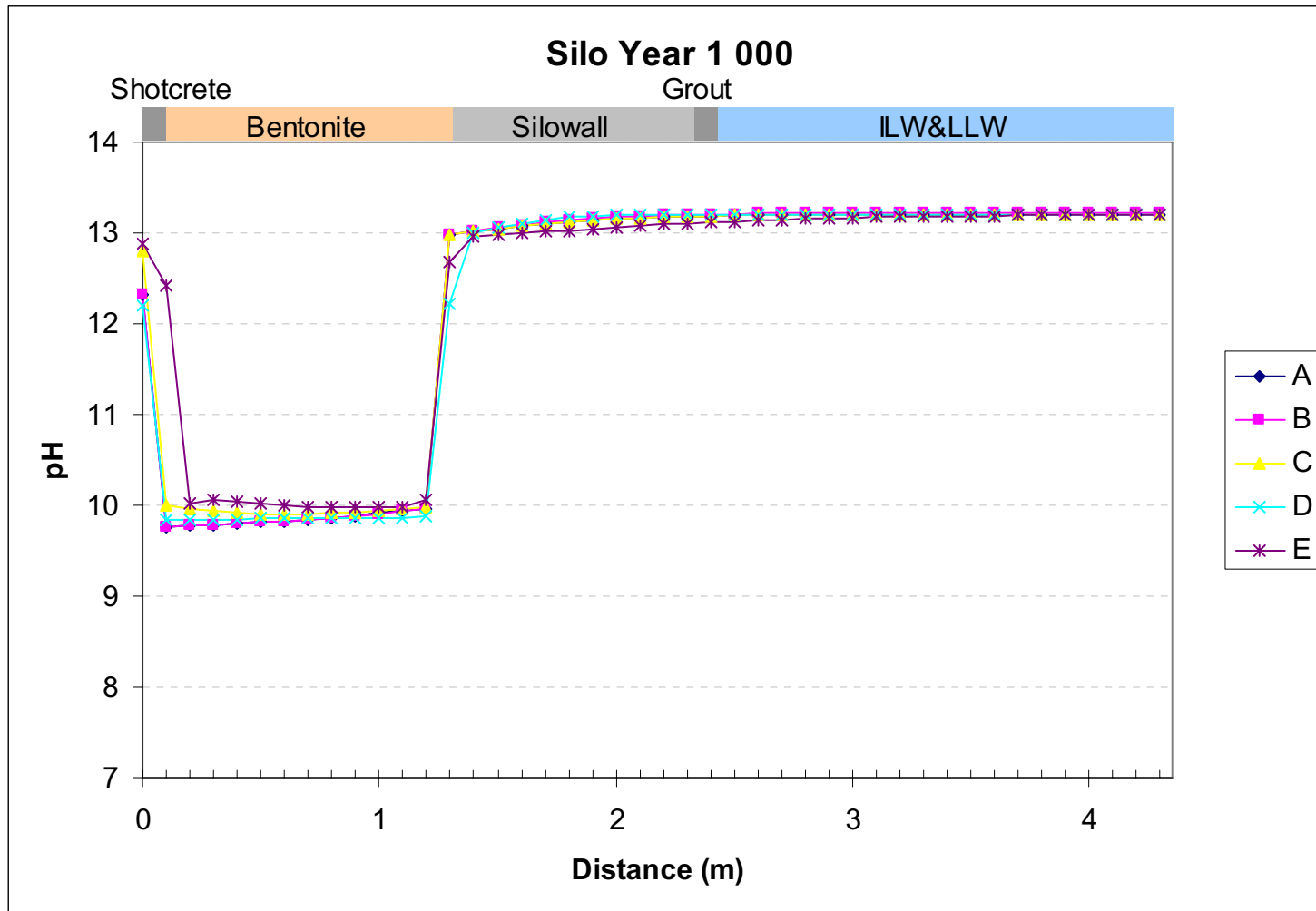


Figure B-34. pH distribution in the Silo at year 1,000.

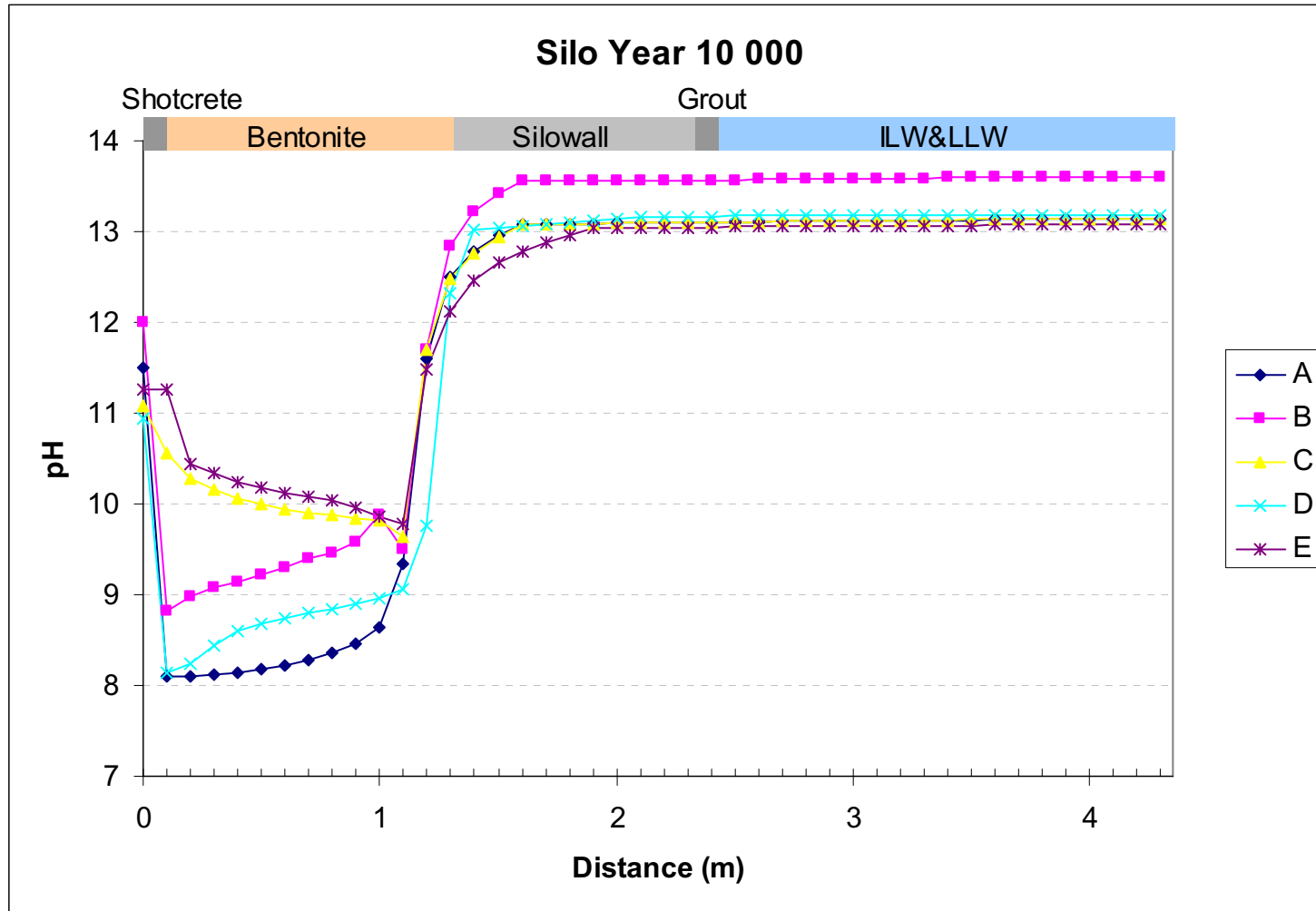


Figure B-35. pH distribution in the Silo at year 10,000.

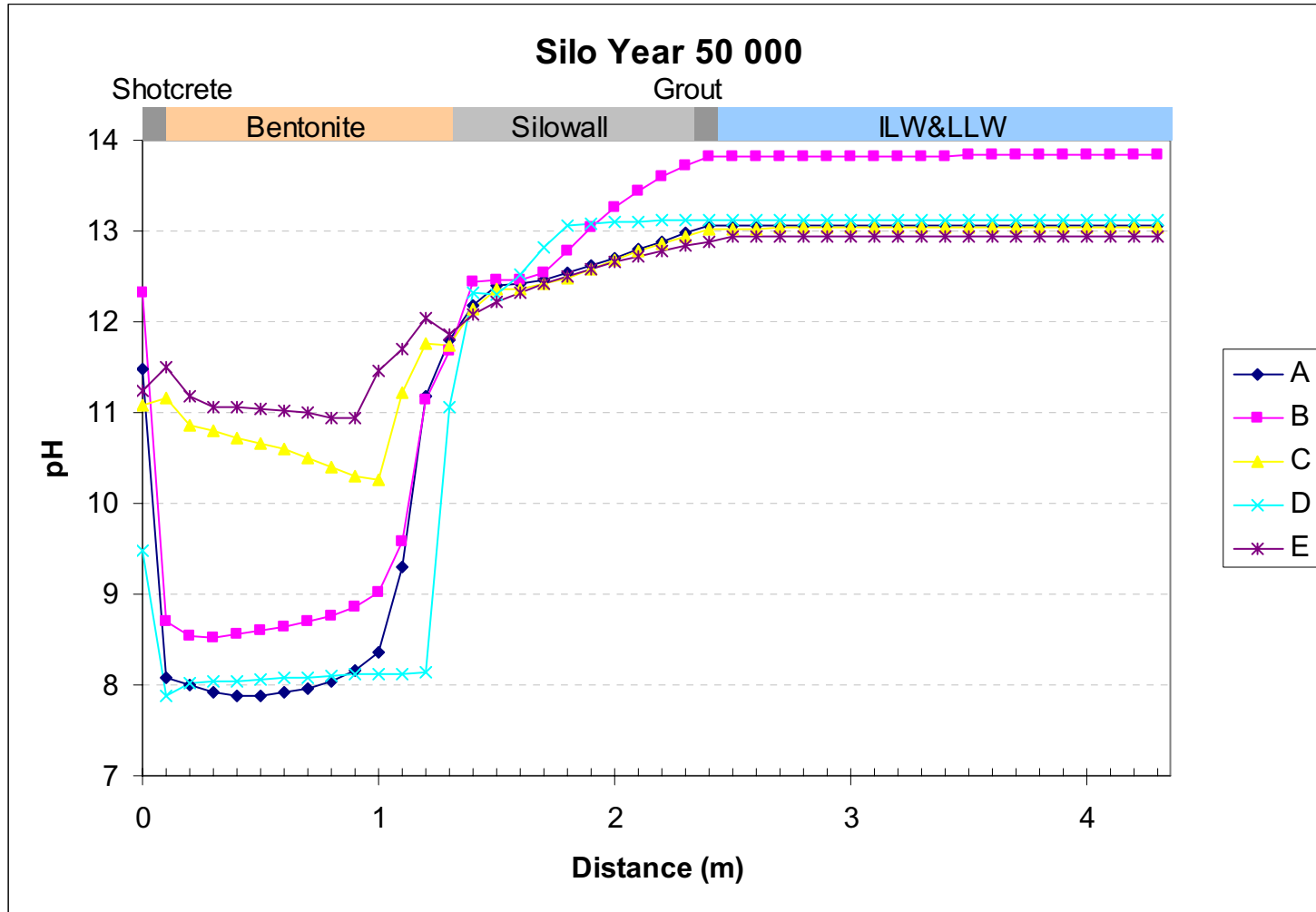


Figure B-36. pH distribution in the Silo at year 50,000.

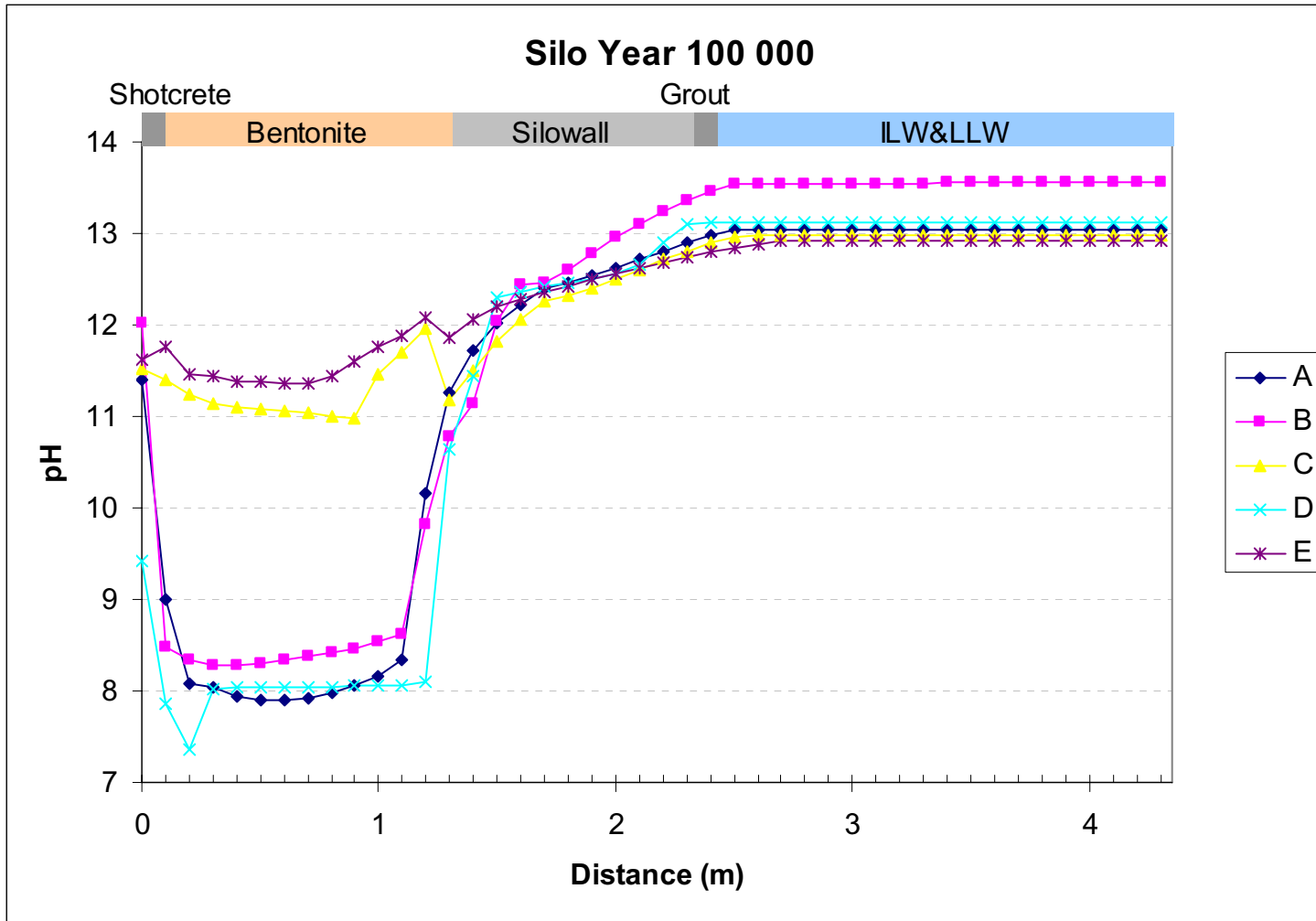


Figure B-37. pH distribution in the Silo at year 100,000.

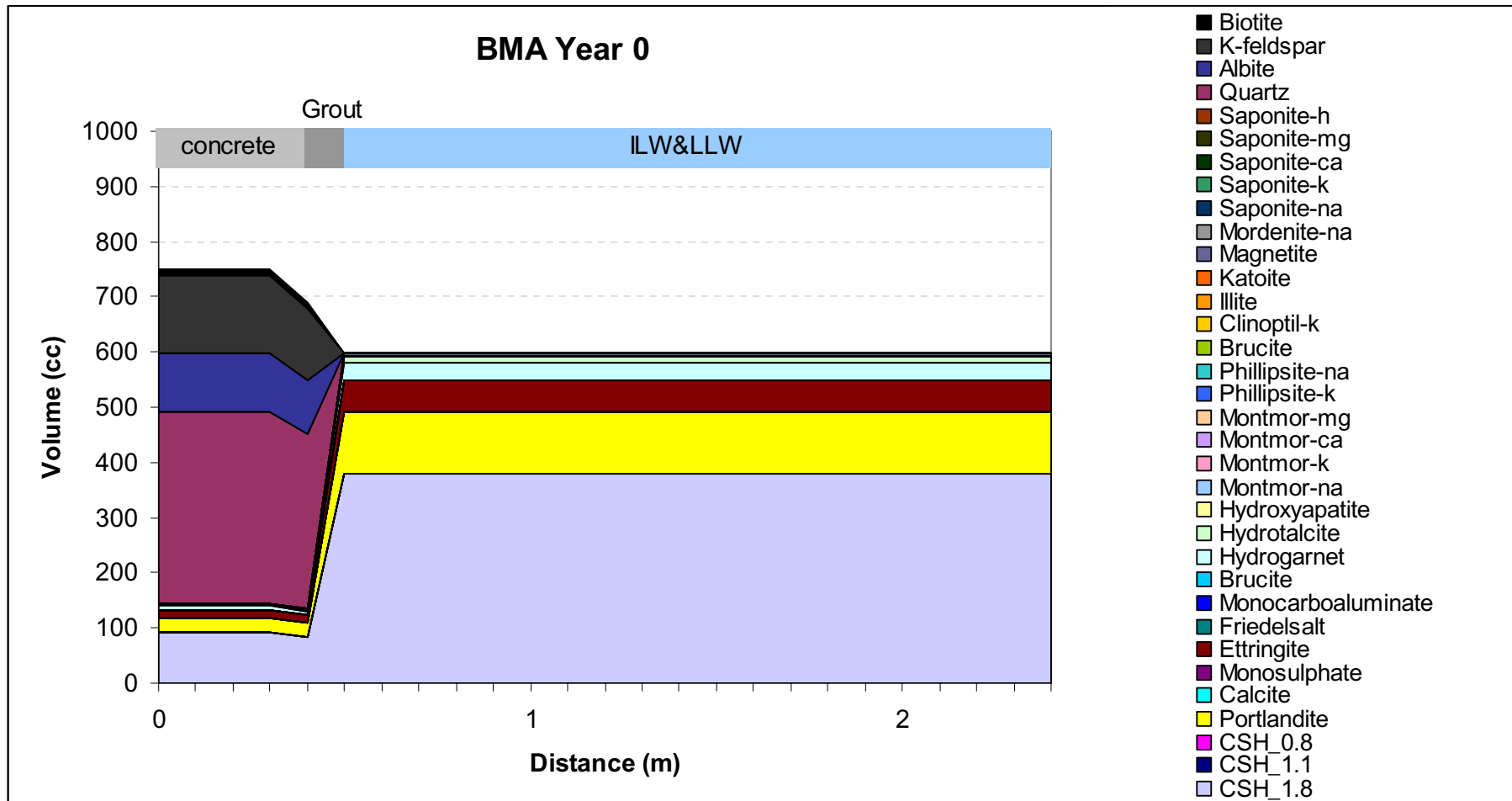


Figure B-38. Initial mineral distribution in BMA.

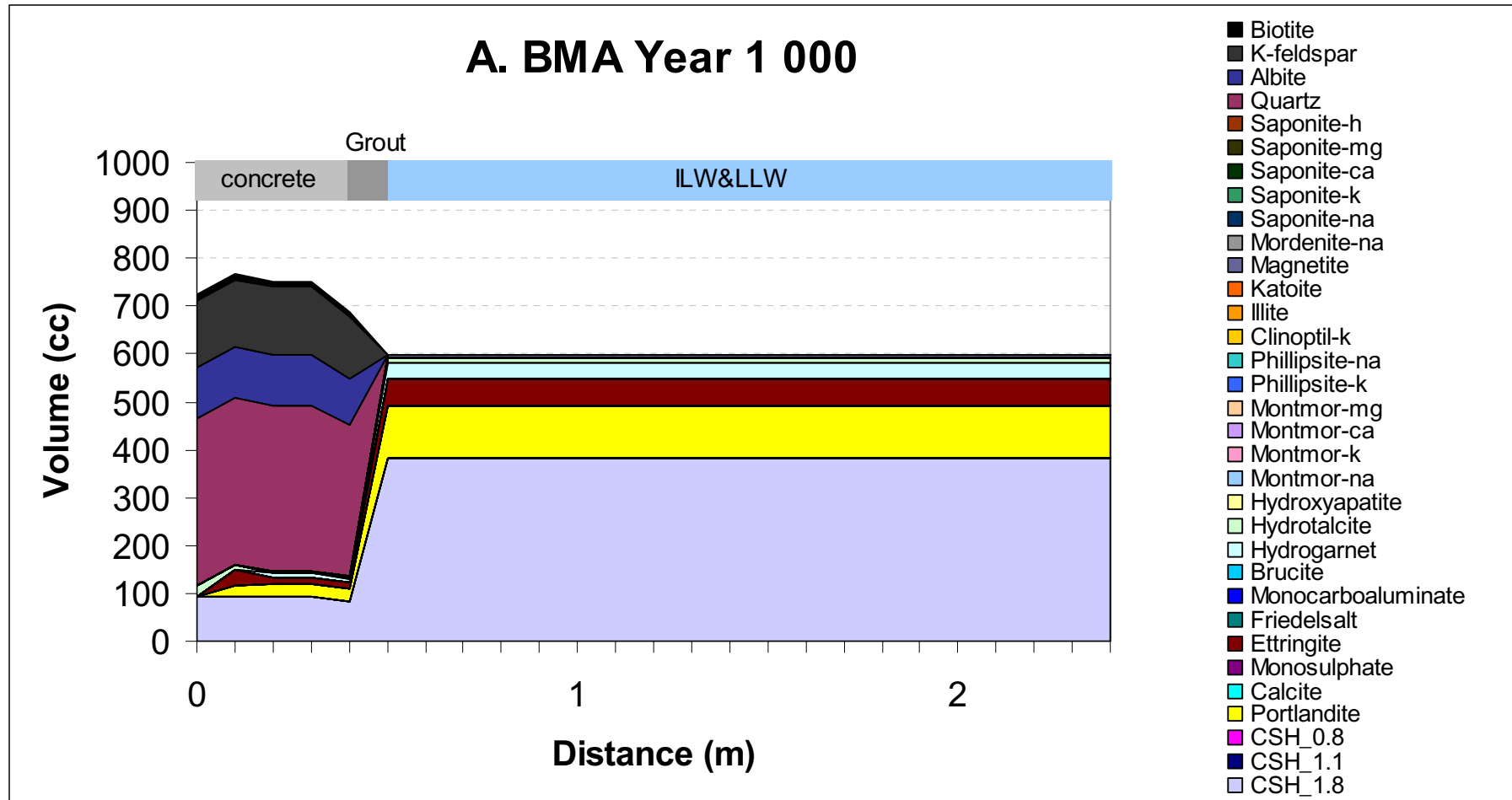


Figure B-39. Mineral distribution in BMA at year 1,000 (fixed diffusivity, temperature and water composition).

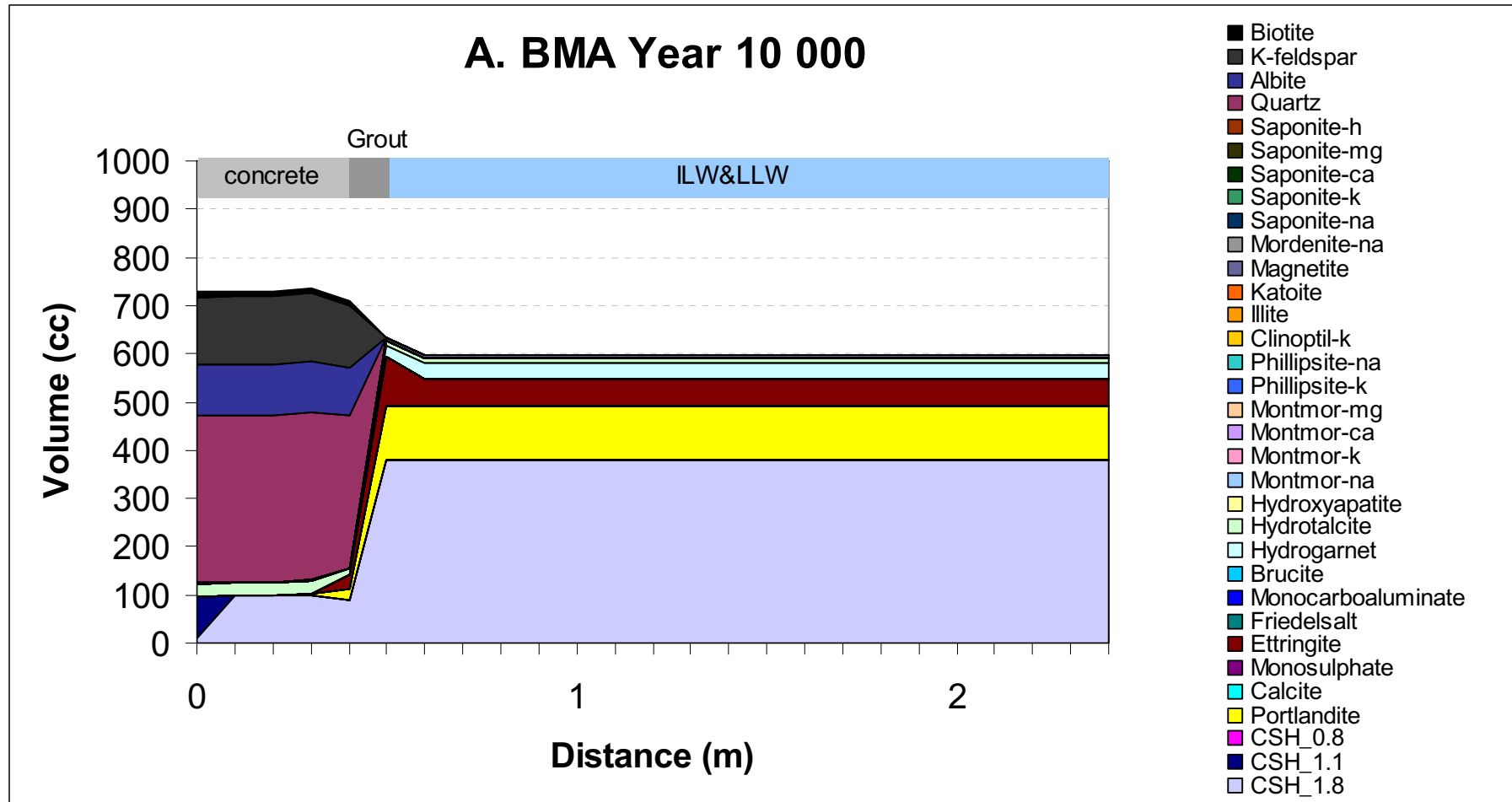


Figure B-40. Mineral distribution in BMA at year 10,000 (fixed diffusivity, temperature and water composition).

A. BMA Year 50 000

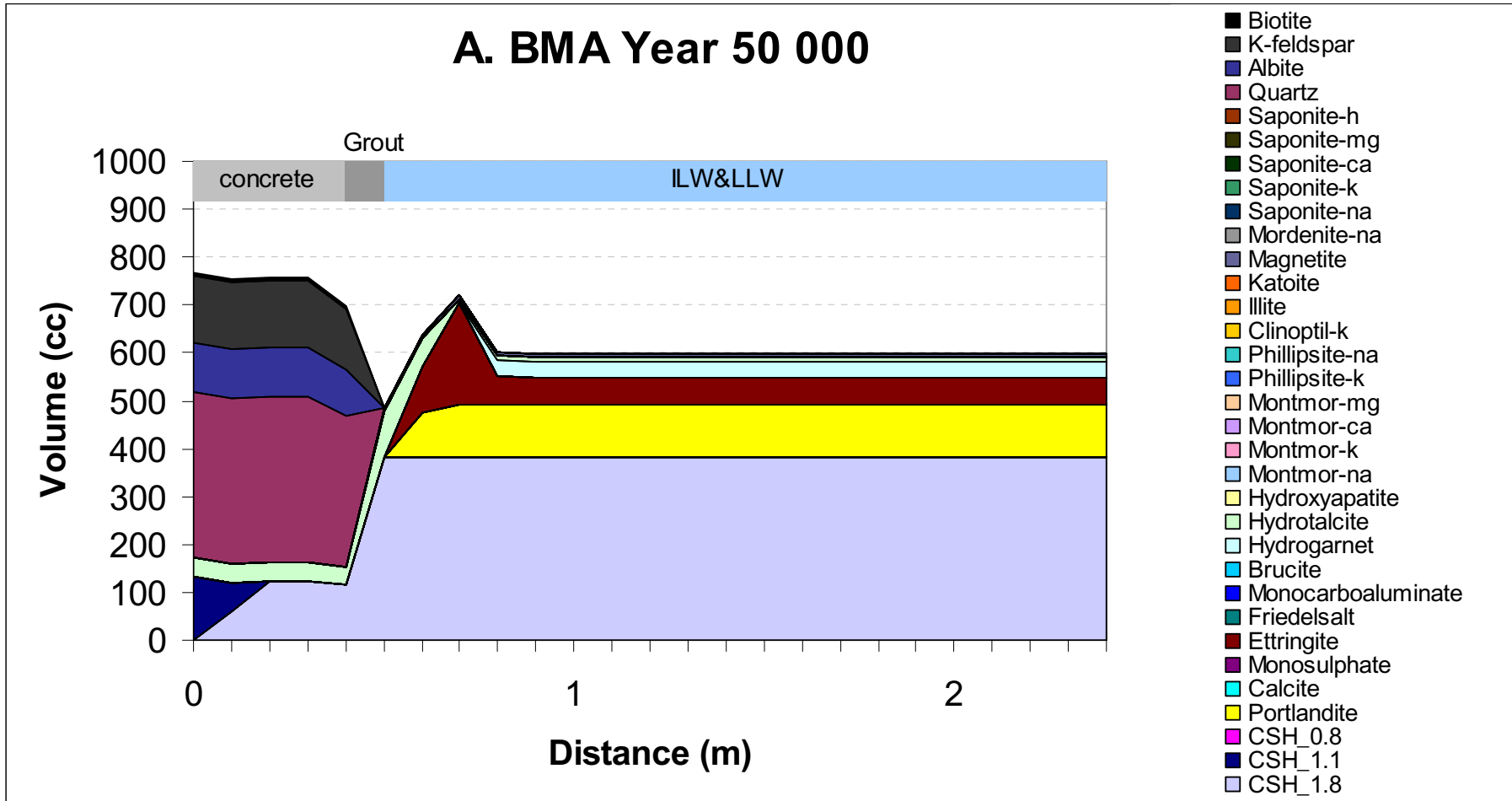


Figure B-41. Mineral distribution in BMA at year 50,000 (fixed diffusivity, temperature and water composition).

A. BMA Year 100 000

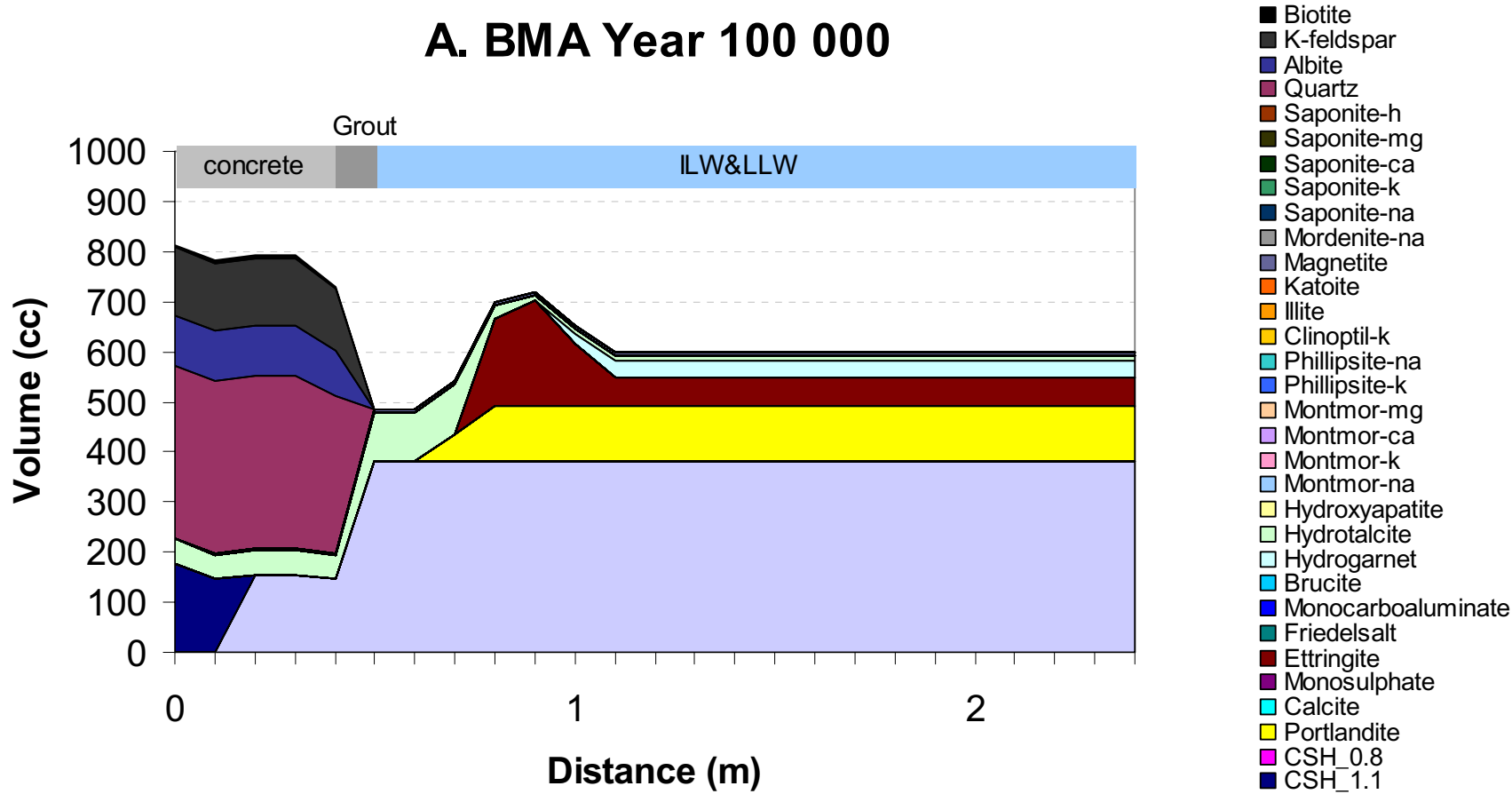


Figure B-42. Mineral distribution in BMA at year 100,000 (fixed diffusivity, temperature and water composition).

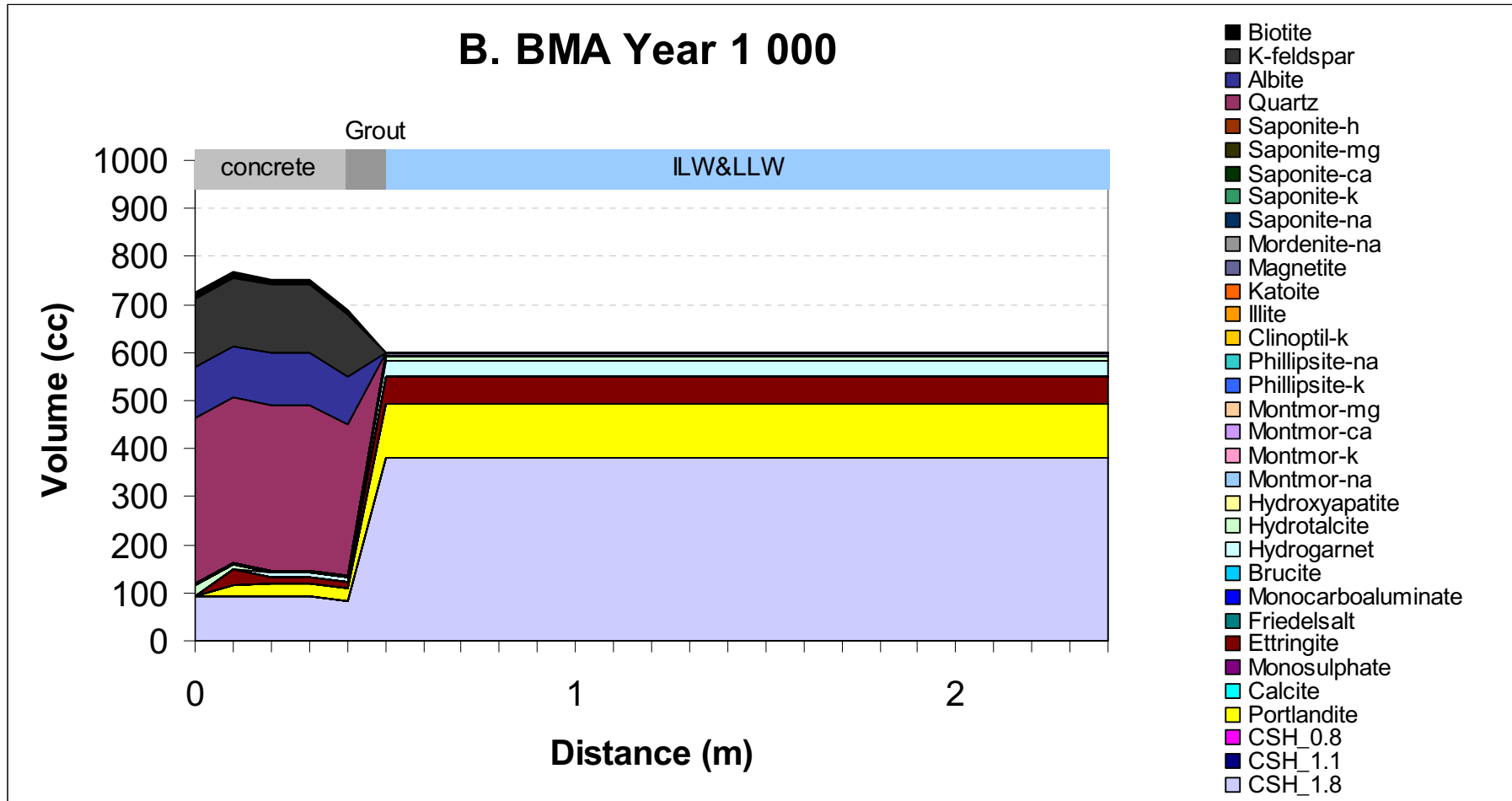


Figure B-43. Mineral distribution in BMA at year 1,000 (fixed diffusivity and water composition, variable temperature).

B. BMA Year 10 000

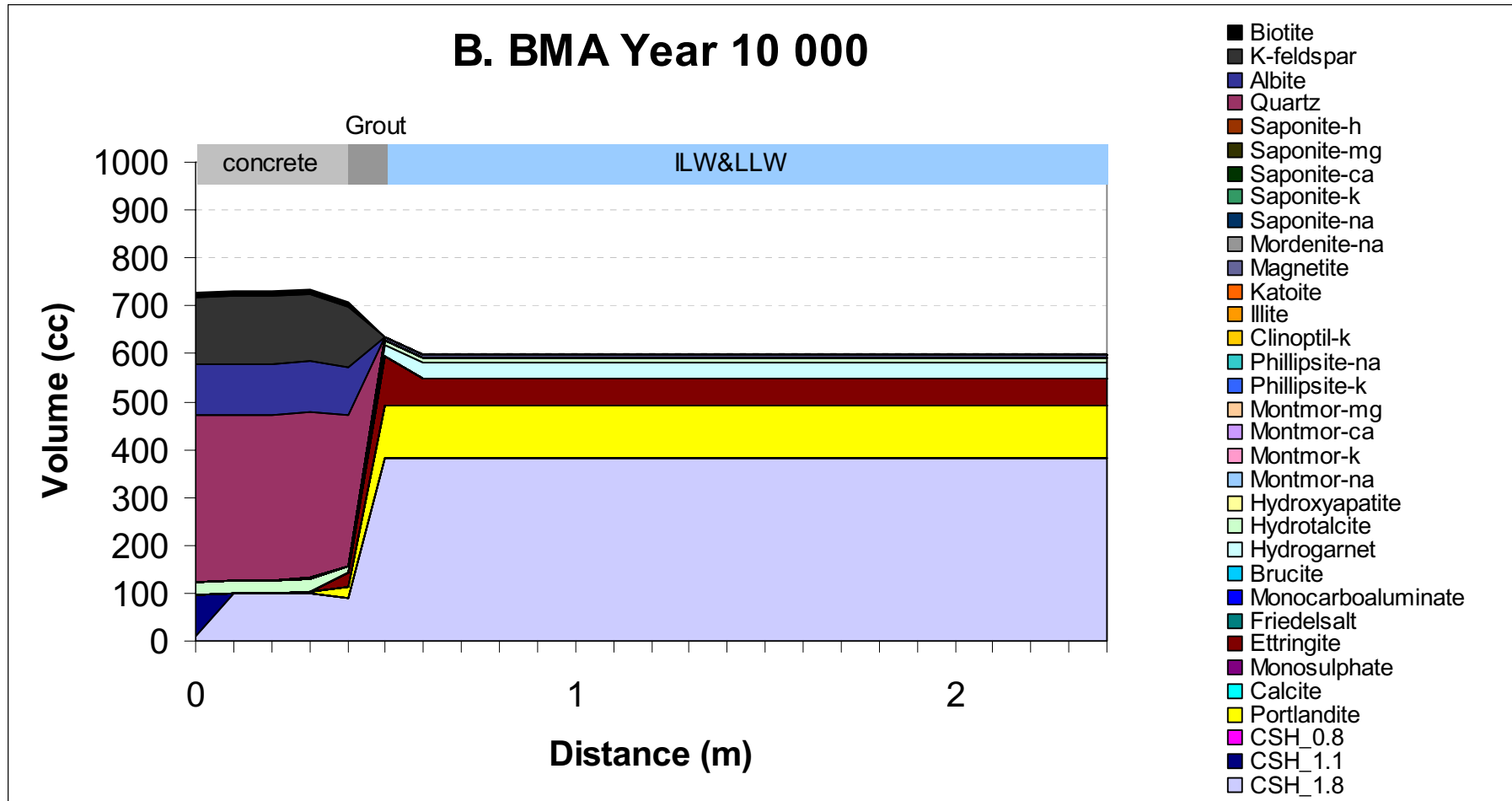


Figure B-44. Mineral distribution in BMA at year 10,000 (fixed diffusivity and water composition, variable temperature).

B. BMA Year 50 000

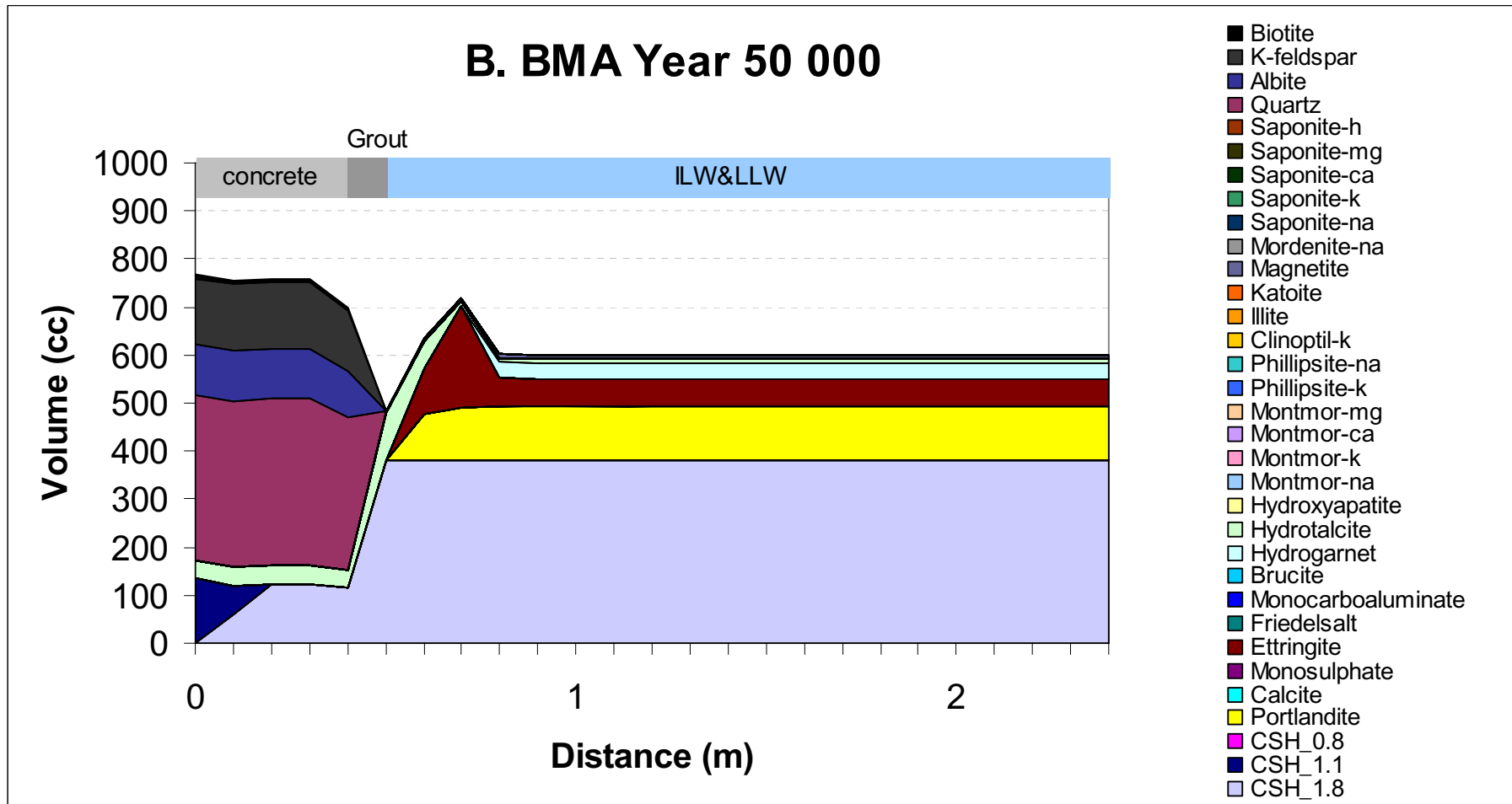


Figure B-45. Mineral distribution in BMA at year 50,000 (fixed diffusivity and water composition, variable temperature).

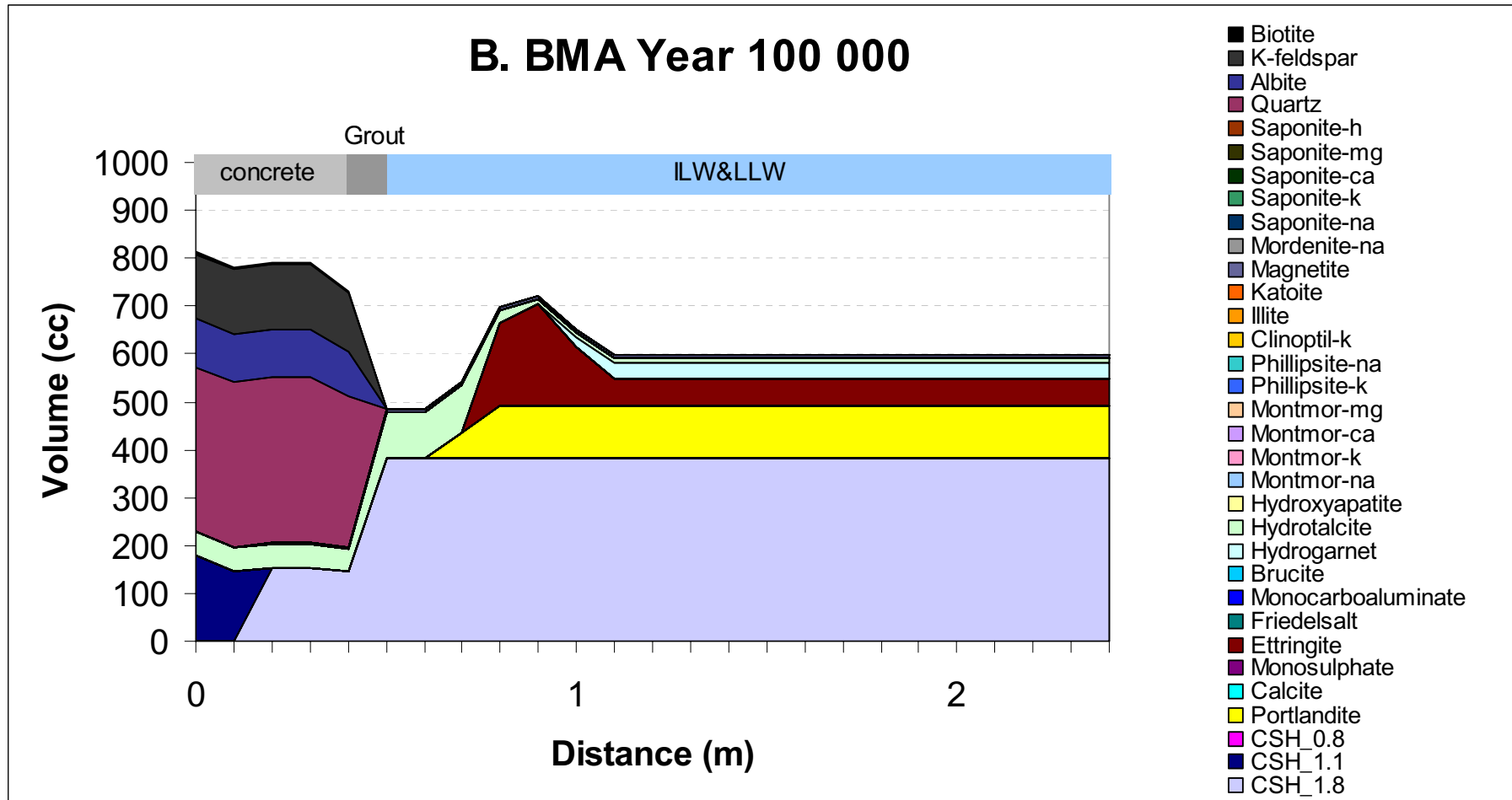
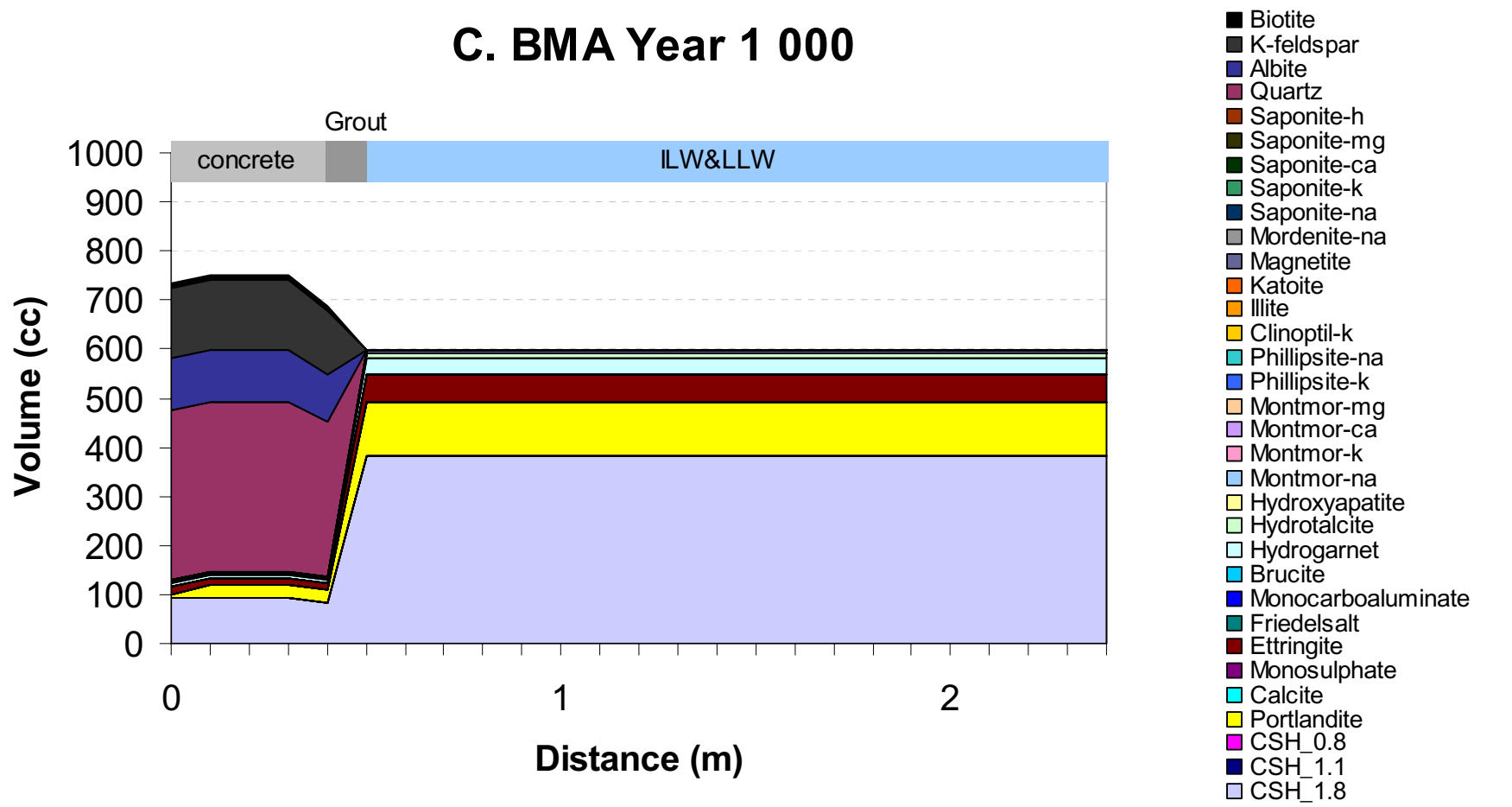


Figure B-46. Mineral distribution in BMA at year 100,000 (fixed diffusivity and water composition, variable temperature).

C. BMA Year 1 000



06

Figure B-47. Mineral distribution in BMA at year 1,000 (fixed diffusivity and temperature, variable water composition).

C. BMA Year 10 000

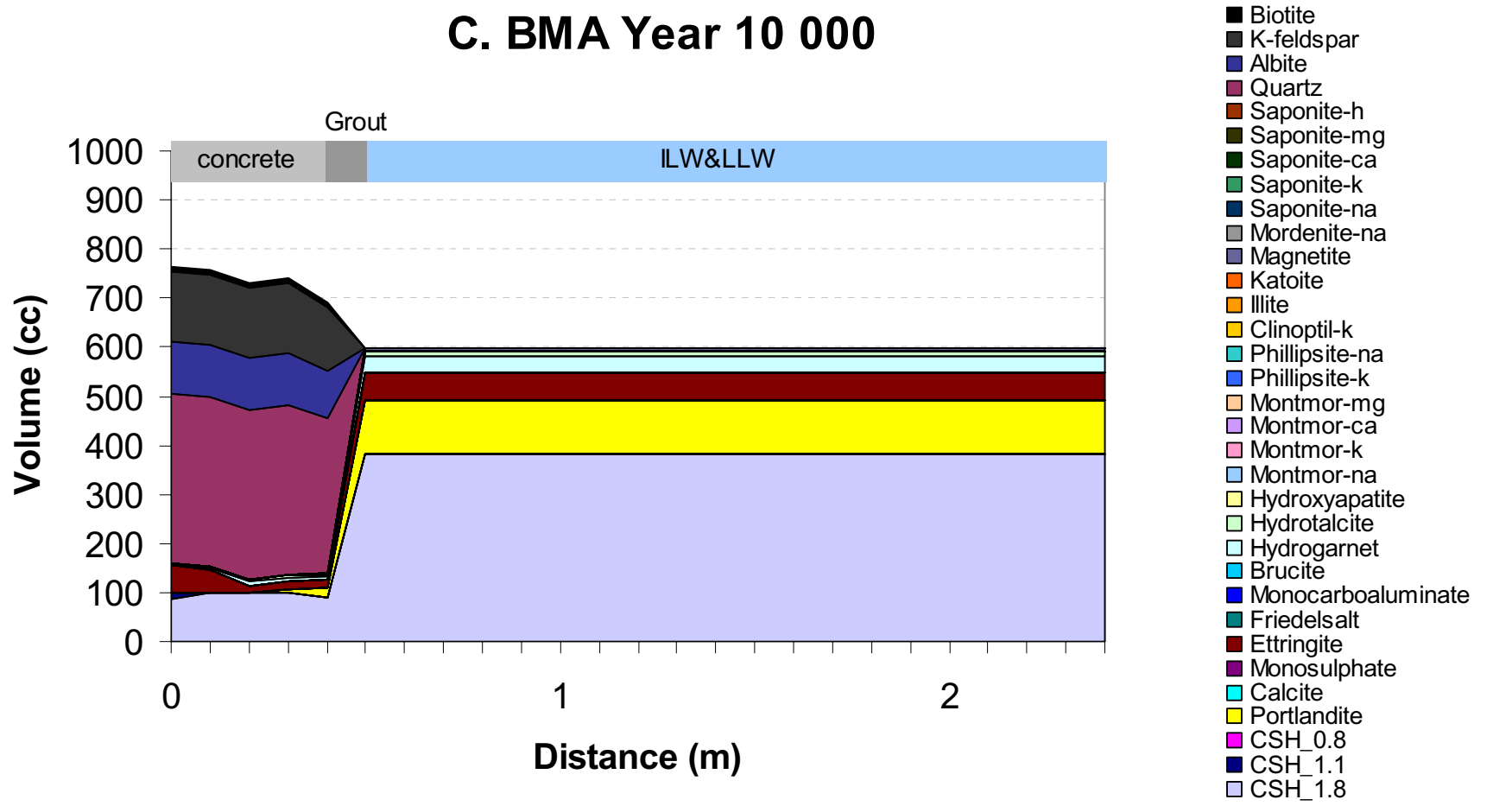


Figure B-48. Mineral distribution in BMA at year 10,000 (fixed diffusivity and temperature, variable water composition).

C. BMA Year 50 000

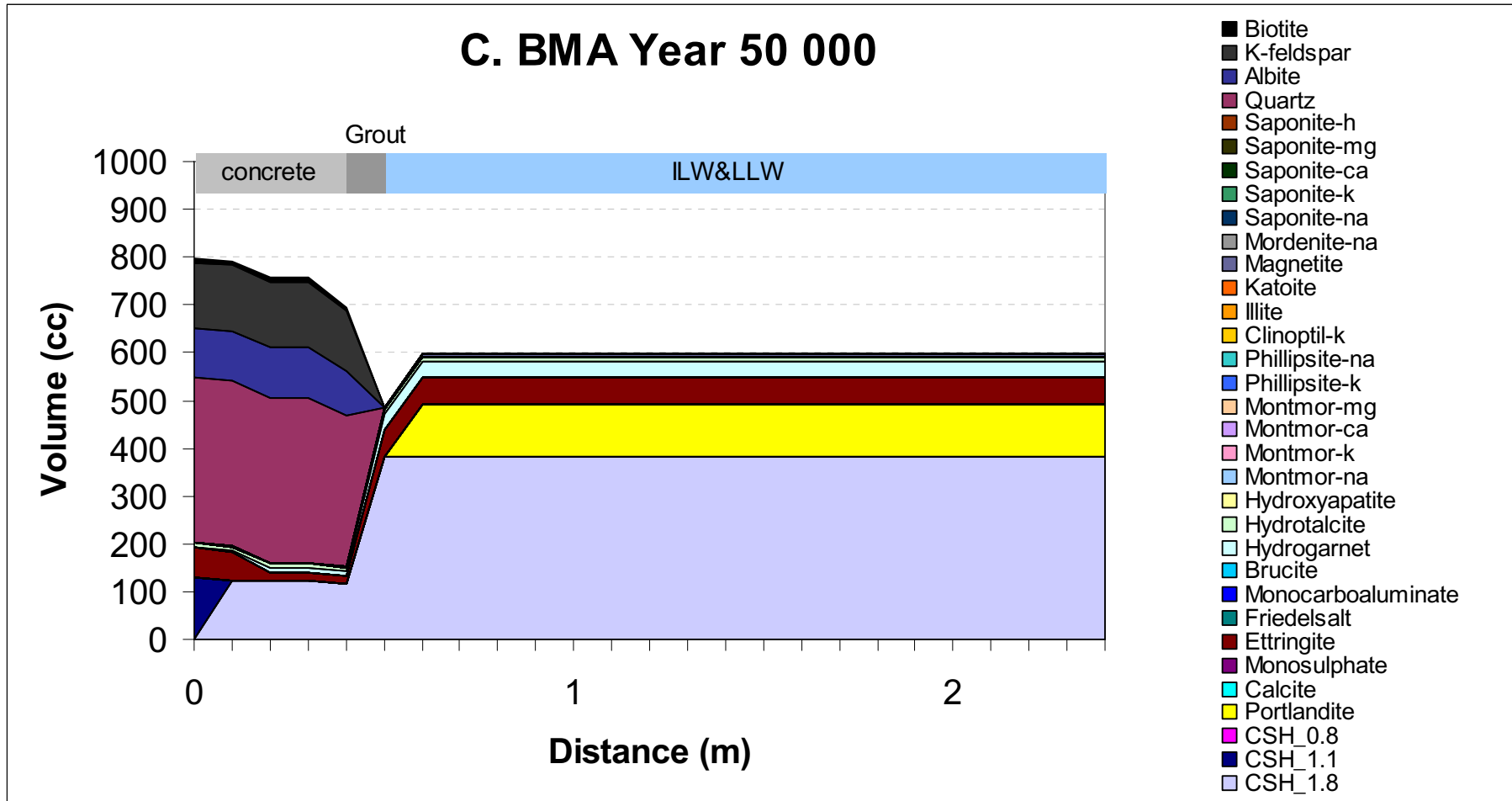


Figure B-49. Mineral distribution in BMA at year 50,000 (fixed diffusivity and temperature, variable water composition).

C. BMA Year 100 000

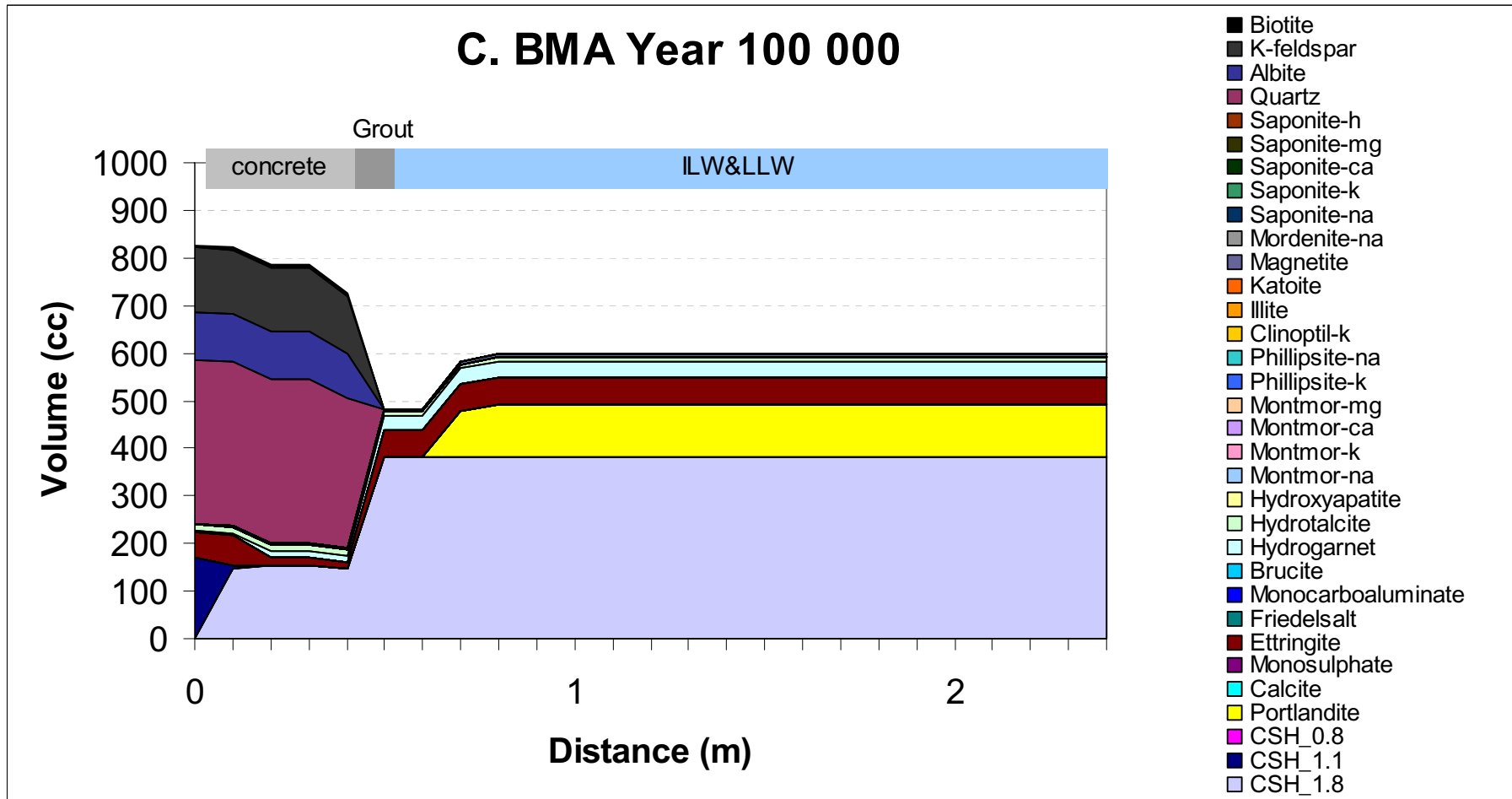


Figure B-50. Mineral distribution in BMA at year 100,000 (fixed diffusivity and temperature, variable water composition).

D. BMA Year 1 000

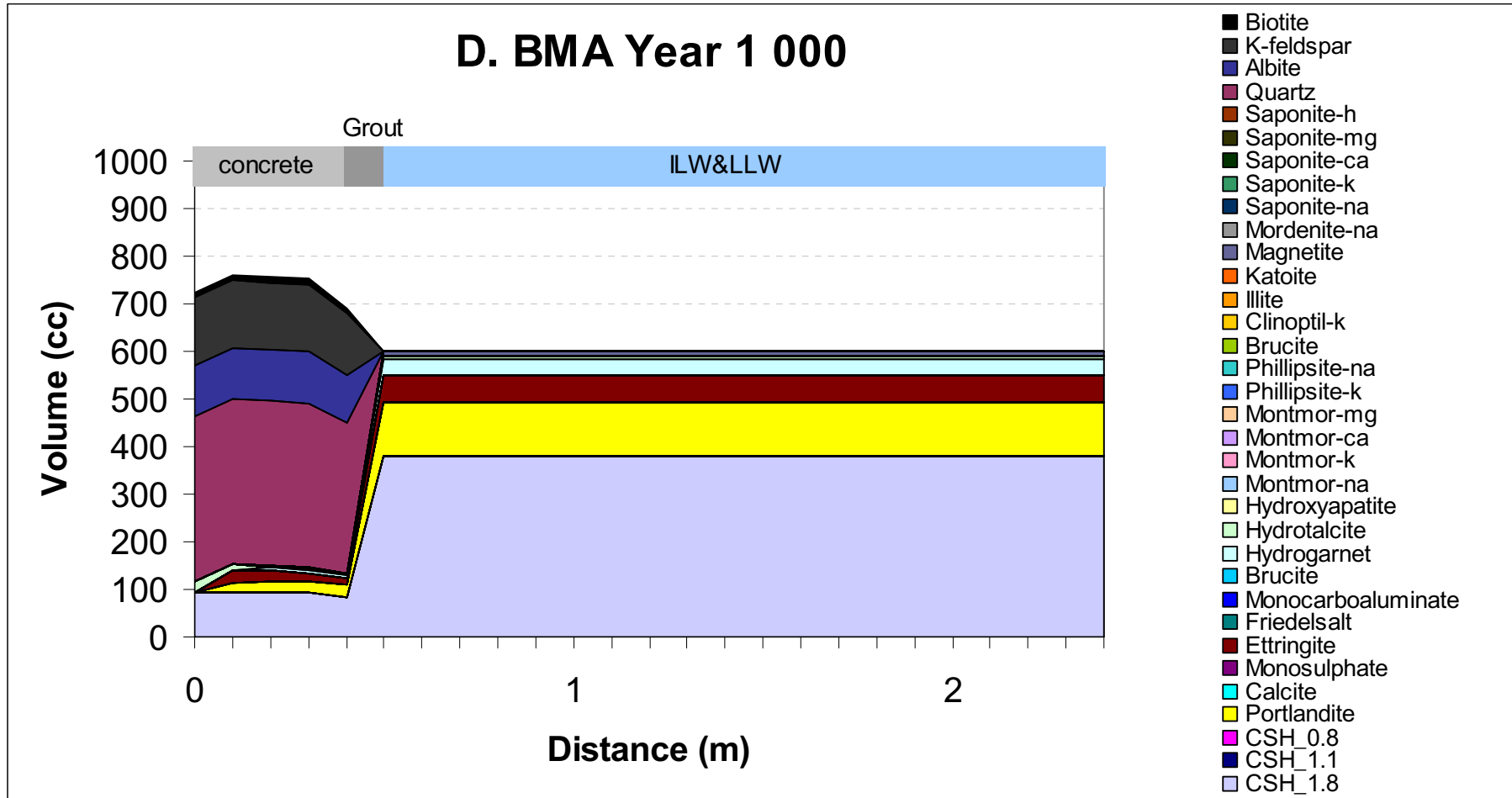


Figure B-51. Mineral distribution in BMA at year 1,000 (dynamic diffusivity, fixed temperature and water composition).

D. BMA Year 10 000

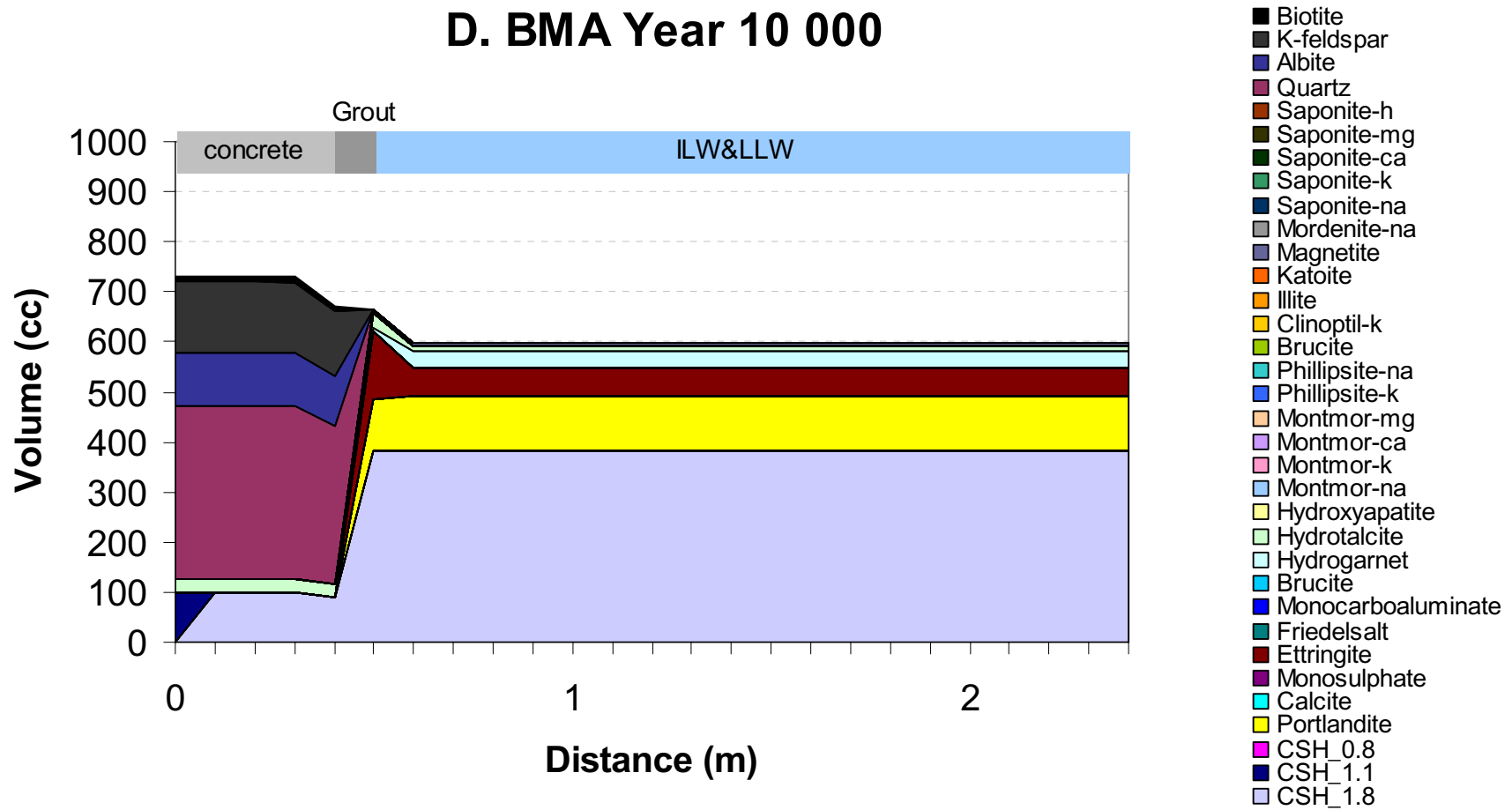


Figure B-52. Mineral distribution in BMA at year 10 ,000 (dynamic diffusivity, fixed temperature and water composition).

D. BMA Year 50 000

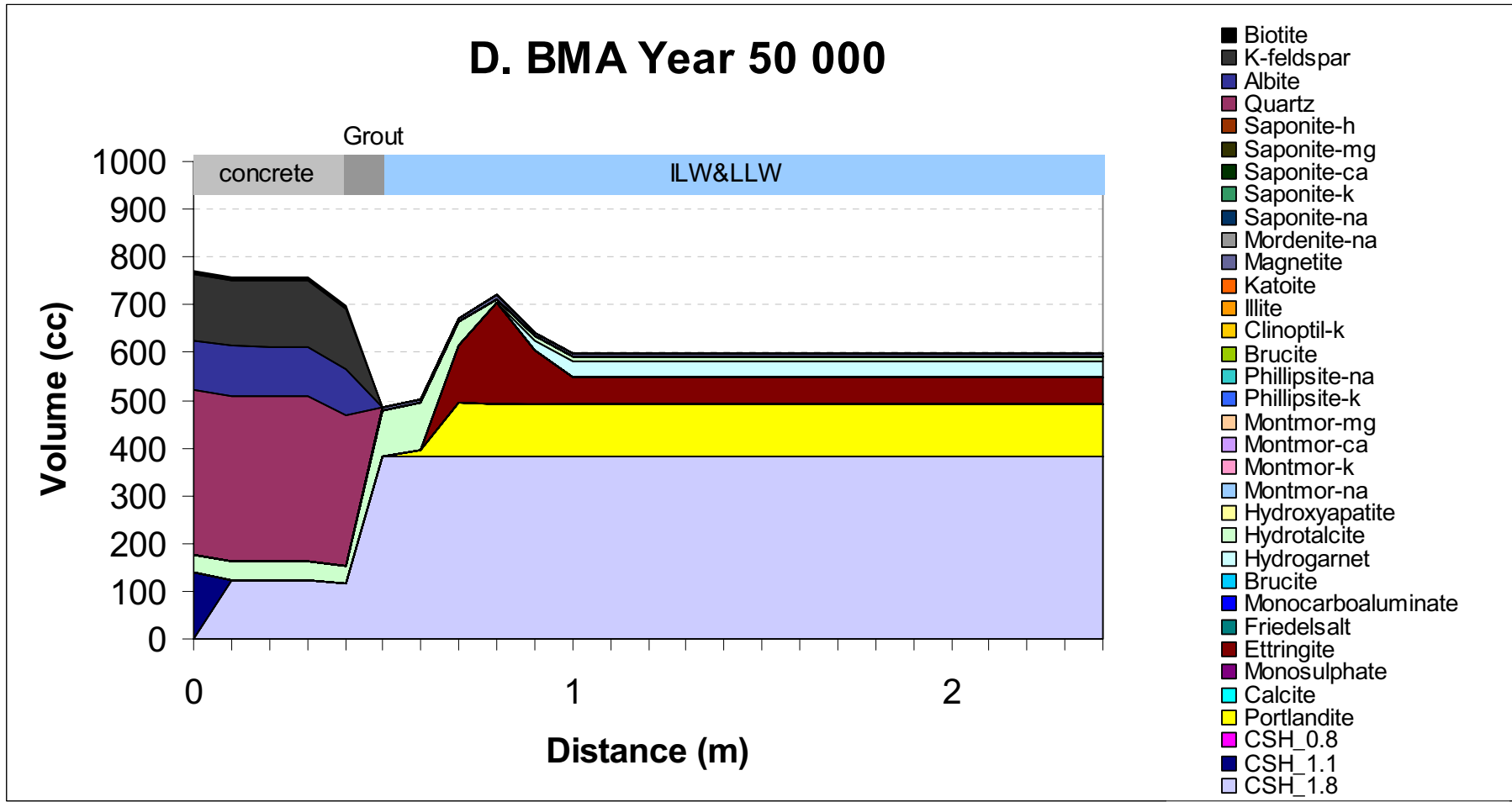


Figure B-53. Mineral distribution in BMA at year 50,000 (dynamic diffusivity, fixed temperature and water composition).

D. BMA Year 100 000

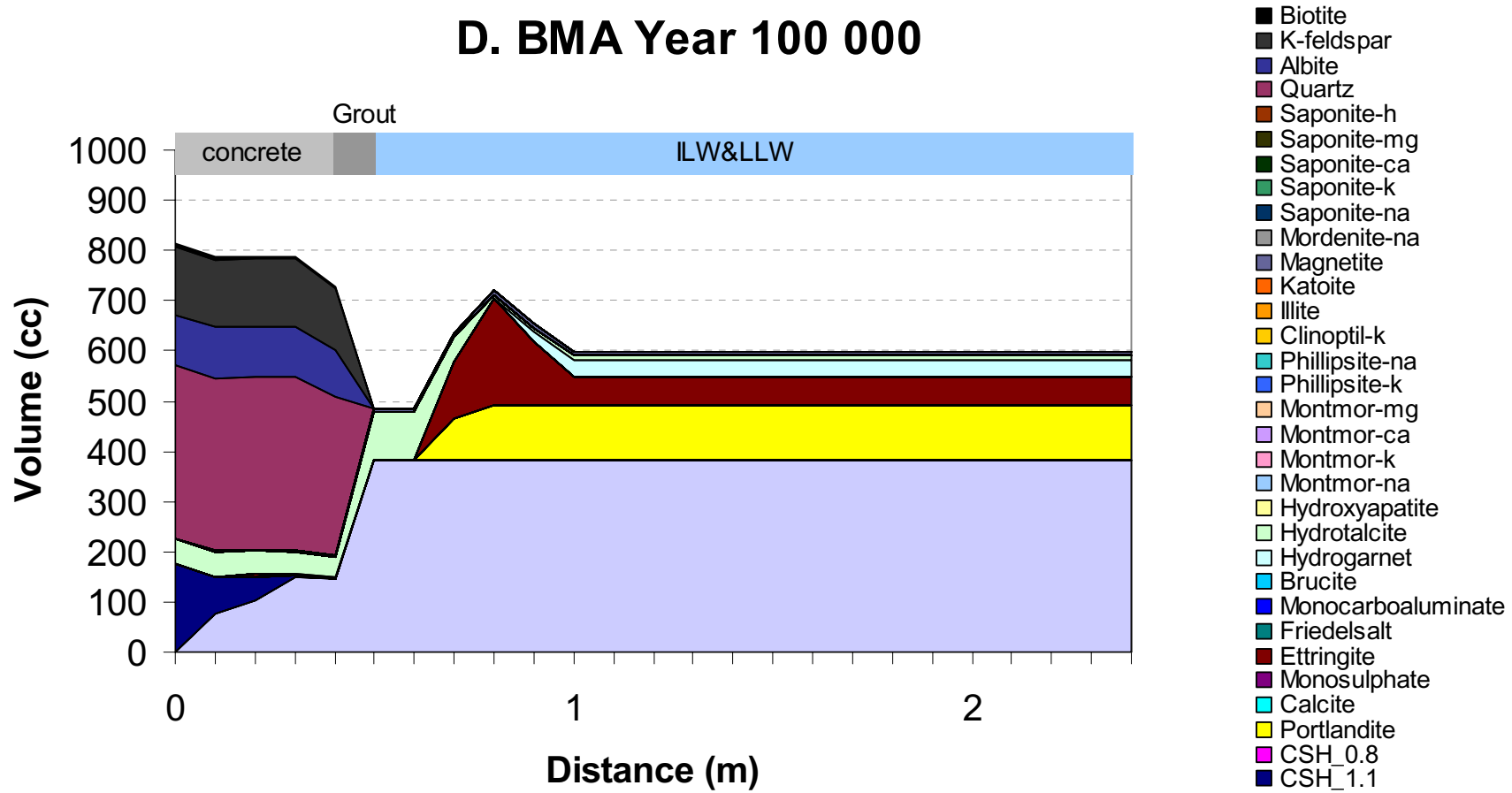


Figure B-54. Mineral distribution in BMA at year 100,000 (dynamic diffusivity, fixed temperature and water composition).

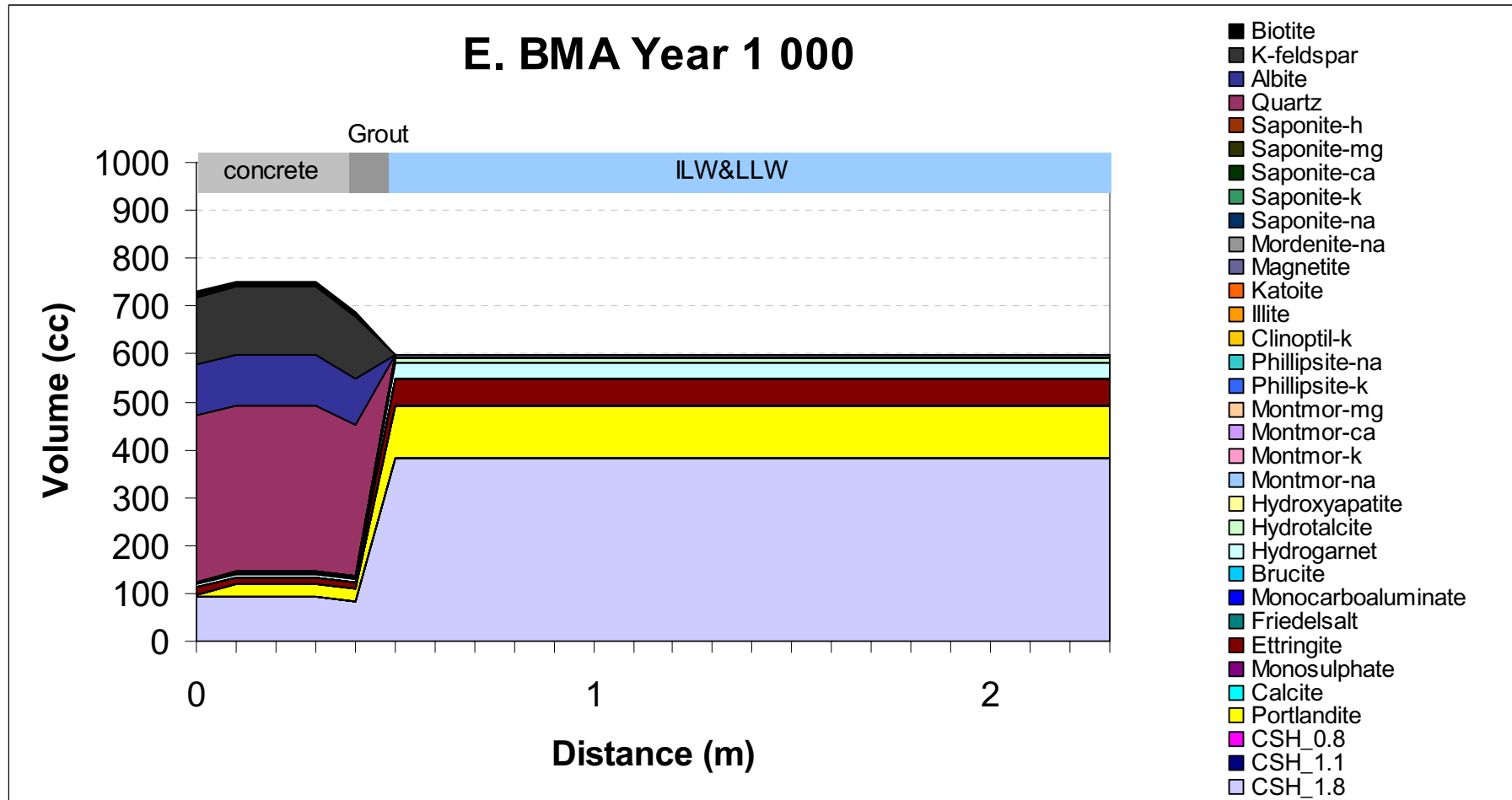


Figure B-55. Mineral distribution in BMA at year 1,000 (dynamic diffusivity, variable temperature and water composition).

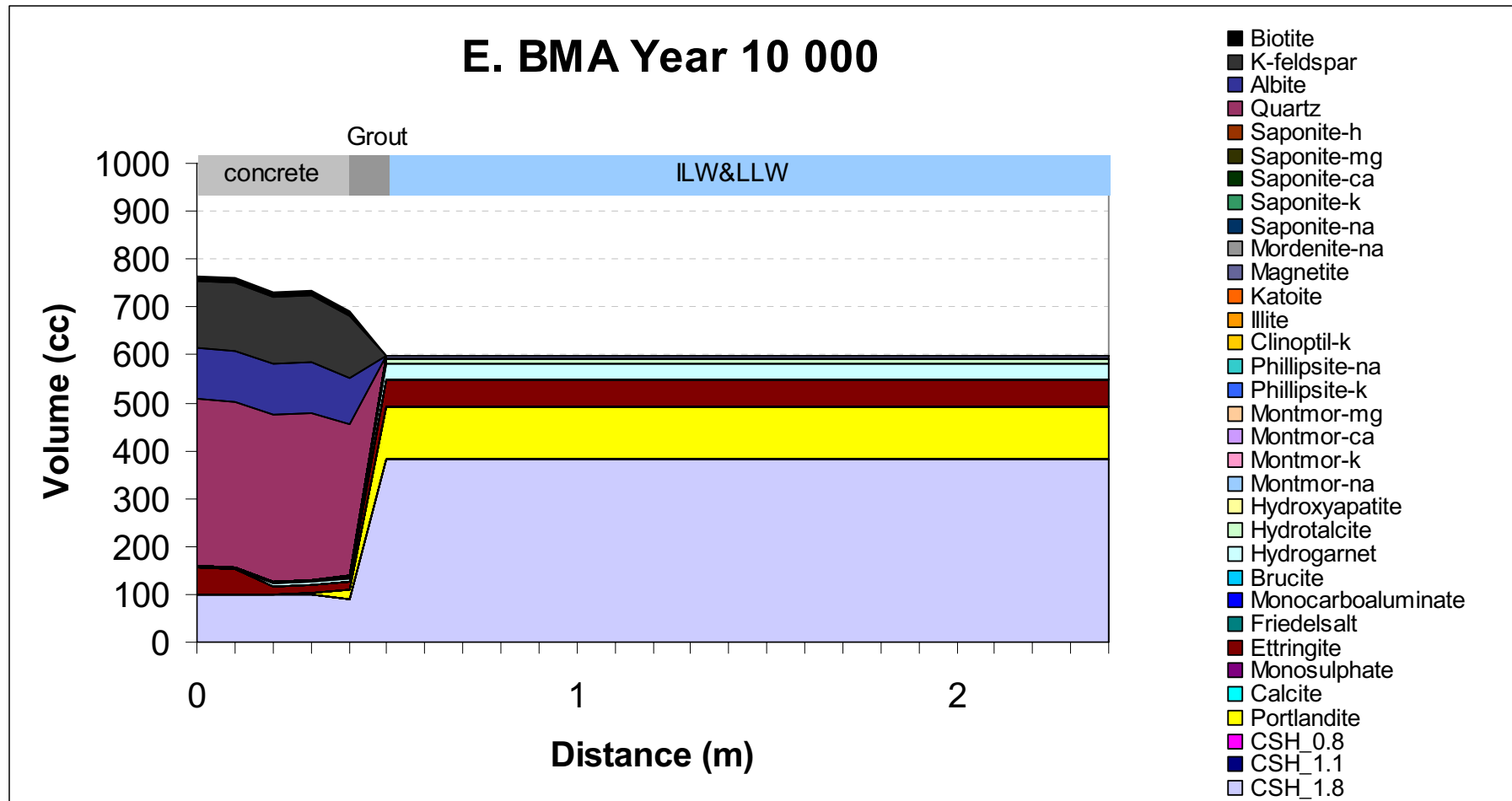


Figure B-56. Mineral distribution in BMA at year 10,000 (dynamic diffusivity, variable temperature and water composition).

E. BMA Year 50 000

100

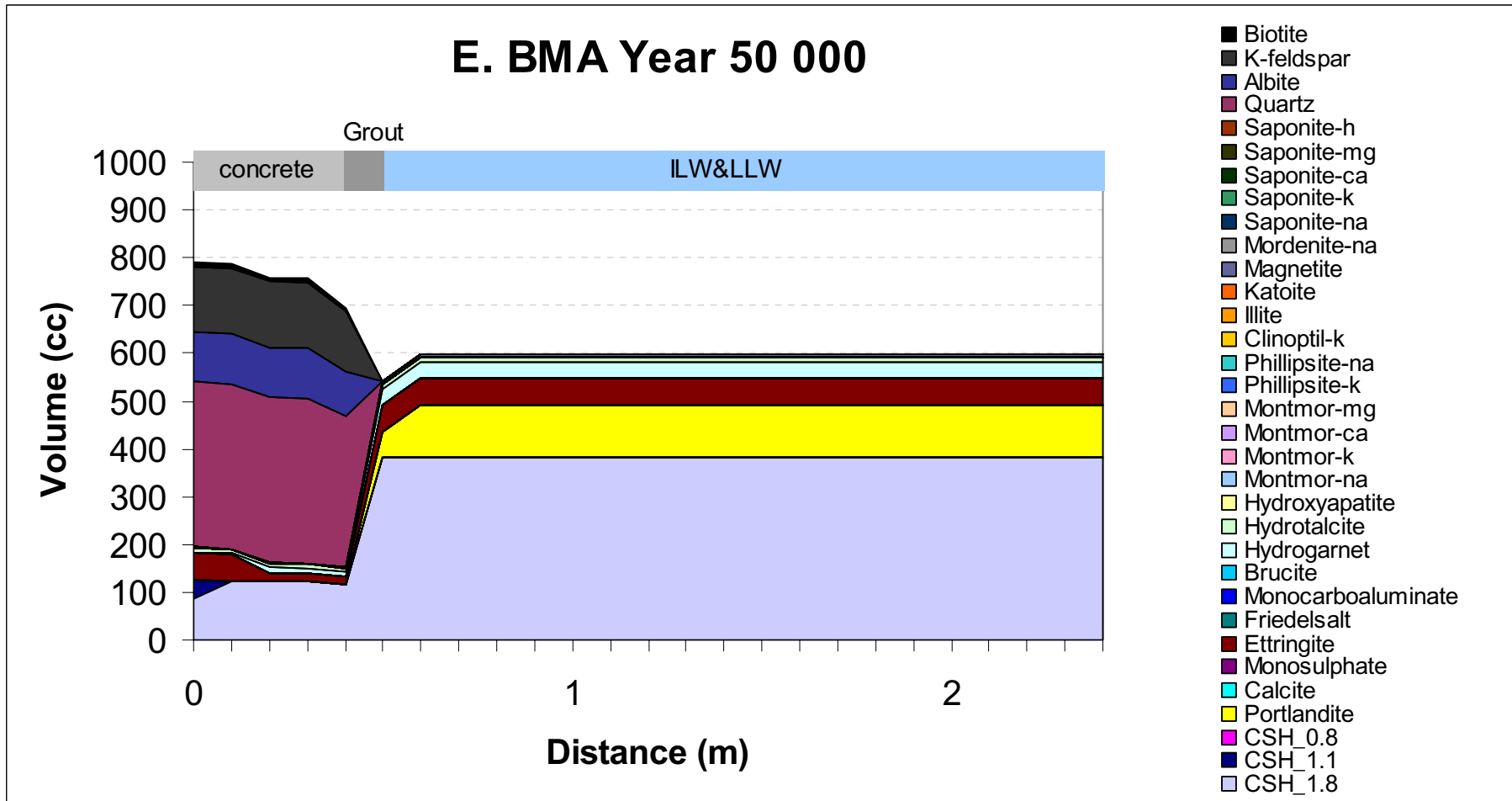


Figure B-57. Mineral distribution in BMA at year 50,000 (dynamic diffusivity, variable temperature and water composition).

E. BMA Year 100 000

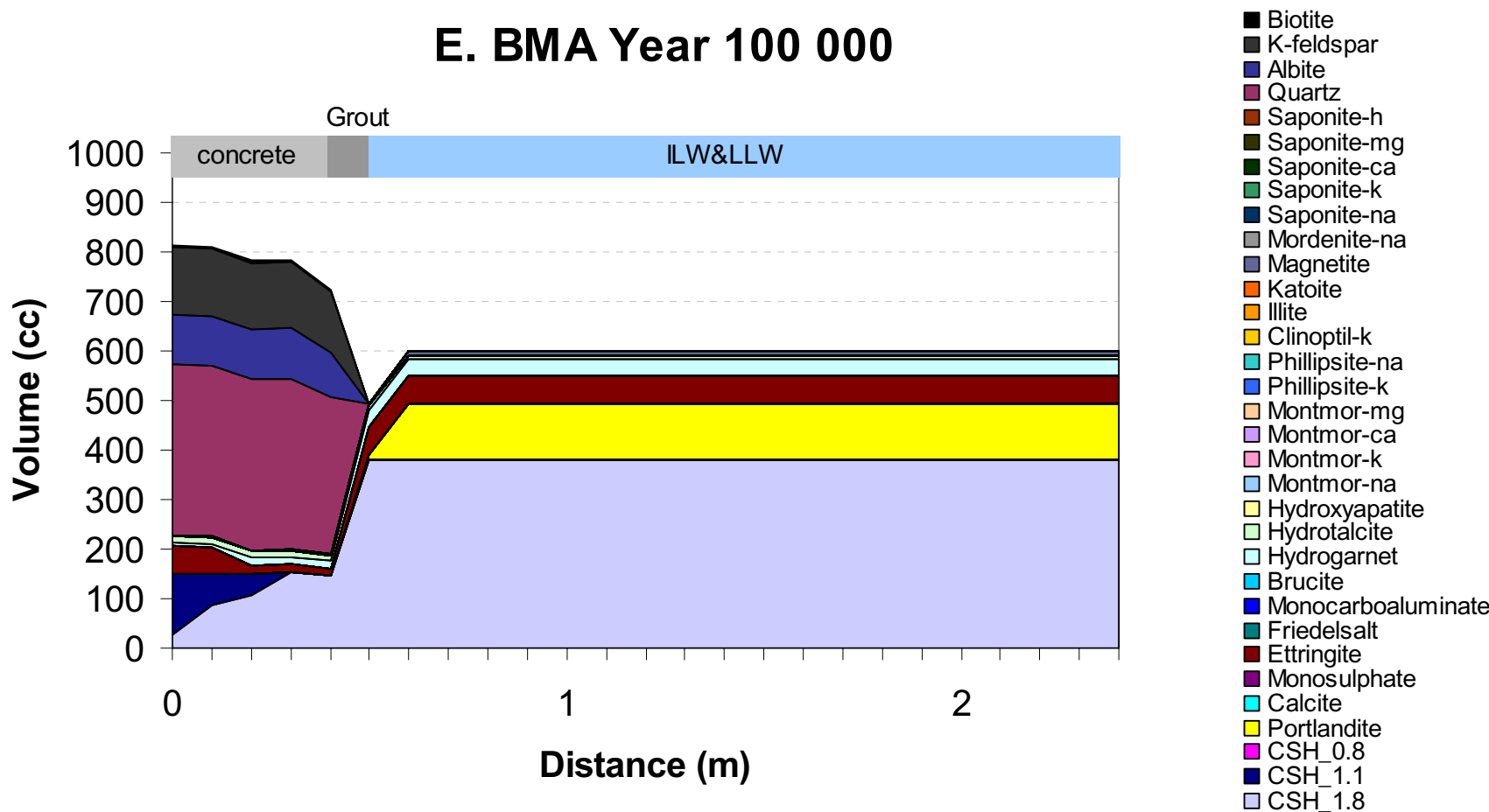
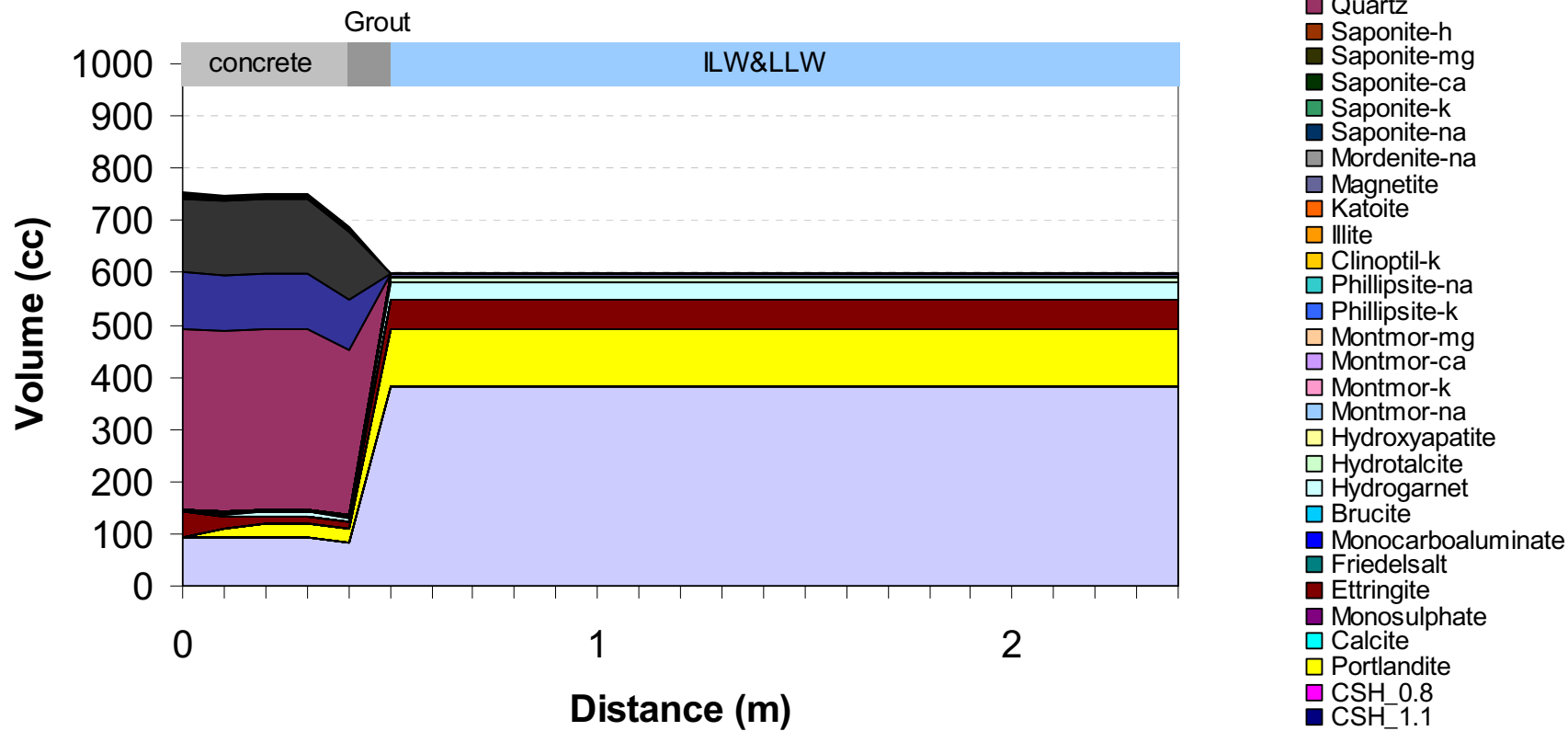


Figure B-58. Mineral distribution in BMA at year 100,000 (dynamic diffusivity, variable temperature and water composition).

F. BMA Year 1 000



- Biotite
- K-feldspar
- Albite
- Quartz
- Saponite-h
- Saponite-mg
- Saponite-ca
- Saponite-k
- Saponite-na
- Mordenite-na
- Magnetite
- Katoite
- Illite
- Clinoptil-k
- Phillipsite-na
- Phillipsite-k
- Montmor-mg
- Montmor-ca
- Montmor-k
- Montmor-na
- Hydroxyapatite
- Hydrotalcite
- Hydrogarnet
- Brucite
- Monocarboaluminate
- Friedelsalt
- Ettringite
- Monosulphate
- Calcite
- Portlandite
- CSH_0.8
- CSH_1.1
- CSH_1.8

Figure B-59. Mineral distribution in BMA at year 1,000 (fracture model).

F. BMA Year 10 000

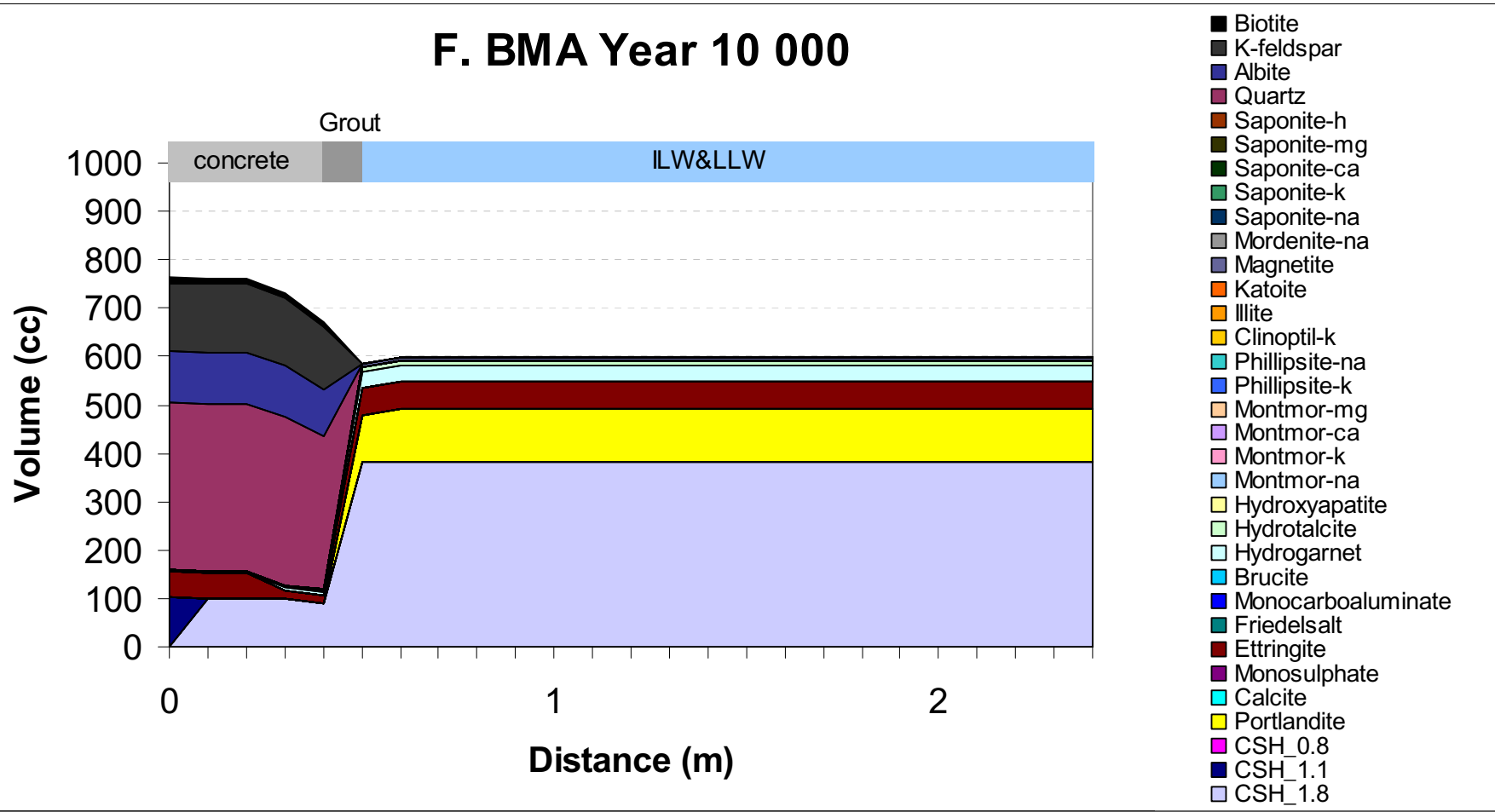


Figure B-60. Mineral distribution in BMA at year 10,000 (fracture model).

F. BMA Year 50 000

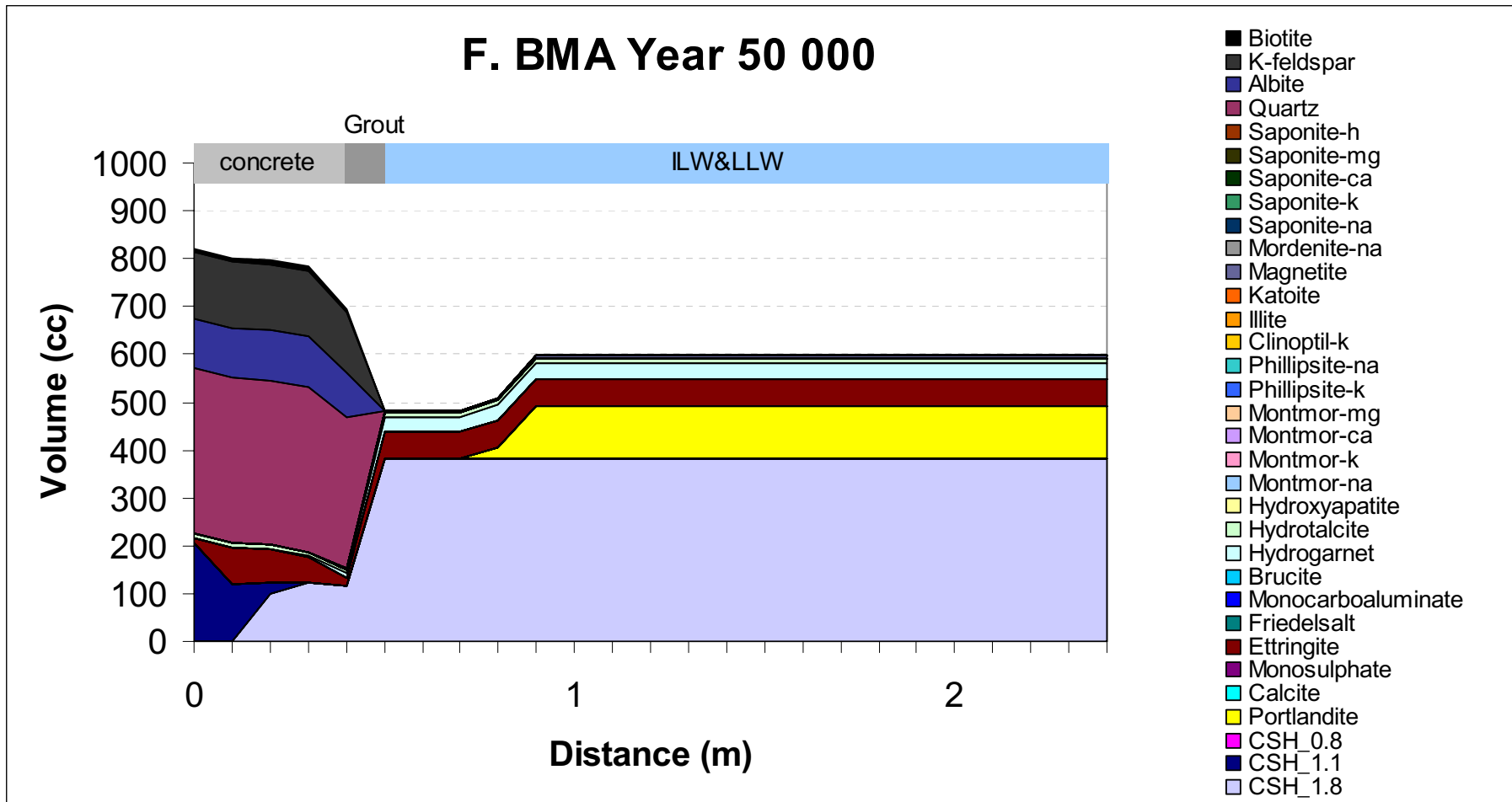


Figure B-61. Mineral distribution in BMA at year 50,000 (fracture model).

F. BMA Year 100 000

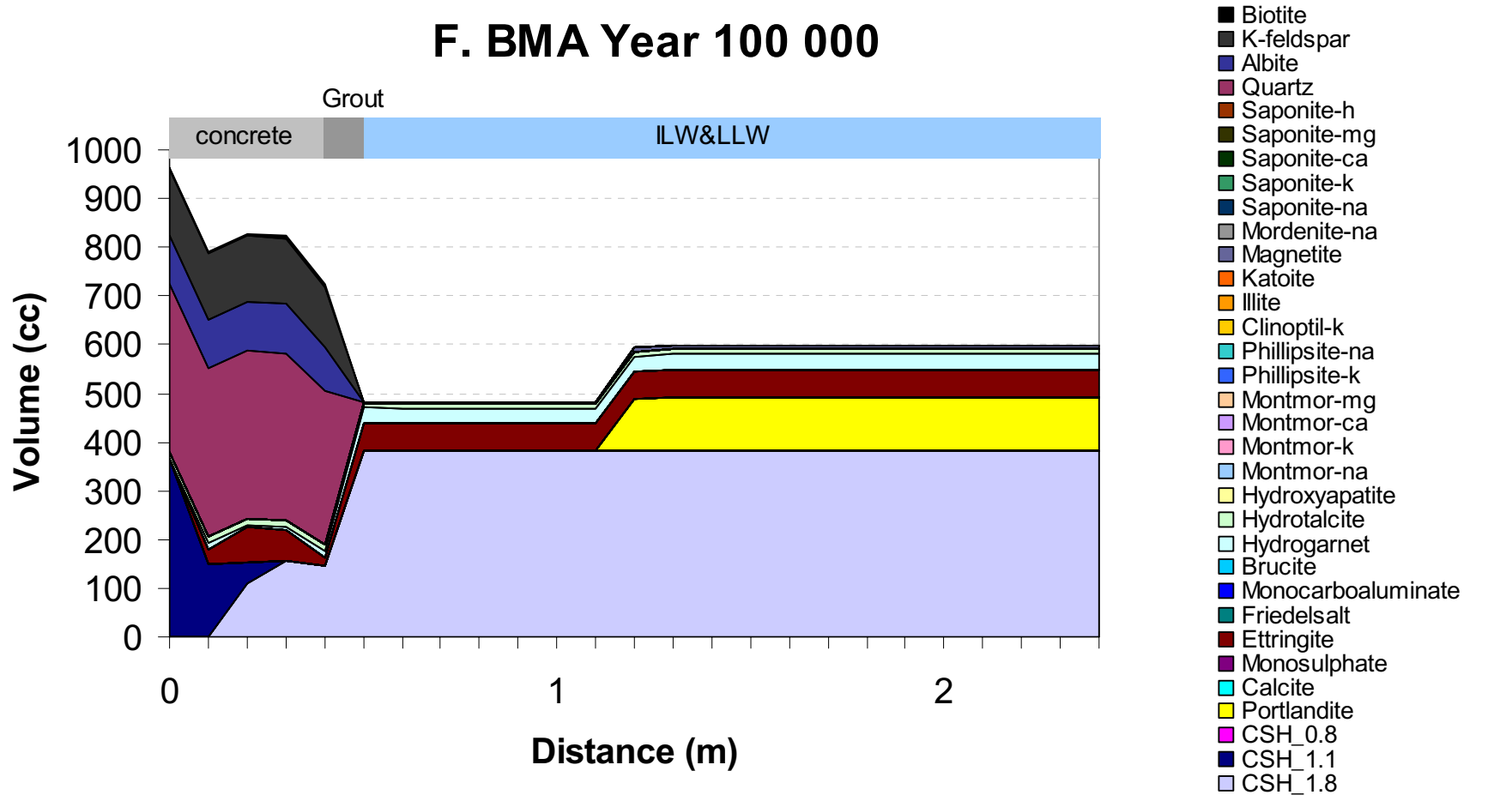


Figure B-62. Mineral distribution in BMA at year 100,000 (fracture model).

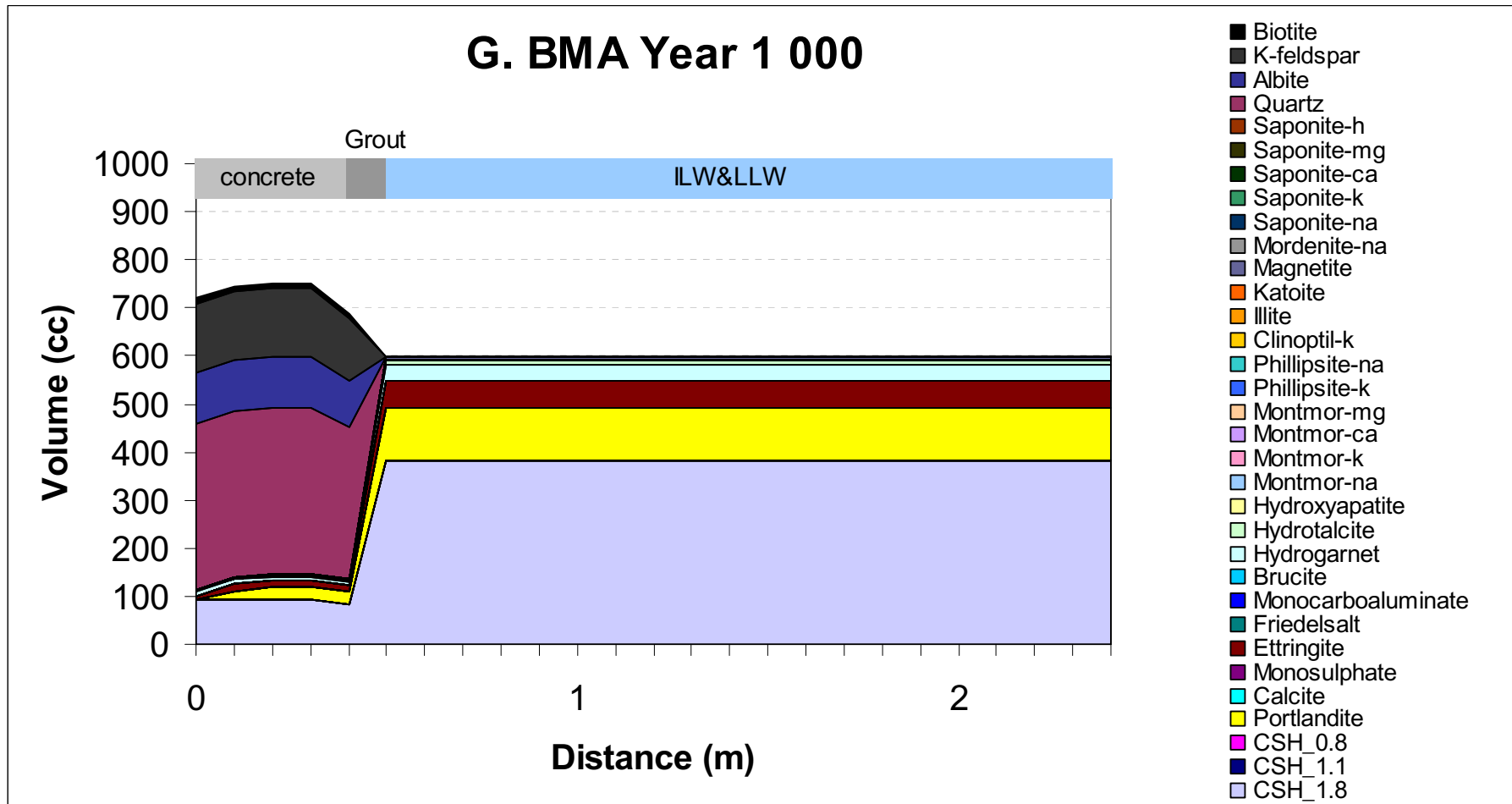


Figure B-63. Mineral distribution in BMA at year 1,000 (freeze-thaw model).

G. BMA Year 10 000

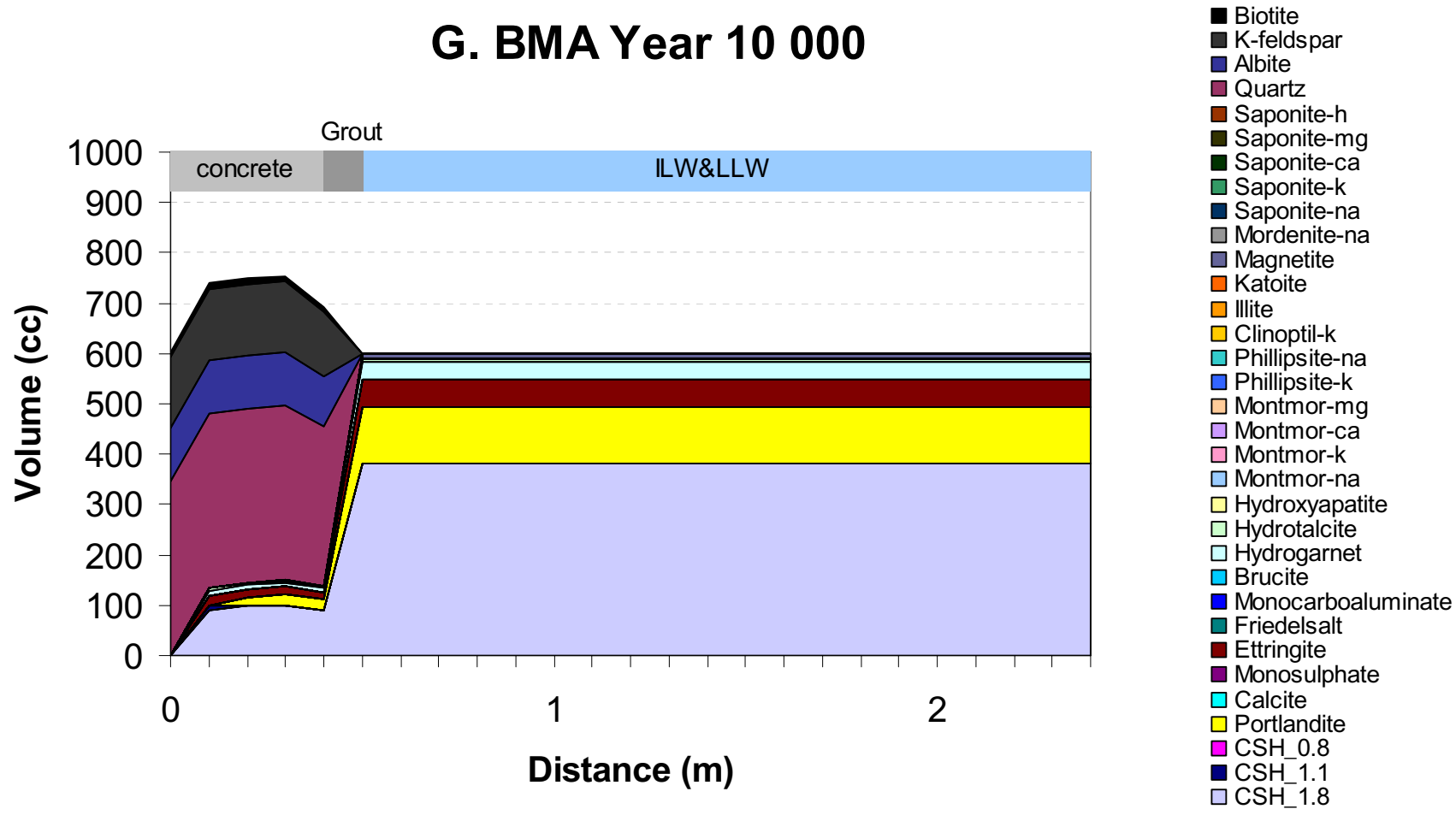


Figure B-64. Mineral distribution in BMA at year 10,000 (freeze-thaw model).

G. BMA Year 50 000

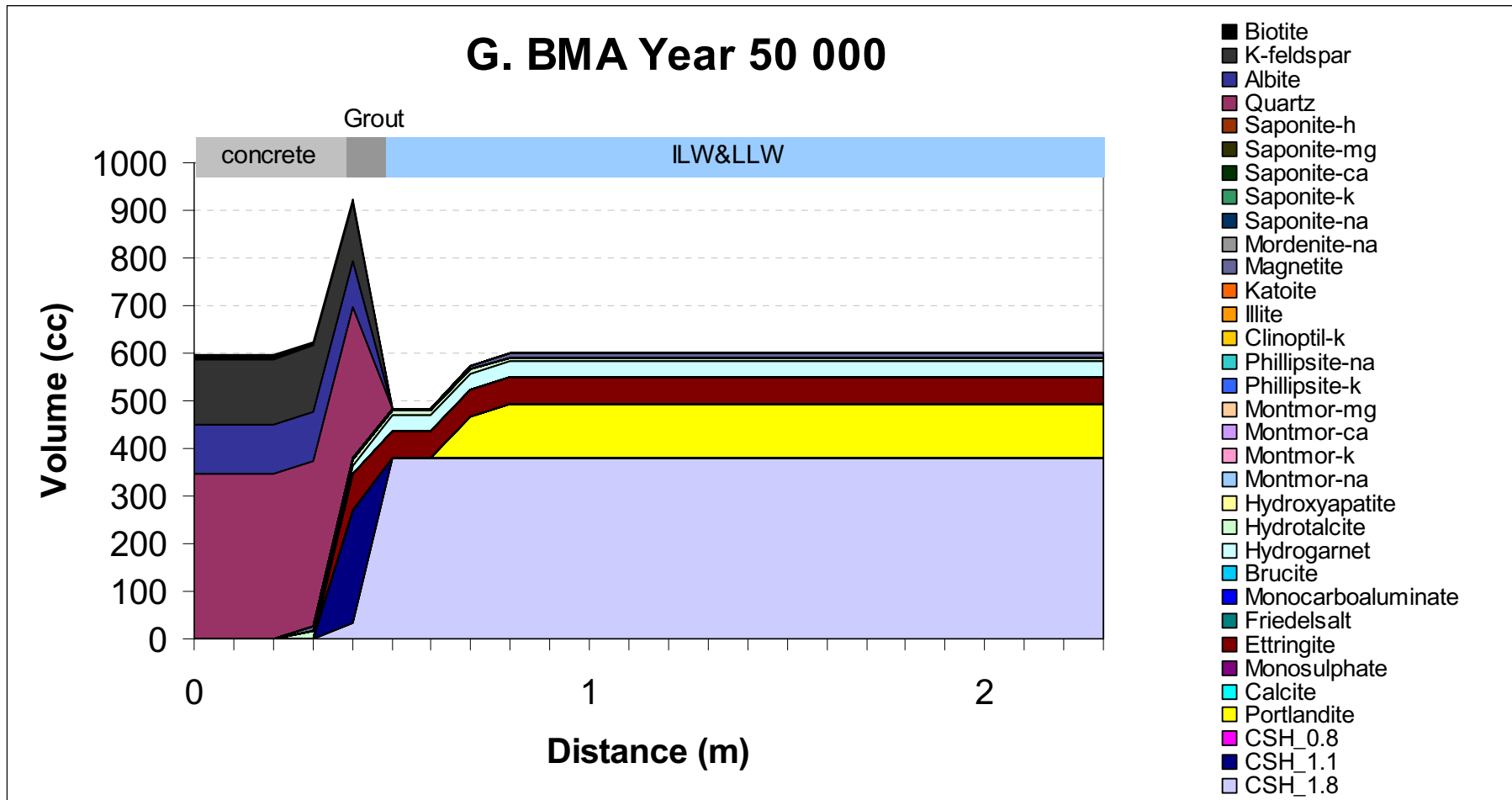


Figure B-65. Mineral distribution in BMA at year 50,000 (freeze-thaw model).

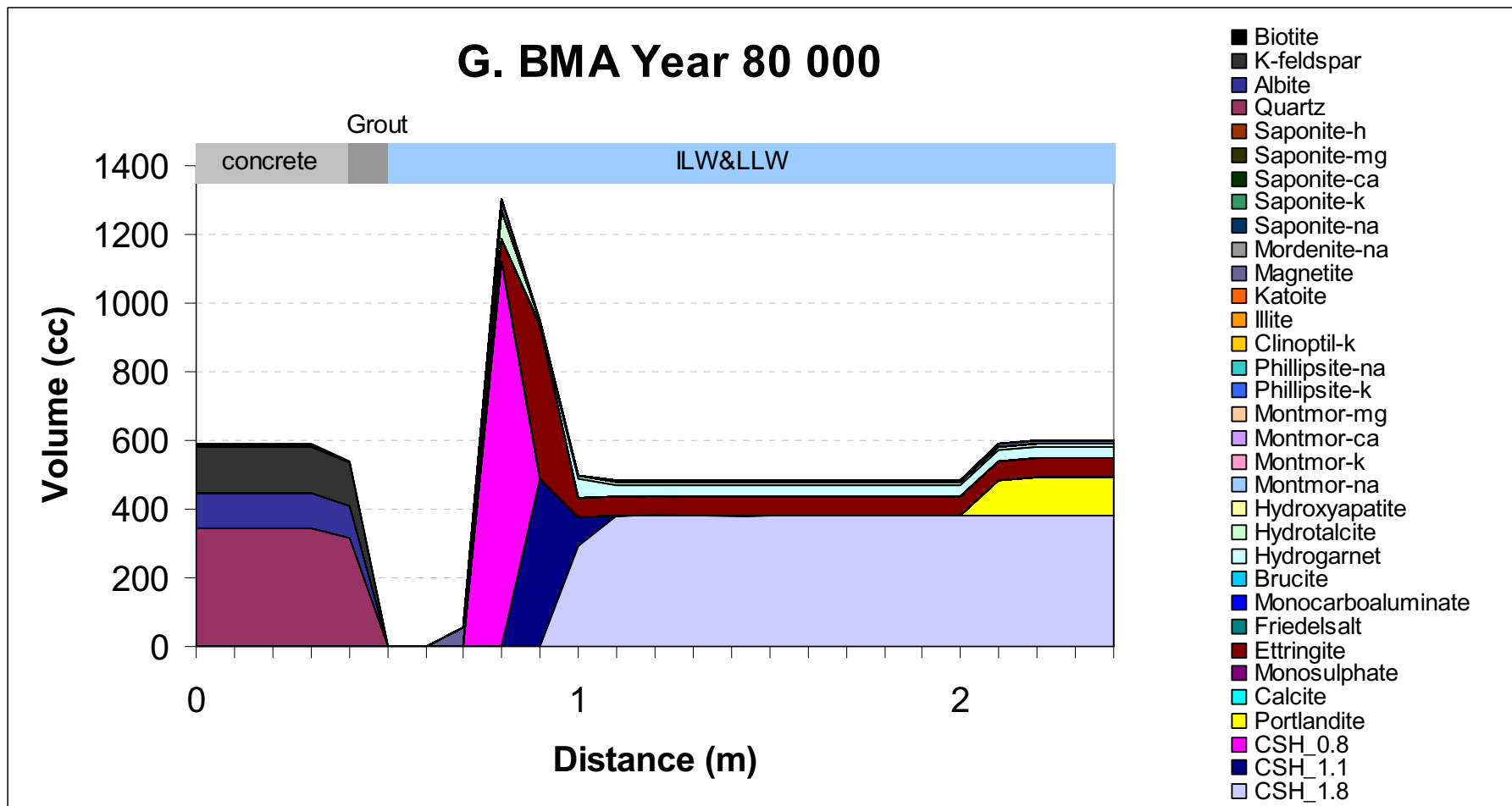


Figure B-66. Mineral distribution in BMA at year 80,000 (freeze-thaw model).

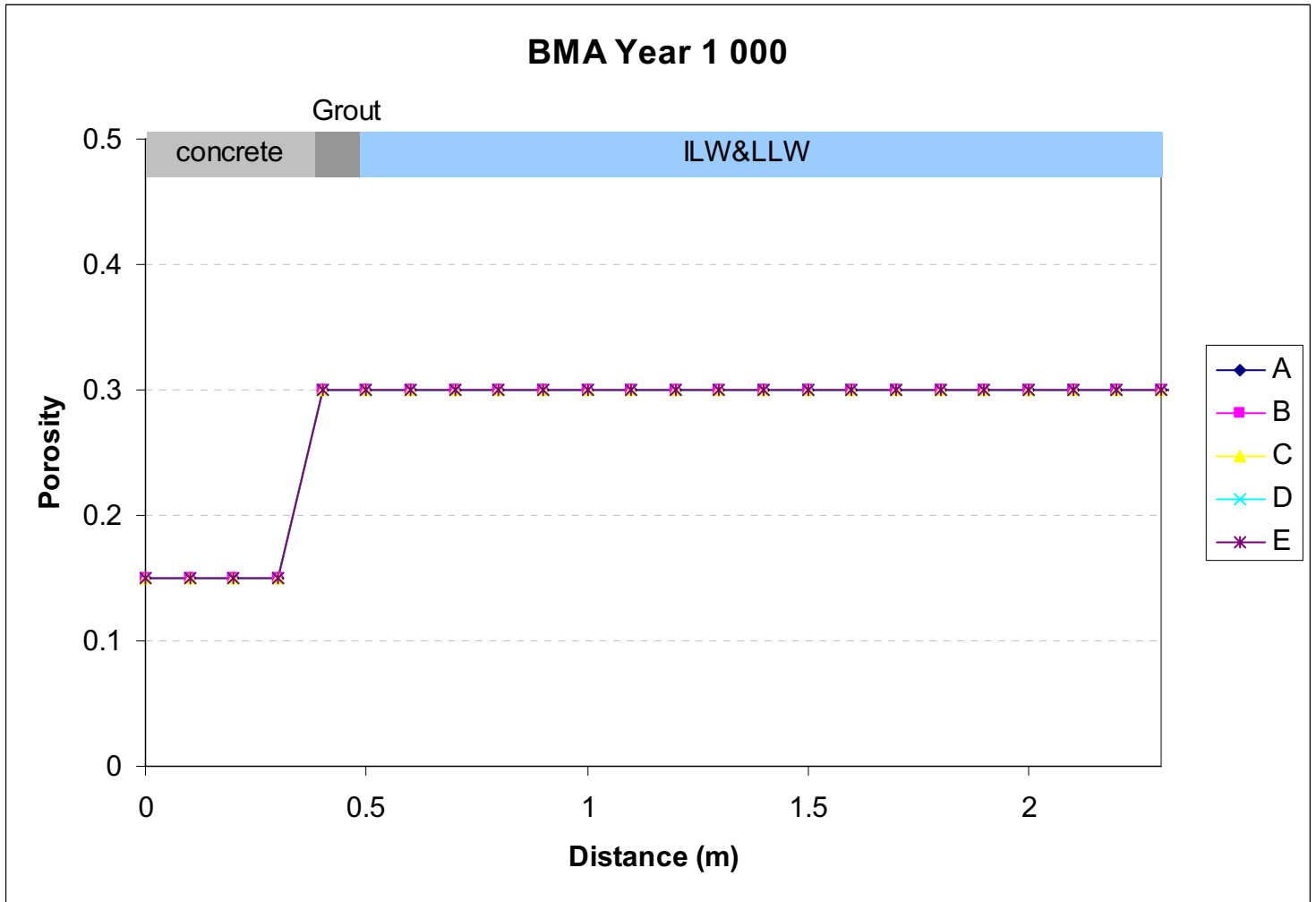


Figure B-67. Porosity distribution in BMA at year 1,000.

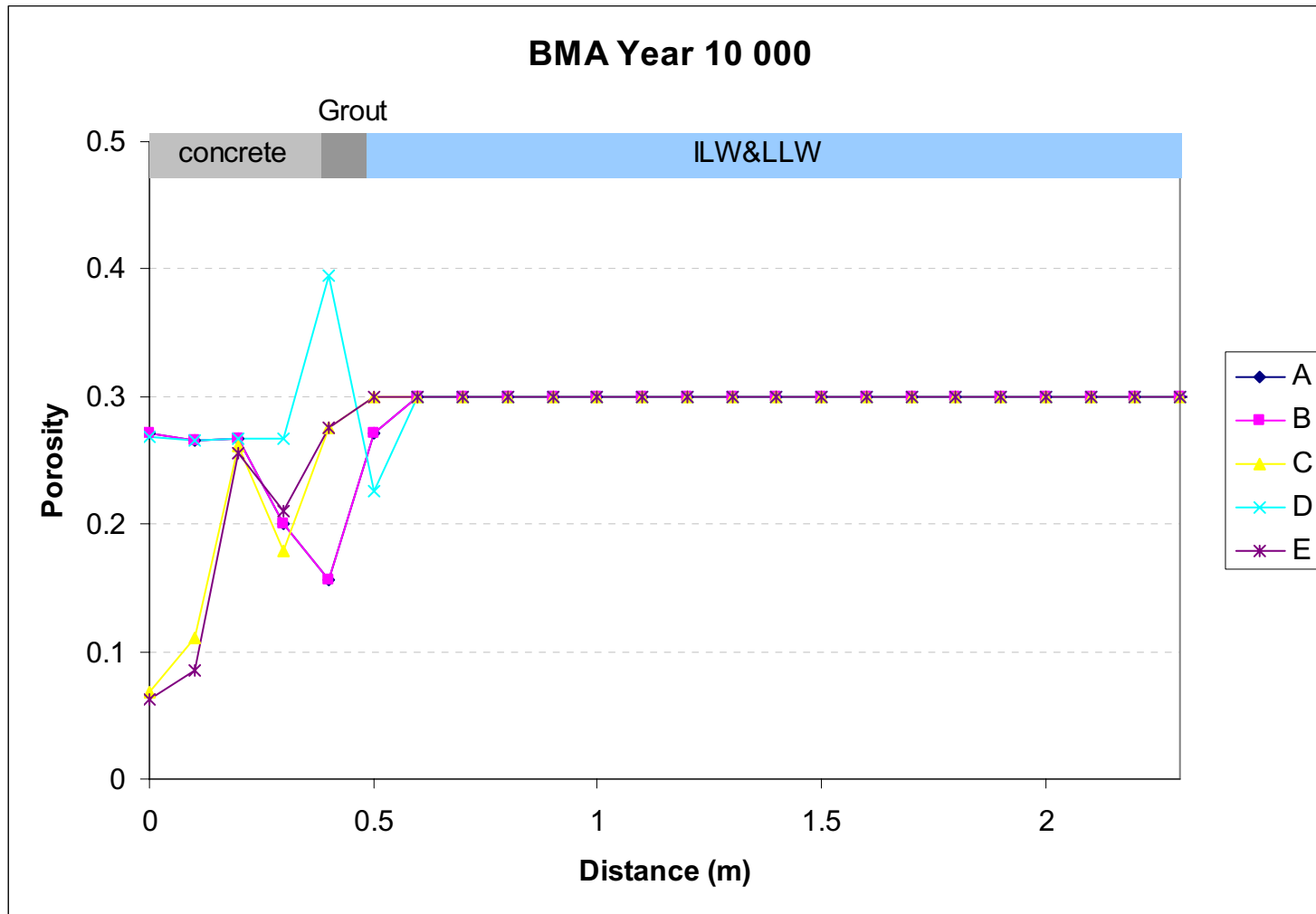


Figure B-68. Porosity distribution in BMA at year 10,000.

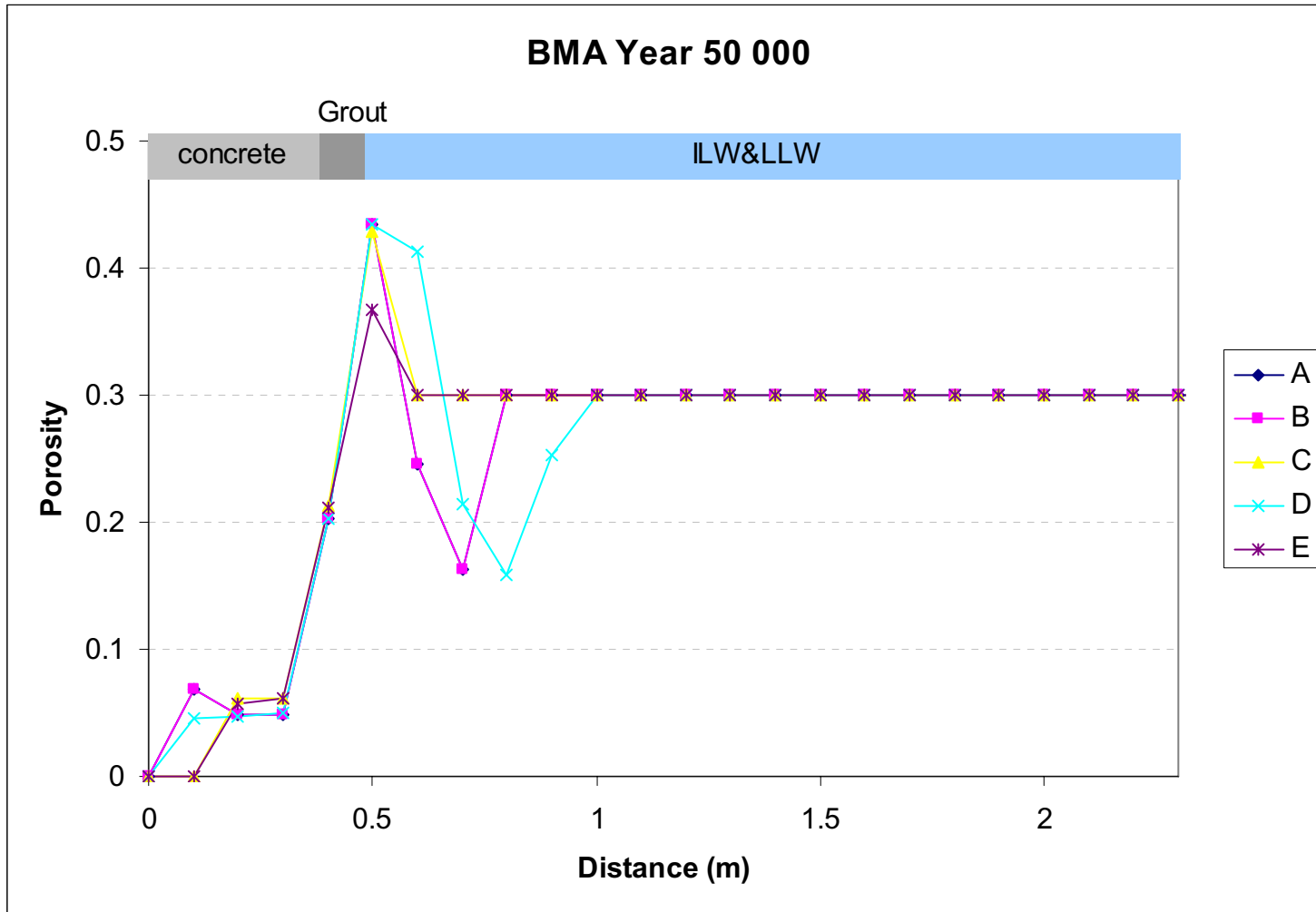


Figure B-69. Porosity distribution in BMA at year 50,000.

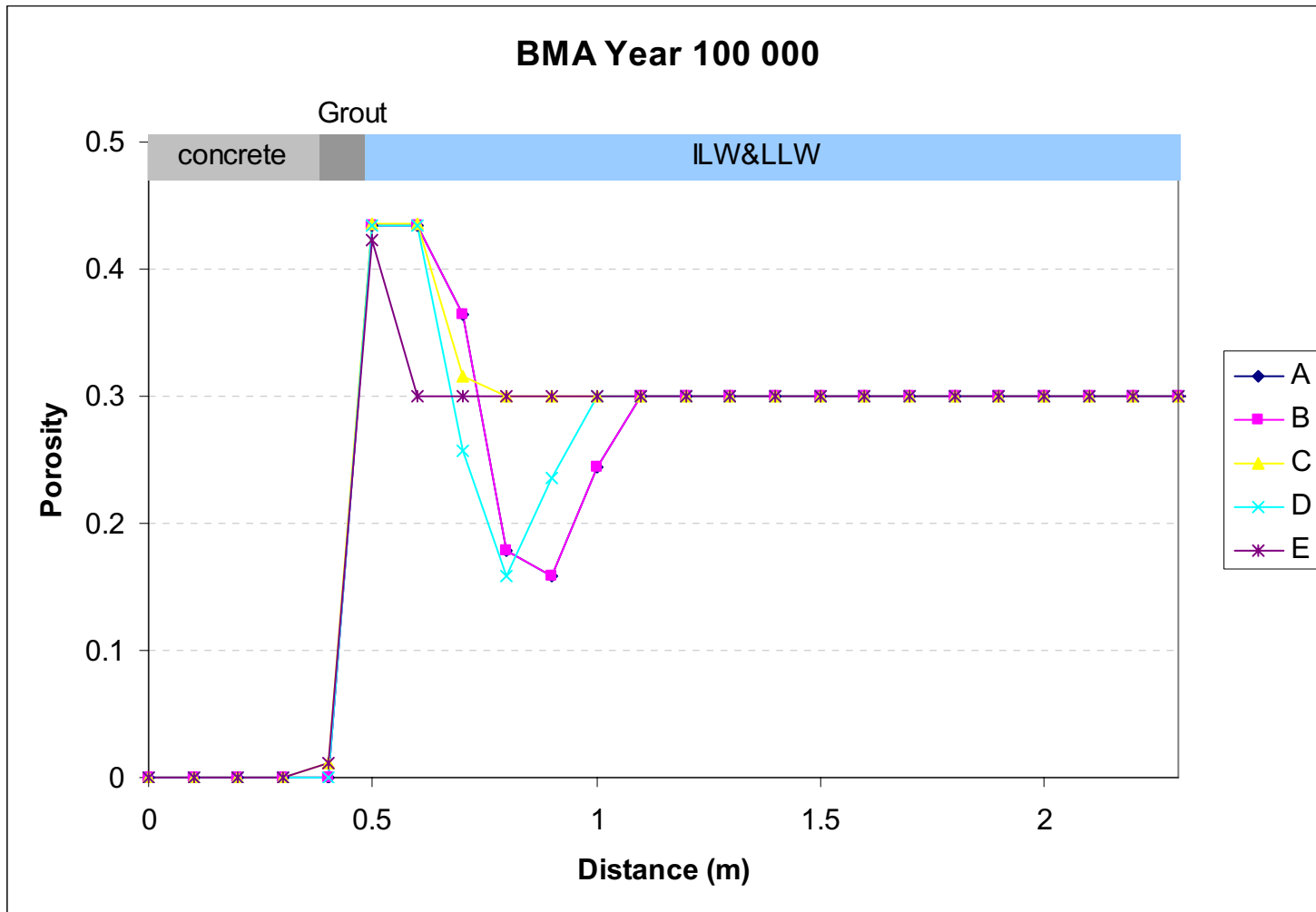


Figure B-70. Porosity distribution in BMA at year 100,000.

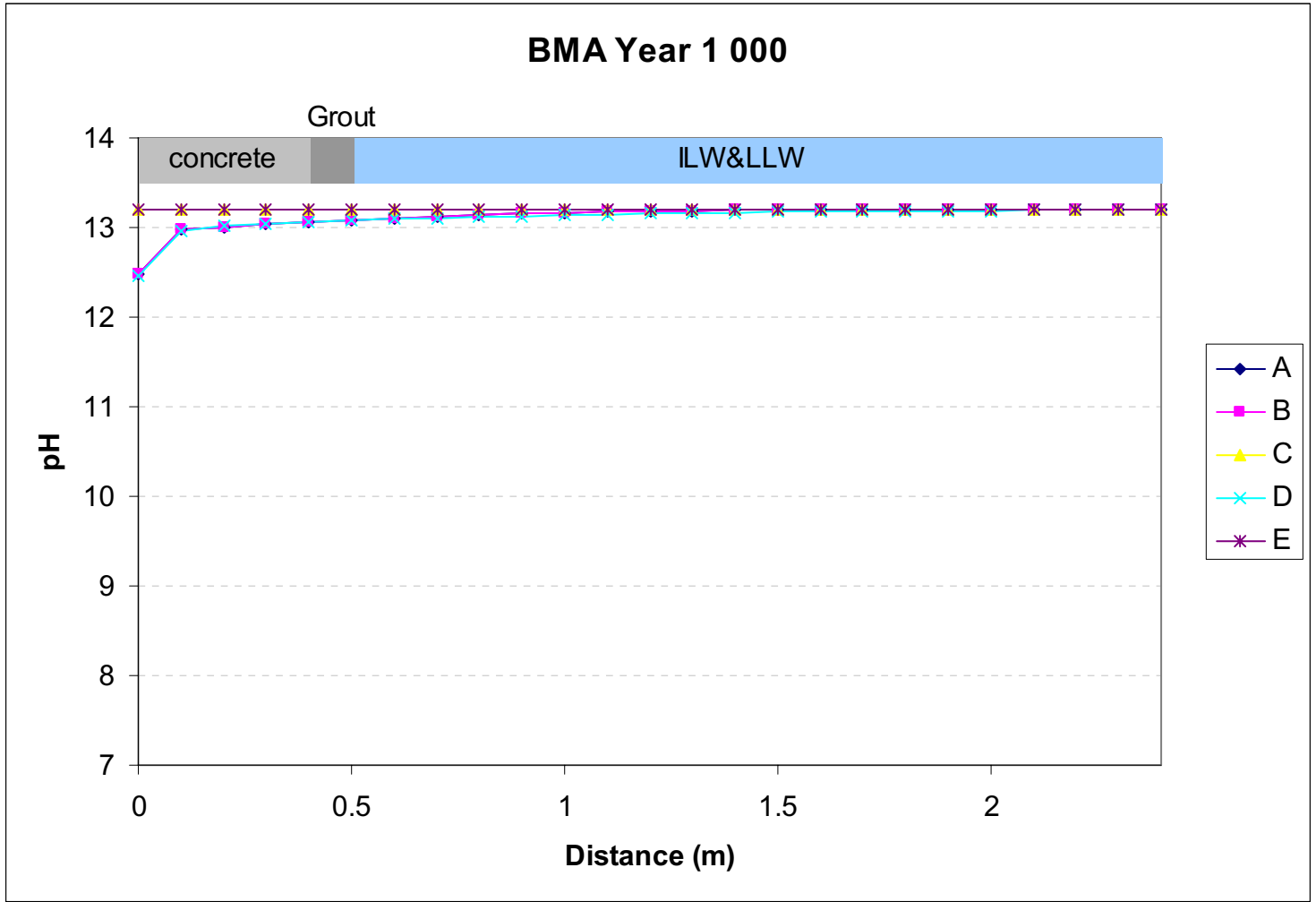


Figure. B-71. pH distribution in BMA at year 1,000.

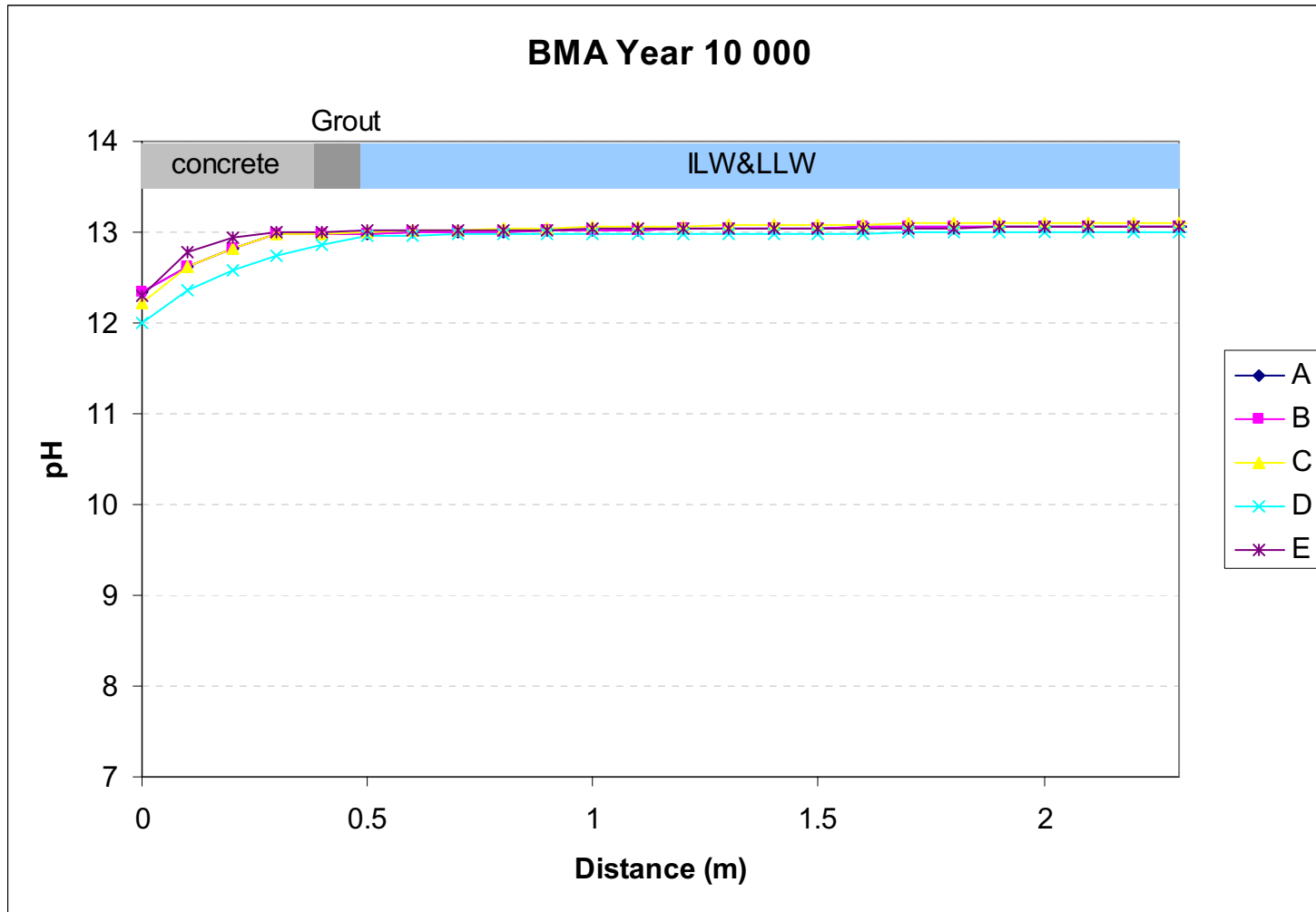


Figure B-72. pH distribution in BMA at year 10,000.

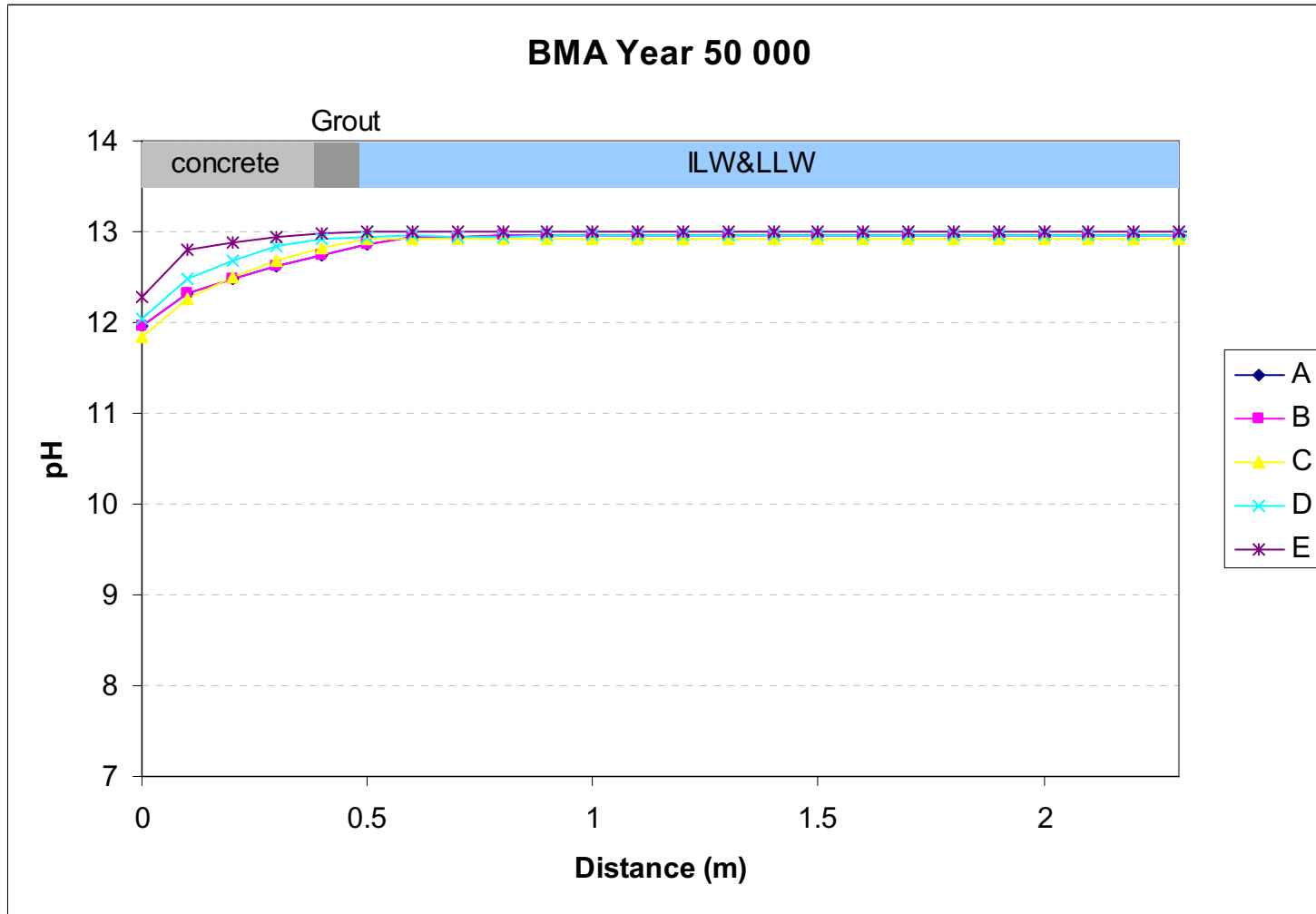


Figure B-73. pH distribution in BMA at year 50,000.

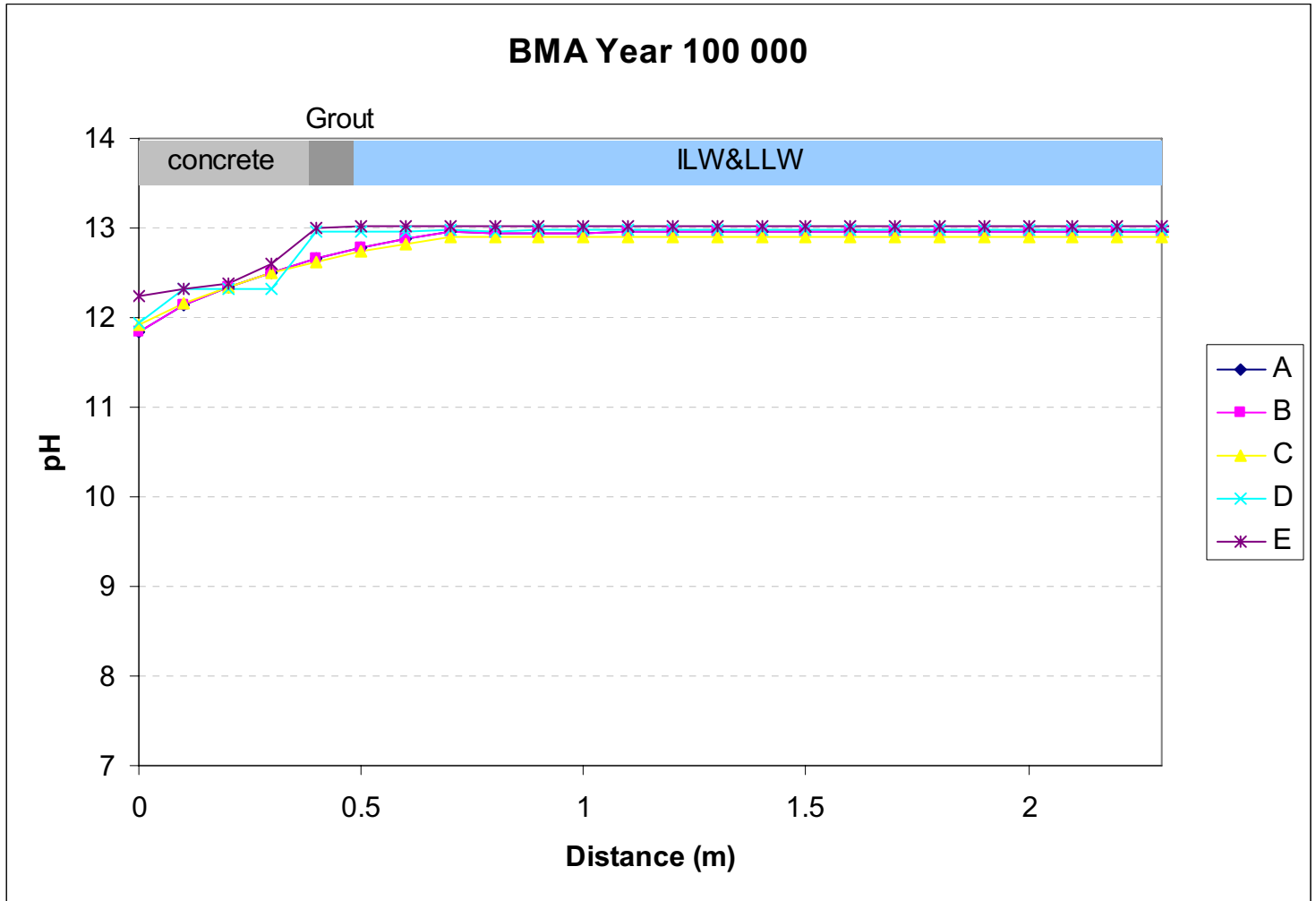


Figure B-74. pH distribution in BMA at year 100,000.